The predictability of internal waves in the continental shelf seas

Anastasiia Domina

School of Environmental Sciences

University of Liverpool

Thesis submitted in accordance with the requirements of the University of Liverpool for the degree of MPhil by Anastasiia Domina.

2021

To my great grandmother and my unborn child

Declaration

I hereby declare that except where specific reference is made to the work of others, the contents of this dissertation are original and have not been submitted in whole or in part for consideration for any other degree or qualification in this, or any other University. This dissertation is the result of my own work and includes nothing which is the outcome of work done in collaboration, except where specifically indicated in the text. This dissertation contains less than 100,000 words including appendices, bibliography, footnotes, tables and equations and has less than 150 figures.

Anastasiia Domina

2021

Acknowledgements

I would like to acknowledge, first and foremost, all my supervisors - Matthew Palmer, Jonathan Sharples, Vasyl Vlasenko and Mattias Green, who supported and guided me throughout this research. As well I would like to thank Nataliya Stashchuk, without whom this MITgcm model would not be possible to present. I would like to thank the members of National Oceanographic Centre (NOC) who has provided an environment in which I was working last couple of years and was able to observe the work of scientists. I would like to thank as well Maria Luneva who always was available for discussions about ocean models. Claire Mahaffey and Lyn Hughes for their help and support during such difficult times of my life combined with a global pandemic of COVID-19. I also would like to thank all my colleagues.

Last, but not least, I would like to thank my parents Tatyana and Valentine, my brother Anton and all my family and friends for always believing in me.

Abstract

Internal waves (IWs) have been recognised as one of the critical controls of climate controlling circulation, biological production and CO_2 pump system in shelf seas. While ocean models can simulate internal tides, they fail to simulate full spectrum of IWs. Therefore the link to mixing and higher frequency IWs is not represented in the vast majority of ocean and climate models. The aim of this work is to increase our understanding of internal wave (IW) dynamics over different topographies and varying stratification in continental shelf seas through a combination of observational (from moorings, gliders) and modelling (MITgcm) methods. We used a new, high-resolution (50m horizontal) MITgcm configuration to generate a realistic internal wave field, which includes high-frequency internal waves and solitons. These model results are compared to varying stratification scenarios from observations made during 2012 and 2015.

Our model suggests that under increasing stratification, the IW field becomes more energetic at all frequencies, however, the increase in energy is not evenly distributed spatially or spectrally. The spectral slope shapes in the MITgcm model are clearly divisible between on-shelf and off-shelf environments - off-shelf, the cascade of internal wave energy is analogous to that of the Garrett-Munk (GM) spectrum. On-shelf, the slope of energy cascade is shown to vary under changing stratification, with a disproportionate increase of energy across higher frequencies resulting in a flatter spectral shape. These results are compared to observations. While realistic variability in tidal forcing and seasonal stratification makes direct comparison of results difficult, there is evidence of a similar reaction to the spectral cascade of IW energy. We investigate this changing spectral shape in continental shelf seas

further using a unique 17-month time series of current velocity and vertical density structure and assess the predictability of internal wave energy under seasonally varying forcing.

Table of contents

List of figures

List of tables

Nomenclature

Roman Symbols

$\bar{S_{ij}}$	mean rate of strain tensor	s^{-1}
$\Delta\rho$	density difference between surface mixed layer and bottom mixed layer	$kg\,m^{-3}$
Δz	pycnocline thickness	m
η	Kolmogorov length scale	m
Γ	mixing efficiency	
λ_{max}	max wavelength	m
ν	kinematic viscosity	$m^2 s^{-1}$
ν_0	amplitude	m
Ω	angular frequency of rotation of the Earth	rad s^{-1}
ω	frequency	s^{-1}
π	Archimedes's constant	3.141 59
ρ	seawater density	$kg\,m^{-3}$
$\rho(z')$	perturbed density	$kg\,m^{-3}$
$\rho_r(z')$	reference density	$kg\,m^{-3}$

φ	latitude	$^\circ$
ζ	vertical displacement of a fluid particle	m
a_1	wave amplitude corresponding to the depth h_1	m
a_2	wave amplitude corresponding to the depth h_2	m
b	e-folding scale of N^2	1.3km
c	group velocity	$\mathrm{m\,s^{-1}}$
c_0	long wave speed	$\mathrm{m\,s^{-1}}$
c_p	internal wave phase speed	$\mathrm{m\,s^{-1}}$
C_t	crest length	km
D	internal tidal wavelength	km
d	diameter of a tube	m
$E(\alpha,\omega)$	dimensionless GM spectrum	
E_T	Turbulent kinetic energy	$\mathrm{m^2 s^{-2}}$
f	Coriolis frequency	$\mathrm{s^{-1}}$
Fr	Froude number	
g	acceleration by gravity	$9.81\mathrm{m\,s^{-2}}$
H	total depth	m
h	current water depth	m
h_1	water depth corresponding to the wave amplitude a_1	m
h_2	water depth corresponding to the wave amplitude a_2	m

If	inertial frequency	15.93h
j	vertical mode number	
k	wavenumber	m^{-1}
K_1	lunar diurnal tidal constituent	23.94h
K_z	diffusion rate	$\mathrm{m}^2\,\mathrm{s}^{-1}$
L	packet length	km
L_0	Ozmidov length	m
l_1	soliton width	m
M_2	lunar semidiurnal tidal constituent	12.42h
M_4	lunar quarter-diurnal tidal constituent	6.21h
M_6	lunar sixthdiurnal tidal constituent	4.14h
M_8	lunar eigthdiurnal tidal constituent	3.11h
N_2	lunar elliptic semidiurnal tidal constituent	12.66h
N^2	buoyancy frequency	s^{-2}
N_b^2	bulk stratification	s^{-2}
O_1	lunar diurnal tidal constituent	25.82h
Q	diapycnal mass flux	$\mathrm{kg\,m}^{-2}\,\mathrm{s}^{-1}$
Re	Reynolds number	
Ri	Richardson number	
Ri_b	bulk Richardson number	

Ri_g	gradient Richardson number	
$Ri_{g\%}$	percentage of times when gradient Richardson number was below 1	%
S	mean salinity component	‰
s'	turbulent salinity component	‰
S_2	solar semidiurnal tidal constituent	12h
S^2	shear stress	s^{-2}
S_b^2	bulk shear	s^{-2}
s_{topog}	topographical slope	
s_{wave}	internal wave characteristic slope	
u	velocity component in the east direction	$m\,s^{-1}$
U_0	tidal speed	$m\,s^{-1}$
U_f	mean flow component	$m\,s^{-1}$
u_f	flow	$m\,s^{-1}$
u'_f	turbulent flow component	$m\,s^{-1}$
U_w	speed of water	ms^{-1}
u_{bn}	baroclinic velocity component in the east direction	ms^{-1}
u_{bt}	barotropic velocity component in the east direction	ms^{-1}
u_h	horizontal velocity component	$m\,s^{-1}$
v	velocity component in the north direction	$m\,s^{-1}$
v_{bn}	baroclinic velocity component in the north direction	ms^{-1}

v_{bt}	barotropic velocity component in the north direction	ms^{-1}
w	vertical velocity component	$\mathrm{m\,s}^{-1}$
x	across-slope distance	
y	slope angle	
ACP	Acoustic Current Profile	
APE	Available Potential Energy	$\mathrm{J\,m}^{-2}$
CCS	Central Celtic Sea	
CMO	Coastal Mixing and Optics experiment	
FASTNEt	Fluxes Across Sloping Topography of the North East Atlantic	
GM	Garrett-Munk spectrum	
HFIWs	High Frequency Internal Waves	
HKE	Horizontal Kinetic Energy	$\mathrm{J\,m}^{-2}$
HrFIWs	Higher Frequency Internal Waves	
ITs	Internal Tides	
IW	Internal Wave	
IWs	Internal Waves	
LFIWs	Low Frequency Internal Waves	
NASA	National Aeronautics and Space Administration	
NIWs	Near-inertial Internal Waves	
NLIW	Nonlinear Internal Waves	

OMG	Ocean Microstructure Glider	
RANS	Reynolds-averaged Navier-Stokes equations	
SSB	Shelf Sea Biogeochemistry	
TE	Total Energy	$\mathrm{J\,m^{-2}}$
TS	Temperature-Salinity chain	

Chapter 1

Introduction

1.1 Abstract

Internal waves are ubiquitous phenomena in the ocean and have an important effect on a variety of temporal and spatial scale processes like climate controlling overturning circulation, CO_2 pump, sustaining fisheries in shelf seas and facilitating deep-water renewals in fjords. Most of the properties of solitary waves in shelf seas are however still poorly understood because it is difficult to measure and parameterise them in ocean models. Therefore, most internal waves, especially high-frequency internal waves (HFIWs), are virtually absent in the most numerical ocean and climate models. The aim of this chapter is to introduce our understanding of the dynamics of shelf seas and internal waves in the shelf seas and in open ocean; to look through the previous research which has been made in this area and to state the main problem to be unraveled by the end of this thesis.

1.2 Motivation

Nowadays, models become more and more advanced, capable to calculate things we were not able to imagine before. But we are still too far from including all physical processes into models, as it would be very challenging even with current technologies. The only solution to that is parametrisation. But how to parametrise chaotic and almost unpredictable components?

Currently, oceanographic models can reproduce tides and internal tides till M4 frequency, but do not represent the full energy spectrum and the tail for turbulence. In our research we are trying to estimate the input of higher frequency internal waves to the turbulence and mixing, which could be the link everybody is trying to find to parametrise turbulence in the models. There are a lot of challenges connected to turbulence parameterisation from the internal tide.

First of all, there is no clear way to separate the generation and propagation components, the most precise percentage which has been proposed recently is 30% local dissipation [St. Laurent and Garrett, 2002] - it means that if certain amount of internal waves have been generated, only 70% will propagate further, but it doesn't take into account the topographical features, the stratification changes in space, the slope criticality. This parameter could not be homogeneous, especially in the on-shelf region, where we can observe a huge variety of slope criticality, topographical features, different forcing conditions, such as stratification and strength of tides.

Another challenge is that we do not have the right dissipation rates in our models, this could lead to the minor or significant errors for the whole internal wave field dynamics of the region and will lead to the incorrect assessment of whole energy cascade.

If both of these challenges will be solved, we could find a way to parameterise the turbulence in certain regions by using the data about internal waves generated in M_2, M_4 frequencies and link it to the turbulence through the higher frequencies.

1.3 Background

The global oceans can be divided into two main areas, separated by the shelf break: the deep ocean with the depth around 4000m and the shelf seas typically with the depth less than 200m. The deep ocean covers most of the planet but, in spite of this, the shelf seas contain 15% of the global ocean production - providing more than 90% of fish, even though the shelf seas form only 7% of the global ocean [Brink and Robinson, 2005]. The shelf seas are important because of their impact on the global ocean processes and because of their economical value. About 40% of human population lives within 100km of the sea [Simpson

and Sharples, 2012] and the shelf seas provide us with leisure activities, energy sources (renewables or offshore drilling), a place for industry and for houses, transportation and could be used in carbon cycling and storage. Due to the immense importance of the shelf seas, a lot of countries with access to the sea are interested in research in this area.

The shelf seas dissipate a lot of energy [Simpson and Sharples, 2012]. There are several large energy inputs in the shelf seas: tidal forces, which propagate from the deep ocean onto the shelf and produce IWs, solar energy, which heats the upper layers of the shelf seas and change density; wind energy, which provides mixing in upper layers and contributes to internal waves [Simpson and Sharples, 2012]. As a result, the shelf seas are the most dynamical regions of the ocean. Only $25-30\%$ of tidal energy dissipates in the deep ocean, the rest is dissipated in the shelf seas [Egbert and Ray, 2000, 2001]. Figure 1.1 shows the distribution of the total tidal dissipation in the global ocean [Egbert and Ray, 2000, NASA]. Based on this figure, there are several areas in the open ocean where the tidal energy dissipation is high mainly due to the ocean ridges and other topographical features, but most of the areas with high tidal energy dissipation are located in the shelf seas. This tidal energy dissipation is important for the carbon and nutrients cycles, and therefore the primary production, and for maintaining the ocean circulation. Diapycnal mixing plays an important role in oceanic heat and carbon storage as shown by the Ocean Mixing Climate Processes Team [MacKinnon et al., 2017].

One of the most energetic and productive regions among shelf seas is the European shelf, where the Celtic Sea, the Irish Sea, the English Channel, the North Sea are located. It is thought that the European shelf is a highly energetic area because there are broad regions of complex topography [Brink and Robinson, 2005].

Before going deeper into the mixing, let us consider the main processes which occur in the shelf seas. There are several energy sources in the shelf seas which could impact on internal mixing. As has been briefly discussed above, one of the sources of mechanical energy in the shelf seas are tides. In many shelf seas tidal currents dominate in the kinetic energy budget, which in turn could have effect on density structure and on transport of suspended matter [Brink and Robinson, 2005].

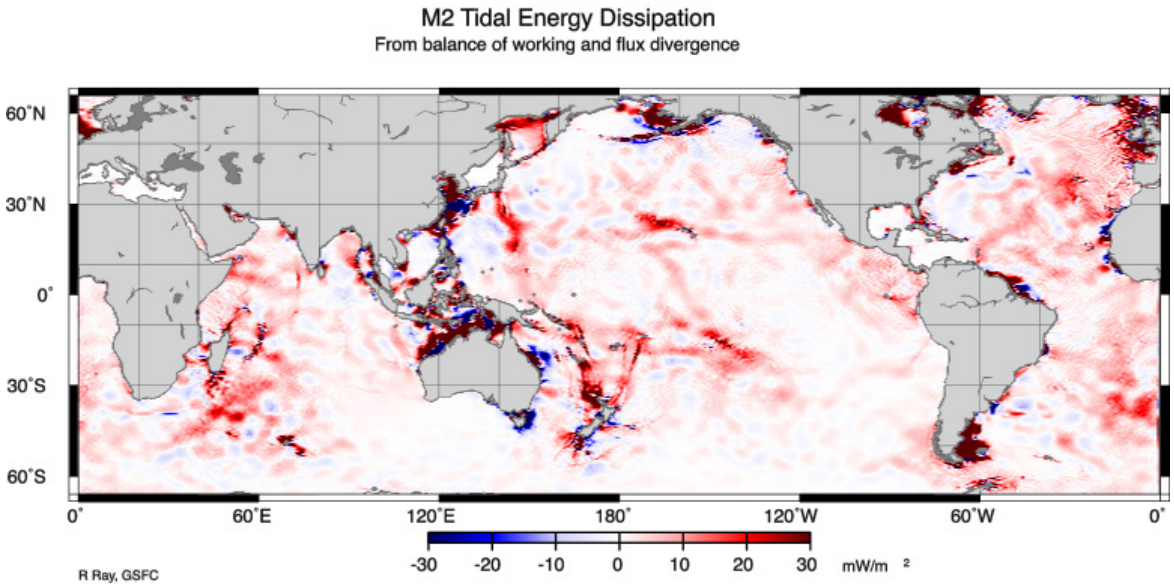

Fig. 1.1 The total tidal dissipation in global ocean [Egbert and Ray, 2000]. Blue areas correspond to the places where the flux divergence is higher and red areas show tides losing energy.

If we look at the difference between the tidal flow in the shelf seas and the deep ocean, we would find that in the deep ocean tidal elevation are small in the majority of cases, tidal currents are weak and there is a small energy dissipation, whereas in the shelf seas the tides are larger significantly and could dissipate a lot of energy [Brink and Robinson, 2005]. As tides move onto the shelf in a form of semidiurnal or diurnal period, they are modified by various processes - for example, the change of the depth from approximately 4km to 200m, from deep ocean to shelf seas, leads to the reduction in phase velocity and wave length, and in order to keep the energy flux, the wave amplitude should increase and the group velocity should decrease [Brink and Robinson, 2005]. For a long wave, the group velocity c is equal to

$$c = \sqrt{gh}, \tag{1.1}$$

where g is the acceleration by gravity and h is current water depth, the change of amplitude from a_1, which is wave amplitude corresponding to the depth h_1, to a_2, which is

wave amplitude corresponding to the depth h_2, when there is a change of depth from h_1 to h_2 without reflection will be equal to

$$(\frac{a_2}{a_1}) = (\frac{h_1}{h_2})^{0.25} \tag{1.2}$$

and in case of reflection the amplitude change will be equal to [Brink and Robinson, 2005]

$$\frac{a_2}{a_1} = \frac{2}{1+\sqrt{\frac{h_2}{h_1}}} \tag{1.3}$$

In the 1st case, when there is change of depth from 4000m to 200m, the change of amplitude would be by a factor of 2.11. In 2nd case, when there is a reflection, the change of amplitude would be by a factor of 1.6. Some tidal energy which is coming from the deep ocean to the shelf sea is not only reflected, but could be dissipated locally or propagated further on shelf. The energy which was generated by tides in the deep ocean propagates onto the shelf as a long wave or as an internal wave which could be dissipated by friction in the shelf seas [Simpson and Sharples, 2012].

Another source of mechanical energy, which was briefly discussed previously, is the wind stress. Both winds and tides gives a huge amount of kinetic energy to the ocean, according to Munk it is 1TW for wind and 3.7 TW for tides [Munk and Wunsch, 1998], whereas Ray and Egbert, as it was pointed earlier, have found that the winds give about 1TW and the tides could supply another 1TW [Egbert and Ray, 2000]. It still under question what is the exact amount of energy coming from tides. But all these amounts of mechanical energy are very small compared to the seasonal exchange of heat between the ocean and the atmosphere, which leads to one more source of energy - solar heating [Simpson and Sharples, 2012]. Heat from the sun warms the top layer of the ocean, it heats up the ocean and returns back to the atmosphere through radiation or evaporation, which could lead to changes in stratification, where the surface water is much warmer and lighter than the cold and therefore heavy water underneath. This is important because it makes difficult to mix the ocean. Stratification provides the interface required for generation of internal waves, which will be considered in

the next section. The fresh water from rivers and from rainfall, also contribute to the changes in stratification [Simpson and Sharples, 2012]. Fresh water is lighter than salty water, so adding large amounts changes the density of coastal water, could affect the circulation and mixing as well. Areas where this process is especially important are known as regions of freshwater influence, or ROFI [Brink and Robinson, 2005, Simpson, 1997].

Liverpool Bay is one ROFI example [Panton et al., 2012]. As a result of these inputs - the wind at the surface, the tidal forces and the solar heat exchange - the shelf seas become one of the most dynamic areas with a lot of energy available to turbulent mixing, which is dissipated through the interesting phenomenon called internal waves (IWs), which will be considered in the next section, as well as the general understanding of generation, propagation and dissipation processes of internal waves, different types of IWs, their frequency range (low frequency internal waves - LFIWs , higher frequency internal waves - HrFIWs , high frequency internal waves - HFIWs , their energetics - Available Potential Energy - APE , Horizontal Kinetic Energy - HKE , Total IW energy - TE .

1.3.1 Internal waves

Waves are familiar to most of us, as we have seen them numerous times on surface of the ocean, seas, lakes, rivers. But not all of us know that there are waves inside the ocean, inside seas and lakes, as well as in the atmosphere, stars and in all stratified systems. Originally IWs were studied in the atmosphere, only later, they were discovered by vikings in the ocean, as they are much more difficult to see and measure than in the atmosphere, and in this research we would like to concentrate on them. As has stated in the previous section, waves inside the ocean often occur at interfaces between water layers of different density, and could be driven by tides, wind, surface waves. In a two layered ocean, denser water which is moved upwards into less dense water experiences a downward force and water which is moved downwards experiences an upward force; these movements of water masses are usually called "internal waves"[Thorpe, 2005].

First time the IWs in the ocean have been spotted long time ago by sailors and vikings, who were sailing close to the sources of fresh water, where fresh water lies on top of salty

one, which creates the density gradient, which could potentially slow or even stop the ship, as sailors thought, it was because of some "mysterious force". This "mysterious force" was first reported in 1893 by the Norwegian oceanographer Fridtjof Nansen. During his Fram expedition, he spotted the dead water phenomenon in which his ship experienced a resistance to a forward motion even in a calm sea [Nansen, 1897]. This happened because the ship was moving on a layer of less dense water from melting sea ice, which was on top of dense and salty water. This density gradient is one of the main "ingredients" to generate internal waves, another is a force, an impulse, which was given by the ship itself. These waves dissipated a lot of energy and almost stopped the ship. Nansen observed the rapid change in temperature profiles, which he and Helland-Hansen have later explained in their report in 1909: "the most feasible explanation, according to our view, is therefore, that the changes of temperature, observed at the same depths, are due to oscillatory movements of the horizontal water-strata, at intermediate depths; and owing to their difference of density, these strata rest one on the top of another for a very long time, with more or less sharply defined boundaries horizontally. The knowledge of the exact nature and causes of these "waves" and their movements would, in our opinion, be of signal importance to oceanography, and as far as we can see, it is one of its greatest problems that most urgently calls for a solution" [Helland-Hansen and Nansen, 1909]. And they were right, for more than a century there are still a lot of unanswered questions connected to internal waves. Nansen and Helland-Hansen pointed out that it is difficult to obtain trustworthy representations if the measurements were taken from a small number of isolated randomly chosen stations, which is still a problem as we do not have enough data to understand all processes in the ocean.

In the 1970s scientists were studying internal waves via echo sounders, but it was difficult to see the spread of internal waves, where are they coming from and how huge could they be. Only after 60-70 years from the first written report about internal waves from Nansen we had an opportunity to see internal waves from satellites. In 1975 internal waves have been photographed in the Andaman Sea and near the Strait of Gibraltar by astronauts on the Apollo-Soyuz Mission (NASA) [El-Baz and Warner, 1979]. These internal waves are non-linear and often called internal solitary waves, which consist of wave packets [ESA].

Table 1.1 The typical characteristics of solitary waves [Apel, 2002]

Characteristic	Symbol	Scale	Units
Packet length	L	1-10	km
Amplitude	$2v_0$	-15	m
Upper layer depth	h_1	20-35	m
Lower layer depth	h_2	30-200	m
Long wave speed	c_0	0.5-1.0	$\mathrm{m\,s^{-1}}$
Max wavelength	λ_{max}	100-1000	m
Crest length	C_t	0-30	km
Internal tidal wavelength	D	15-40	km
Soliton width	l_1	100	m

Figure 1.2 shows the satellite picture from Andaman Sea with wave stripes, which represents the internal solitary waves. Because internal waves interact with currents, which in turn interact with the surface waves and change the roughness of the sea [Hughes, 1978], this is a reason why internal waves could be seen from satellites, airplanes and sometimes even ships as stripes of smooth and rough sea surface. Figure 1.3 shows an approximate scheme how do we see the internal waves from the satellites - here the pycnocline displacement of solitary waves is combined with a sea surface and bright or dark stripes (bright corresponds to rough patches, whereas dark correspond to calm areas) [ESA]. However, it could be difficult to use the satellite data for internal waves research, as they could be seen only with a specific angle of the sun and if there are no clouds in this area [Apel et al., 1975], but scientists are still using satellites to see where internal waves could occur.

The first solitary waves were documented by John Scott Russell in his report [Russel, 1844-1845]. He has observed a single hump generated by a barge which was moving in the Union Canal at Hermiston and later tried to recreate it. In 1895, the whole theory was developed by Korteweg and De Vries for solitons [Miles, 1981], however, it was Boussinesq who firstly introduced it [Boussinesq, 1877]. For a long time after that the solitary waves were though to be an unimportant process, but Zabusky and Kruskal showed a computer experiment with the K-dV equation for the collision of two solitary waves [Zabusky and Kruskal, 1965]. From this experiment it has been concluded that after collision two solitary waves will keep their shape and velocities and behave more like particles, rather than waves

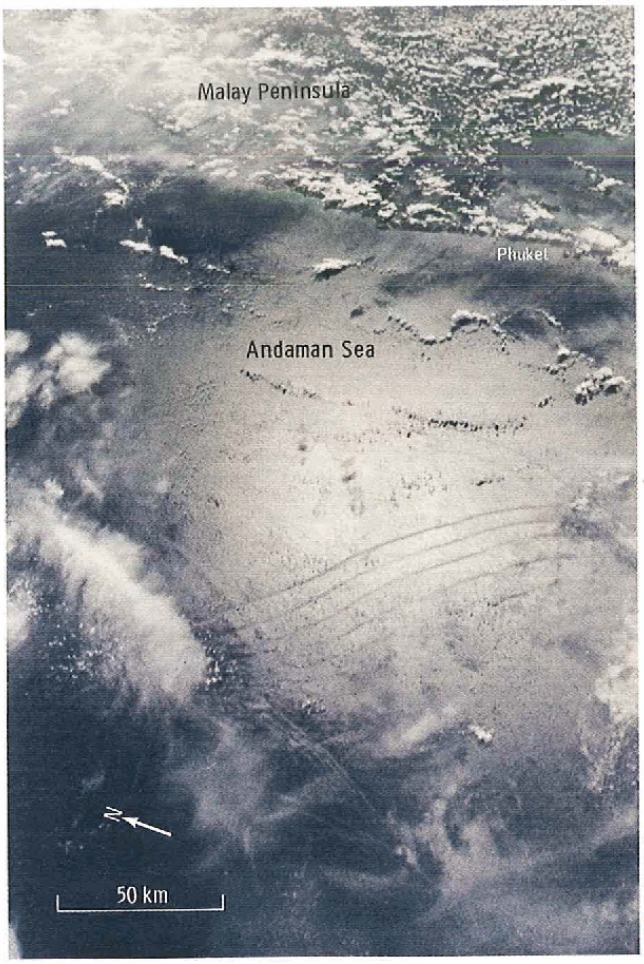

Fig. 1.2 Internal waves in the Andaman Sea, off Thailand, photo is taken during the Apollo-Soyuz mission in 1975 (NASA) [El-Baz and Warner, 1979], this photo was also used in Science journal, 1980.

[Osborne and Burch, 1980]. The typical characteristics of solitary waves are shown in the table 1.1 from Atlas of oceanic internal solitary waves made by Global Ocean Associates [Apel, 2002].

Here is another example of recent satellite imagery for the internal solitary waves - fig. 1.4. This figure shows one of the largest internal solitary waves recorded in the ocean, here in the South China Sea. In his paper [Alford et al., 2015], Alford shows that in the South China Sea they have found internal waves of >200-metre-high that give rise to turbulence more than 10,000 times compared to the open ocean. These waves are the largest waves

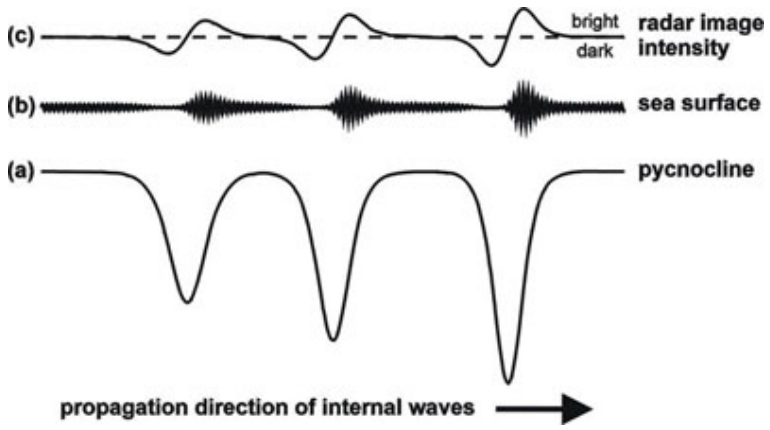

Fig. 1.3 Scheme of solitary internal waves - their shape of the pycnocline (a), sea surface roughness (b), and satellite image intensity (c), [ESA].

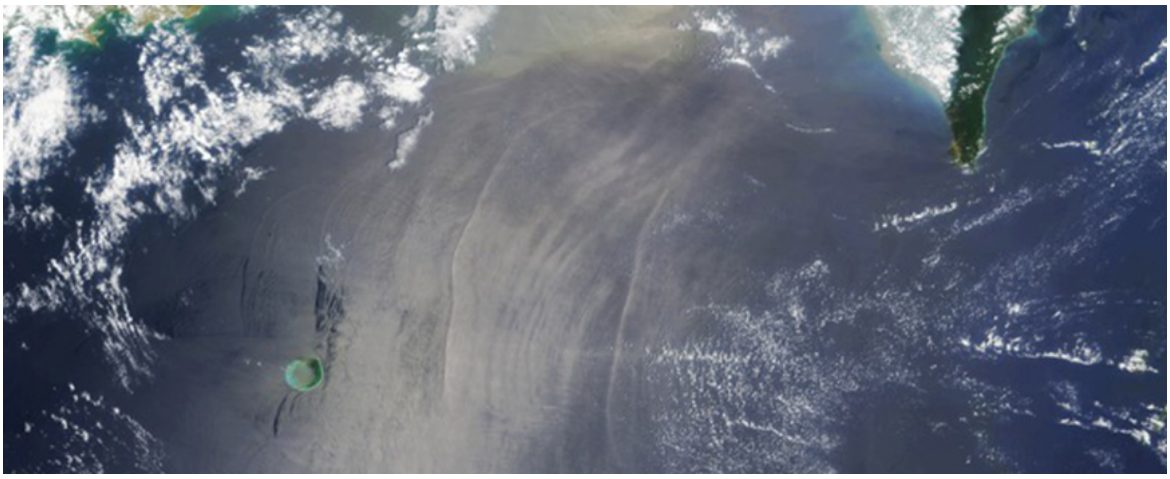

Fig. 1.4 Satellite imagery of South China Sea internal waves [Apel, 2004, NASA].

documented in the global ocean, as their vertical displacement reached up to 500m (which is more than five Big Bens stacked on top of each other), with static instabilities of more than 200m [Alford et al., 2015]. Typical amplitude and period for internal solitary waves are larger than surface gravity waves in oceans because the density gradient inside the fluid is much smaller, and vary from tens of metres to hundreds of metres and from seconds to several hours, respectively [Grue et al., 1999, Klemas, 2012]. The solitary waves found in the South China Sea can exceed 150m displacement just in 5 minutes [Alford et al., 2015], which could be hazardous to some offshore projects. These solitary waves are highly unstable and lead

to turbulence and energy dissipation, which contribute to the local biological productivity [Klymak and Moum, 2003].

Types of internal waves

Depending on source, we can separate internal waves between those, which appear due to atmospheric forces, such as wind (inertial internal waves), and due to tides (internal tides) [Simpson and Sharples, 2012]. The internal waves which were generated by tide over topography, usually called lee waves.

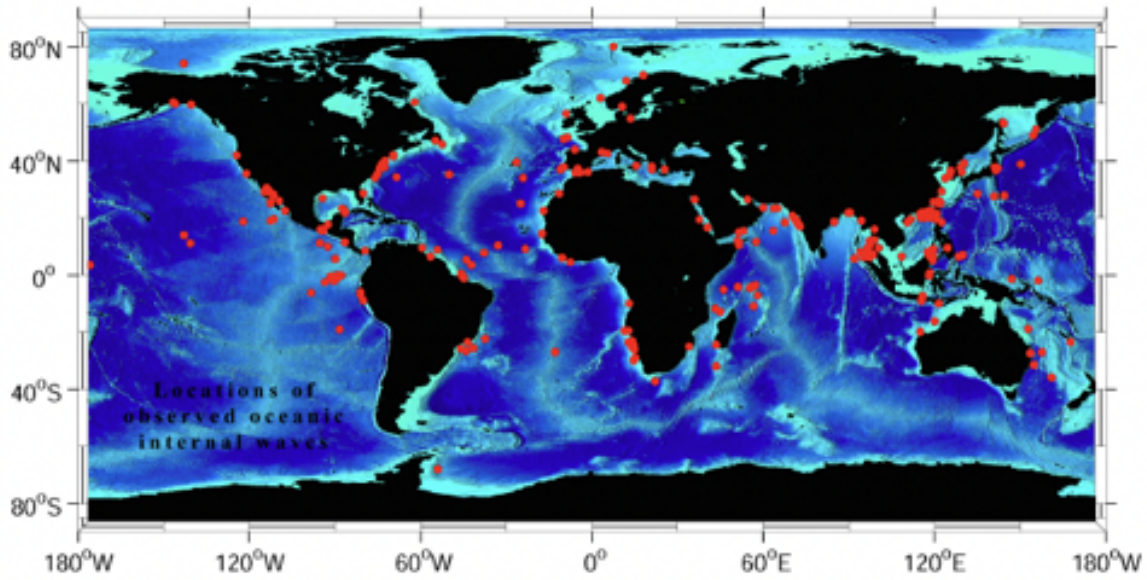

Fig. 1.5 Global atlas of internal waves [Apel, 2004]. The red dots show the locations of internal waves.

There are 75 areas in the world where the internal waves have been observed - Figure 1.5 [Apel, 2004], some of the largest internal tides are formed over the Hawaiian Ridges [Carter et al., 2008, Klymak et al., 2006], over the Stellwagen Bank [Scotti and Pineda, 2004], over continental slopes such as the Malin shelf [Rippeth and Inall, 2002], the Celtic shelf [Hopkins et al., 2014, Palmer et al., 2015, Vlasenko et al., 2014], the Washington continental shelf [Zhang and Alford, 2015], the Luzon Strait [Zhao, 2014]. They are forming in open ocean and shelf seas.

Table 1.2 Internal wave frequency bands for the Celtic Sea area, [Hopkins et al., 2014]

Frequency	Period(h)	Source
If, inertial	15.93	wind
M_2, semidiurnal	12.42	barotropic tide
M_4, quarter-diurnal	6.21	nonlinear interaction $M_4 = M_2 + M_2$
M_6, sixthdiurnal	4.14	bottom friction, nonlinear interaction $M_6 = M_2 + M_4$
M_8, eigthdiurnal	3.11	nonlinear interaction of M_4, $M_8 = M_4 + M_4$

The internal waves usually have different frequencies, for example, there are internal waves which have dominant frequencies, such as one of tidal constituents M_2, S_2, N_2, O_1, K_1, M_4, M_6, M_8, as well internal waves have inertial frequencies If forced by wind, but mainly the internal waves are explored in the low (till M_2) frequencies, which are dominant in the most of the sites (for more information see the table 1.2).

Internal waves have frequencies ranging from the buoyancy frequency $N^2 = -\frac{g}{\rho_0}\frac{d\rho}{dz}$, ; where ρ is the seawater density and g is the acceleration due to gravity, to Coriolis frequency $f = 2\Omega \sin\varphi$; where $\Omega = \frac{2\pi}{T} = 7\,2921 \times 10^{-5}$rad s^{-1} is the angular frequency of rotation of the Earth and φ is the latitude [Gerkema and Zimmerman, 2008].

The internal waves occurring in tidal frequencies are called internal tides (ITs), and those occurring in near-inertial frequency are called near-inertial internal waves (NIWs) which are mostly generated in the mixed layer by wind forcing [Alford, 2003, D'Asaro, 1985].

Figure 1.6 shows the spectral energy density of pycnocline displacement at the point ST5. This plot shows the distribution of energy between different frequencies - LFIW, which include inertial and tidal - If and M_2 frequency bands, HrFIW, which include M_4, M_6, M_8 frequency bands, and HFIW with frequency bands higher than M_8 and lower than N^2. Like in the majority of shelf seas, in the Celtic sea the inertial (If) and tidal (M_2) frequencies are dominant frequencies, however there is a high peak of energy in M_4 frequency for the ST5 point, meaning that after generating IW on the shelf break and before reaching this point, it went through some changes due to the topographical friction and nonlinear interaction, which increased the energy in HrFIW band. When the depth of the ocean changes between the open ocean and the shelf sea, the relatively steep bathymetry of the shelf slope can lead to

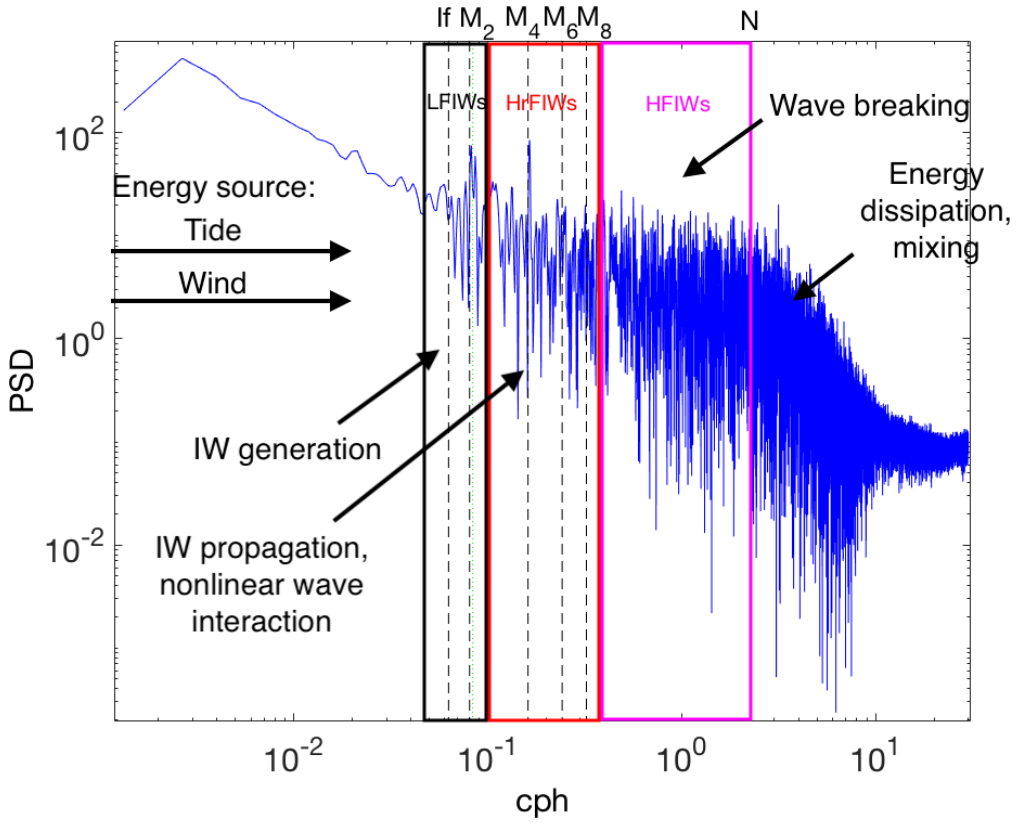

Fig. 1.6 The spectral energy density of pycnocline displacement at the point ST5. The dashed lines shows different frequencies from inertial (If) to buoyancy frequencies (N^2). The black rectangle represents the low frequencies for internal waves, the red rectangle represents the higher frequencies for internal waves and the magenta rectangle represents the high frequencies for internal waves.

the formation of NLIWs of higher and high frequencies [Sharples et al., 2007]. They appear due to the interaction of inertial and tidal frequencies.

High-frequency internal (solitary) waves are important on shelf seas where they contain an enhanced fraction of the baroclinic energy [D'Asaro et al., 2007]. They represent a potential hazard to offshore drilling operations [Hyder et al., 2005] and have important consequences for underwater sound propagation [Zhou et al., 1991]. They represent an important energy transfer mechanism between the large scale tides and vertical mixing, and they often play a key role in biological primary production [Sandstrom and Elliott, 1984] by affecting the exchange of heat, nutrients, and other properties between the shelf and the open ocean [Huthnance, 1995].

Generation, propagation and dissipation of internal waves

There are three different stages of internal waves: generation, propagation and dissipation. The generation of internal waves could be divided into three parts, according to where the excited internal waves form [LeBlond, 1978]:

1. The surface
2. Bottom or lateral boundaries
3. The interior of the ocean.

Due to smaller difference in density between water masses, in comparison with the density difference between the atmosphere and the ocean surface, the restoring force is much smaller than for the surface waves, so less energy is required to form internal waves, resulting in large amplitude of internal waves [Gerkema and Zimmerman, 2008].

The internal waves forced by wind usually have the inertial frequency, whereas the internal waves formed by internal tides have M_2 frequency. Both generate low-frequency internal waves which usually dominates in nature, the interaction of these waves leads to HFIWs. For the internal waves the system of a stratified density structure of the two fluids should have a sharp density gradient in the interface, because if there is a smaller density gradient, there would be smaller wave frequency and slower propagation speed [Apel, 2004].

The Figure 1.7 is showing the mechanism of internal wave generation and propagation. As described by Shaples et al.,2007 [Sharples et al., 2007], during off-shelf ebb barotropic tidal flow the pycnocline is depressed over the shelf edge, which is forming the internal wave. When the ebb tidal flow decreases, this internal tidal wave start to propagate both on- and off-shelf; the short internal waves that cross the shelf edge toward the shallower shelf water can steepen and increase in amplitude, which could lead to vertical mixing [Sharples et al., 2007].

When the internal waves propagate, they carry energy in vertical and horizontal directions, this is due to smaller density gradient between two water masses in comparison with density gradient for the surface waves, [Gerkema and Zimmerman, 2008]. Due to the directions of

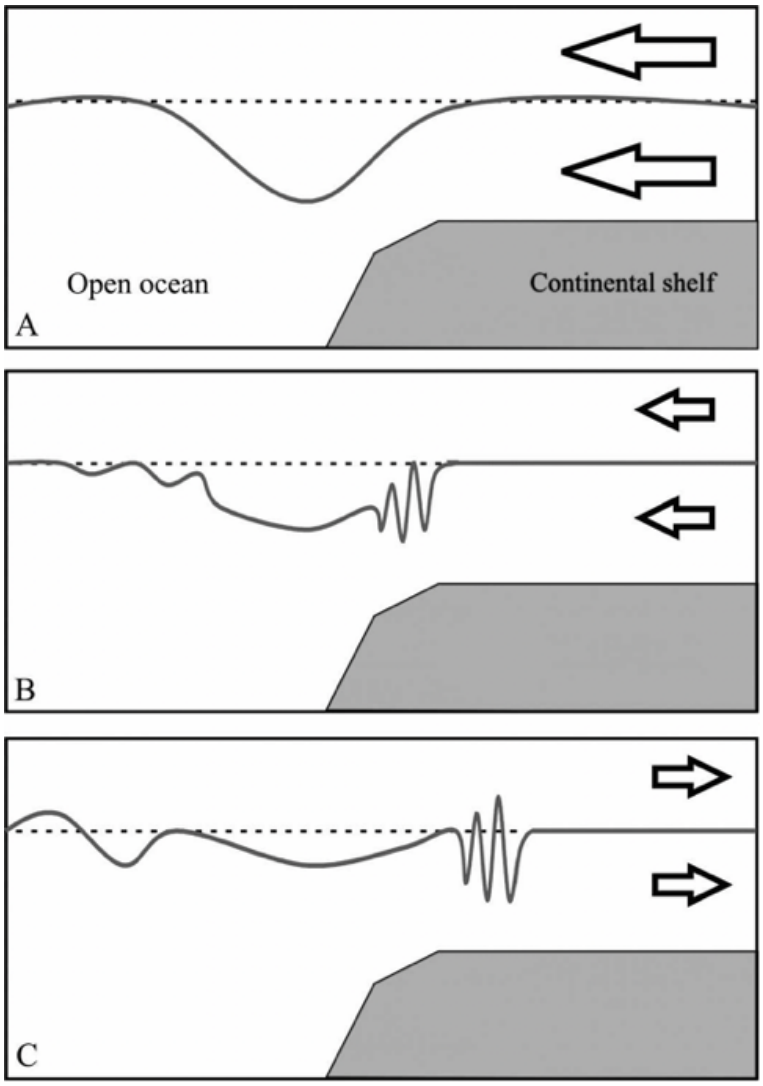

Fig. 1.7 Internal waves generation scheme [Sharples et al., 2007]. (a) During off-shelf tide the pycnocline is depressed giving an impulse to IW. (b) When the tidal flow decreases, this wave is starting to propagate on- and off- shelf, on-shelf the wave is increasing its amplitude due to the shelf break. (c) When the flood tide is coming, these waves propagate further on-shelf steepening on the way, leading to instability and mixing. The arrows show the direction of the tidal current.

propagation, internal waves have horizontal and vertical components of wavenumbers. As the waves propagate they change due to topography, changes in stratification, interaction between waves, and then they dissipate. Dissipation by breaking may result in vertical mixing that is important for a number of coastal processes [Helfrich et al., 2009]. While this energy transfers from bigger to smaller scales, a lot of energy is usually dissipated. For example,

the total dissipated energy from tides - according to Lambeck, [Lambeck, 1989], is 3.4 TW, whereas the dissipation by the M_2 barotropic tide gives 1.7 TW, which is only 50% of the total energy loss [Miller, 1966], which could leave another half to internal tides and higher frequencies. Total dissipation has been calculated more accurately since, but the estimate from Miller has not been increased significantly.

In some cases internal waves break even before they reach the shelf seas. The breaking criterion of the internal waves, according to V.Vlasenko [Vlasenko and Hutter, 2002], is such - when the water depth is less than the depth at the position where the amplitude satisfies the condition

$$a = \frac{0.8^\circ}{\arctan y} + 0.4 \tag{1.4}$$

where the y is the slope angle, the internal wave breaks down before it reach the shallow water, otherwise, it passes through the shallow zone and dissipates later [Vlasenko and Hutter, 2002].

The mechanisms which lead to the breaking of internal waves is not yet fully understood. It is thought that the low frequency low mode internal waves, the one which are generated by tides, transfer their energy to higher frequency internal waves which are steeper and break more easily [Liang et al., 2017].

Internal waves energy

Waves have kinetic energy, due to their orbital motion, and potential energy, because of particle displacement.

Let's define the Total Energy as

$$TE = HKE + APE \tag{1.5}$$

where the horizontal kinetic energy is

$$HKE = \frac{1}{2}\rho \int_{-\infty}^{0} (u_h^2 + w^2) dz \tag{1.6}$$

where u_h is horizontal velocity component and w is vertical velocity component [Simpson and Sharples, 2012].

The available potential energy, which represents the potential energy due to the presence of wave disturbance relative to the fluid at rest

$$APE = \int_{z-\zeta}^{z} g[\rho(z') - \rho_r(z')]dz' \tag{1.7}$$

where ζ is the vertical displacement of a fluid particle, $\rho(z')$ is perturbed density, $\rho_r(z')$ is the reference density [Kang and Fringer, 2010], more information could be found in 2.3.1.

Internal wave energy spectrum in the open ocean

In 1972 Garrett and Munk demonstrated how observations from different locations in the deep ocean could be combined into an empirical model of the wavenumber-frequency energy spectrum, which is called the Garrett-Munk (GM) spectrum [Garrett and Munk, 1972b]. Currently, this spectrum is one of the most useful descriptions of internal wave field in the open ocean. The GM spectrum is usually used to quantify internal wave energy and turbulence levels [Gregg, 1989a, Hibiya et al., 1998, Kunze and Sanford, 1996, Kunze et al., 2006, Nagasawa et al., 2002, Polzin et al., 1995].

The dimensionless GM spectrum is proportional to

$$E(\alpha,\omega) = 2\pi^{-1}E\omega_i\mu^{-1}\omega^{-1}(\omega^2-\omega_i^2)^{-1/2} \tag{1.8}$$

where π is Archimedes's constant, ω is the frequency and

$$\mu = j_i\pi(\omega^2-\omega_i^2)^{-1/2} \tag{1.9}$$

with j_i being the equivalent number of wave modes. Observations were fitted with $j_i = 20, E = 2\pi\times10^{-5}$ [Garrett and Munk, 1972b, 1975].

Later, in 1981 Munk presented modifications to GM spectrum [Munk, 1981]:

$$S_{GM79}(\omega, j) = Eb^2 N_0^2 \frac{N(z)}{N_0} B(\omega) H(j) \tag{1.10}$$

where j is the vertical mode number, b is the e-folding scale of N^2 and $b = 1.3km$,

$$B(\omega) = \frac{2}{\pi} \frac{f}{\omega(\omega^2 - f^2)^{1/2}} \tag{1.11}$$

$$H(j) = \frac{1}{J} \frac{1}{j^2 + j_*^2} \tag{1.12}$$

$$\frac{1}{J} = \sum_1^\infty \frac{1}{j^2 + j_*^2} \tag{1.13}$$

where j_* parameter is directly related to the wavenumber bandwidth, a larger j_* correspond to increasing bandwidth,

Though there are several issues with this spectra. As Levine has pointed out [Levine, 2002], the GM spectrum at low latitudes does not fit the data at low frequencies, as well he has raised an issue with temporal variability and complex internal wave field in shelf seas because of the presence of nonlinear internal waves (NLIW) . Even thought the barotropic tide is regular, the energetics of NIW can vary in space in time, which lead to changes in spectral shape - there is more energy in high-frequencies and spectra have a "shoulder" near high frequencies, which is usually absent in the deep ocean, making it difficult to use GM spectrum in the shelf seas. To conclude, the GM spectrum could be useful for the open ocean, where most of the IWs are linear, but it is difficult to use GM at different latitudes, stratifications, depths, as it creates some inconsistencies between predicted and real values.

Internal wave energy spectrum on the shelf seas

After Garrett and Munk some scientists have tried to modify the energy spectrum, but we would like to concentrate on Levine spectra. Thirty years after Garrett and Munk proposed their energy spectra for the open ocean, a new modified spectral formulation was presented

by Levine that treats three problems which the GM formulation has: the normalisation of the energy spectrum as a function of frequency bandwidth, the energy distribution at frequencies below the semidiurnal tide, and the treatment of vertical boundaries and turning points [Levine, 2002].

The modified (by Levine) spectral energy distribution function looks as follows:

$$E_*(\omega,\theta,j) = E_{ref} B_*(\omega) H(j) \tag{1.14}$$

where E_{ref} is the constant energy per unit mass,

$$B_*(\omega) = \frac{\pi}{2}\frac{B(\omega)}{C}\begin{cases} 1, & \text{if } \omega_{s2} < \omega. \\ (1+\frac{f}{\omega_{s2}})\frac{(\frac{\omega}{\omega_{S2}})^3}{(\frac{\omega}{\omega_{S2}})^{2.5}+\frac{f}{\omega_{S2}}}, & \text{if } f < \omega < \omega_{s2}. \end{cases} \tag{1.15}$$

The normalisation to ω_{s2} frequency removes the f dependence of the spectral level at frequencies higher than ω_{s2}.

$$\int_{\omega_{S2}}^{N_{ref}} B_*(\omega) d\omega = 1 \tag{1.16}$$

$$C = arccos\frac{f}{N_{ref}} - arccos\frac{f}{\omega_{S2}} \tag{1.17}$$

Levine has tested this modified spectrum on observational data from different latitudes and on data from Coastal Mixing and Optics experiment (CMO) from 1997 in Mid-Atlantic Bight. However, in order to compare the calculations from modified spectra and observational data, they have used a stratification profile which was averaged through 30 days [Levine, 2002], therefore they might miss some variability of energy spectrum dependent on the shape and strength of stratification. Even though some progress was made in the field of low (M_2) frequency internal waves prediction, we still do not have a good parameterisation for high frequency internal waves and turbulence.

1.3.2 Mixing and turbulence

Richard Feynman has described turbulence as "the most important unsolved problem of classical physics". But in spite of it, most of us intuitively know the definition of turbulence, as we have seen it numerous times during our everyday life - in storm clouds, in water flowing from the tap, when waves are breaking at the surf zone, in smoke from chimney, even when we are putting milk in our tea and start stirring it, all of it contain turbulence. Turbulence is random fluctuations of flow and properties which is widely observed to occur in moving fluids and may be a combination of eddies of different scales, and it plays a key role in dynamics of the shelf seas by transferring heat, mass and momentum [Simpson and Sharples, 2012]. One of the most important properties is that turbulence generates large velocity gradients at small scales [Thorpe, 2005].

The first recognition of turbulence as a distinct fluid behaviour was at least 500 years ago by Leonardo da Vinci. The figure 1.8 shows the sketch which was found in da Vinci's book.

Turbulence is usually characterised by the following features:

- Irregularity

  Turbulent flows are always irregular, this is a reason why they are usually described statistically by using average properties.

- Diffusivity

  This characteristic is responsible for the increased rates of mass, momentum and energy transports.

- Vorticity

  Turbulent flows have strong 3D vorticity, these vortices are subjected to stretching, which is the core mechanism for the energy to be dissipated from large to small scales. The process continues until the small scale vortices are so small that their kinetic energy transforms into heat.

- Dissipation

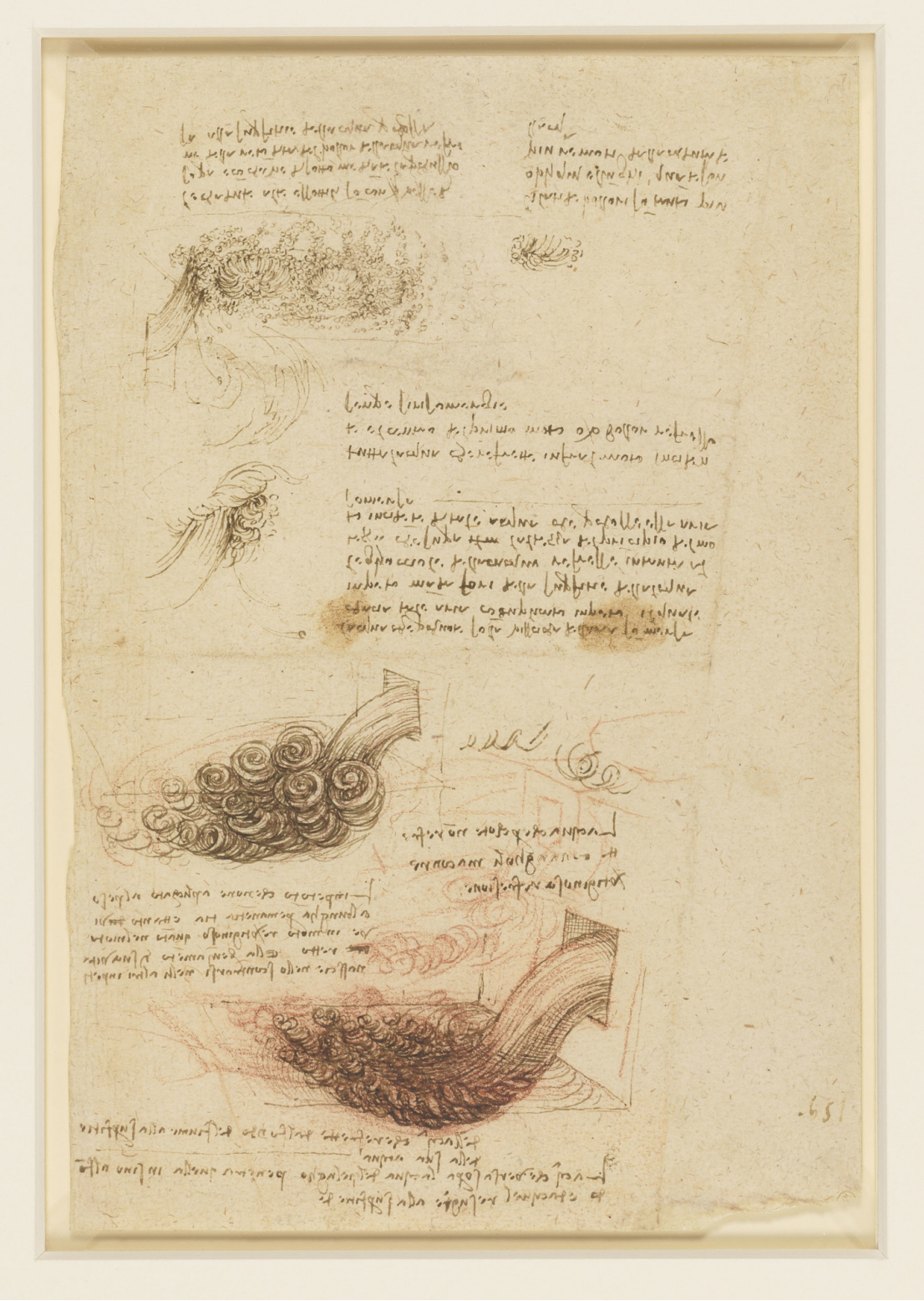

Fig. 1.8 The sketch of turbulent flow from Leonardo da Vinci [Royal Collection Trust]

In order to sustain turbulent flow, there is a need of energy supply because turbulence dissipates the kinetic energy rapidly. Most of the kinetic energy is contained in the large-scale, which is transferred to smaller scale and forms an energy cascade and this process continues if there is an available energy source.

The turbulence was mathematically described firstly by Osborne Reynolds on the basis of studying the flow of water in pipes: at low speed the dyed fluid followed straight line-laminar flow, at higher speed the flow was random - became turbulent. This is how Reynolds describes his observations, [Reynolds, 1883]: "The general results were as follows:

1. When the velocities were sufficiently low, the streak of colour extended in a beautiful straight line through the tube.

2. If the water in the tank had not quite settled to rest, at sufficiently low velocities, the streak would shift about the tube, but there was no appearance of sinuosity.

3. As the velocity was increased by small stages, at some point in the tube, always at a considerable distance from the trumpet or intake, the colour band would all at once mix up with the surrounding water, and fill the rest of the tube with a mass of coloured water. ...On viewing the tube by the light of an electric spark, the mass of colour resolved itself into a mass of more or less distinct curls, showing eddies."

The switch between laminar and turbulent conditions is controlled by the relation of inertial and viscous forces, which is now known as a Reynolds number (Re), $Re = \frac{U_w d}{\nu}$, where ν is the kinematic viscosity, about $10^{-6}\,\mathrm{m^2\,s^{-1}}$ for water, U_w is the speed of water and d is the diameter of a tube [Thorpe, 2005]. The critical Reynolds number of 10^4 is generally considered turbulent in the ocean, but sometimes the Reynolds number flows of the same order of magnitude could be found in the shelf seas.

Reynolds' experiment showed the first example of measured transition from laminar into turbulent flow. But not all transitions to turbulence could be determined by the Re, for example when the transition to turbulence involves buoyancy forces [Thorpe, 2005], like

internal waves. To describe turbulence in stratified flows the Gradient Richardson number Ri_g is used:

$$Ri_g = -\frac{g}{\rho}\frac{\frac{\partial \rho}{\partial z}}{(\frac{\partial u}{\partial z})^2} = \frac{N^2}{S^2} \tag{1.18}$$

where N^2 is the stratification and S^2 is the shear:

$$N^2 = -\frac{g}{\rho_0}\frac{\partial \rho}{\partial z} \tag{1.19}$$

$$S^2 = (\frac{\partial u}{\partial z})^2 + (\frac{\partial v}{\partial z})^2 \tag{1.20}$$

where u and v are velocity components in the east and north directions and ρ is the density profile.

When the shear increases in a stratified fluid there is a higher chance for the flow to become unstable. The Richardson number Ri defined above is always considered positive. A negative value of N^2 indicates unstable density gradients with active convective overturning, the magnitude of negative Ri is not generally of interest. The $Ri < 1/4$ is a necessary condition for velocity shear to overcome the tendency of a stratified fluid to remain stratified, and this is a point when the flow becomes turbulent [Howard, 1961, Miles, 1961].

In order to describe the turbulent flow the following method is usually used:

$$u_f = U_f + u'_f \tag{1.21}$$

This method is called Reynold's decomposition, which separates the flow, u_f, into mean flow component, U_f, and turbulent flow component, u'_f, where $\bar{u}' = 0$.

The same could be applied to any scalar property, like temperature or salinity:

$$s = S + s'; \bar{s}' = 0 \tag{1.22}$$

where S is the mean salinity component and s' is the turbulent salinity component.

If we will consider the flux of this scalar property:

$$F = (U + u')(S + s') \tag{1.23}$$

and apply $\bar{s'} = 0$ and $\bar{u'} = 0$:

$$\bar{F} = US + \overline{s'u'} \tag{1.24}$$

where the first term is due to advection and the second one is due to covariance of fluctuations [Simpson and Sharples, 2012].

Navier-Stokes equations:

$$\frac{\partial u_i}{\partial x_i} = 0 \tag{1.25}$$

$$\frac{\partial u_i}{\partial t} + u_j \frac{\partial u_i}{\partial x_j} = f_i - \frac{1}{\rho}\frac{\partial p}{\partial x_i} + \nu \frac{\partial^2 u_i}{\partial x_j \partial x_j} \tag{1.26}$$

where f_i is a vector representing external forces.

Each quantity can be split into time-averaged and fluctuating components (Reynolds-averaged Navier-Stokes equations, RANS):

$$\frac{\partial \bar{u}_i}{\partial x_i} = 0 \tag{1.27}$$

$$\frac{\partial \bar{u}_i}{\partial t} + \bar{u}_j \frac{\partial \bar{u}_i}{\partial x_j} + \overline{u'_j \frac{\partial u'_i}{\partial x_j}} = \bar{f}_i - \frac{1}{\rho}\frac{\partial \bar{p}}{\partial x_i} + \nu \frac{\partial^2 \bar{u}_i}{\partial x_j \partial x_j} \tag{1.28}$$

Multiplying (1.30) by density

$$\rho \frac{\partial \bar{u}_i}{\partial t} + \rho \bar{u}_j \frac{\partial \bar{u}_i}{\partial x_j} = \rho \bar{f}_i + \frac{\partial}{\partial x_j}\left[-\bar{p}\delta_{ij} + 2\mu \bar{S_{ij}} - \rho \overline{u'_i u'_j}\right] \tag{1.29}$$

where

$$\bar{S_{ij}} = \frac{1}{2}\left(\frac{\partial \bar{u}_i}{\partial x_j} + \frac{\partial \bar{u}_j}{\partial x_i}\right) \tag{1.30}$$

is the mean rate of strain tensor.

Since integration in time removes the time dependence, we will obtain:

$$\rho \bar{u_j} \frac{\partial \bar{u_i}}{\partial x_j} = \rho \bar{f_i} + \frac{\partial}{\partial x_j} \left[-\bar{p}\delta_{ij} + 2\mu \bar{S_{ij}} - \rho \overline{u_i' u_j'} \right] \tag{1.31}$$

where $-\rho \overline{u_i' u_j'}$ is known as the Reynolds stress tensor.

Turbulent Kinetic energy

Turbulence kinetic energy (E_T) is the kinetic energy associated with eddies. In Reynolds-averaged Navier-Stokes equations, the turbulence kinetic energy can be quantified by turbulent velocities:

$$E_T = \frac{1}{2} \left((u')^2 + (v')^2 + (w')^2 \right) \tag{1.32}$$

TKE can be produced by fluid shear, friction or buoyancy and transferred to smaller scales through energy cascade, and is dissipated by viscous forces at the Kolmogorov scale.

Diffusion rate, K_z is usually calculated as

$$K_z = \Gamma \frac{\varepsilon(z)}{N^2(z)} \tag{1.33}$$

where Γ is the mixing efficiency, which is equal to 0.2 [Osborne and Burch, 1980], ε is the dissipation rate of turbulent kinetic energy and N^2 is the buoyancy frequency.

Diapycnal mass flux, Q, is usually calculated as

$$Q = K_z \frac{\Delta\rho}{\Delta z} \tag{1.34}$$

where $\Delta\rho$ is the density difference between surface mixed layer and bottom mixed layer and Δz is the pycnocline's thickness.

Turbulent scales

Turbulence is transferring energy through the energy cascade from large to small scales. Richardson thought that turbulence consists of "eddies" of different sizes. The large eddies are unstable and break up generating smaller eddies, the kinetic energy of large eddy is divided into the smaller eddies. These smaller eddies experience the same process, dividing to even smaller eddies which take their energy. The energy is passed down from the large to smaller scales until reaching such a scale where the viscosity of the fluid can dissipate the kinetic energy into heat.

In 1941, Kolmogorov wrote that for very high Reynolds numbers, the small scale turbulent motions are statistically isotropic [Nikolaevich, 1941]:

$$\eta = \left(\frac{\nu^3}{\varepsilon}\right)^{\frac{1}{4}} \tag{1.35}$$

This is known as the Kolmogorov length scale, where ν is kinematic viscosity.

Kolmogorov spectrum is represented in the following way:

$$E(k) = C\varepsilon^{\frac{2}{3}}k^{-\frac{5}{3}} \tag{1.36}$$

where $C = 1.5$ is a Kolmogorov constant and k is wavenumber [Simpson and Sharples, 2012].

However, in a stratified environment the length scale is set by L_0 - the Ozmidov length, where the energy dissipation rate is related to the buoyancy forces:

$$L_0 = \left(\frac{\varepsilon}{N^3}\right)^{\frac{1}{2}} \tag{1.37}$$

where N^2 is buoyancy frequency [Ozmidov, 1965]. Here the buoyancy forces suppress the turbulence, therefore, turbulence can only exist in this environment if there is enough power to outcompete the buoyancy forces.

Turbulent processes have a large effect on the circulation in the longterm through changes in the density fields, modelling of mixing processes are not described by model equations, so

various parameterisations have to be used [Moshonkin et al., 2016]. It is important to know and understand turbulence in the ocean in order to predict ocean processes in models.

1.4 The problem statement

In order to solve the challenges, described in the Motivation section, two stages should be accomplished:

- The link from M_2 and M_4 frequencies to higher M_6, M_8 frequencies in different stratification scenarios.
- The link from the higher frequencies into turbulence and mixing by using the results from the MITgcm run and the results from the ocean microstructure glider in the Celtic sea.

We have a clear link from MITgcm model (chapter 2.1.1) to the in-situ point ST5 as we've saved the data in this point from MITgcm model for each minute - from these data APE and HKE could be calculated, but we do not have the dissipation rate data to estimate the generation propagation ratio.

We also have a link between OMG and in-situ through the APE, but it's still very tricky to estimate the dissipation rate just from APE. We need to find a better way to link this data to get some interesting results.

1.5 Aims and objectives

This PhD project is comprised from 3 main tasks:

1. Evaluate the mechanisms behind the generation of solitary waves on the European Shelf Seas.
2. Investigate the spatial homogeneity of the identified generation mechanisms and resultant internal wavefield.

3. Combine observational and model data - develop an improved understanding of contribution to internal mixing of solitary waves.

1.6 Thesis structure

In this chapter the basics of the shelf seas dynamics, internal waves and turbulence were presented. In the following chapter I would like to introduce the data which have been used in this research and methods which have been applied. In chapter 3 the results from our modelled data are presented. In chapter 4 the data from our model were combined with our observational data to find the dependency between different stratification scenarios and spectral slope shape. In chapter 5 the results of the observational data from ocean microstructure glider (OMG) are presented combined with the previous results found in the chapters 3 and 4. In chapter 6 the conclusion of all this information from this study and a discussion of their implications are presented.

Chapter 2

Methods

2.1 Data

In this research we are mainly focusing on the Celtic Sea, one of the widest sections of the Northwest European Shelf. There are several data sources, which have been used in this research and are located in the Celtic Sea: in-situ data from moorings, in-situ data from ocean microstructure glider (OMG) and modelled data from the very high-resolution MITgcm model. The figure 2.1 shows the location of the Celtic sea, our model domain and the locations of our observational data. The typical water depth in this region is around 150m increasing to the 4000m beyond the shelf-edge.

As was described in the subsections 1.3.1 and 1.3.2, the Celtic Sea is one of the most energetic and productive regions among shelf seas. Therefore, there is a higher possibility to see internal waves in our data and, due to its specific topography with sharp shelf break, large shelf sea area with complicated topographical features and canyons, strong tides and stratification, there is a chance that the internal wave field modelled with our high-resolution MITgcm model may be close to reality. Studies on the internal waves in the Celtic Sea have been carried out by [Holt and Thorpe, 1997, Hopkins et al., 2014, Palmer et al., 2015, Pingree and Mardell, 1985, Pingree et al., 1981, Vlasenko et al., 2014]. Each report internal waves originating near the shelf break during the summer months (July to September) when there was a developed stratification.

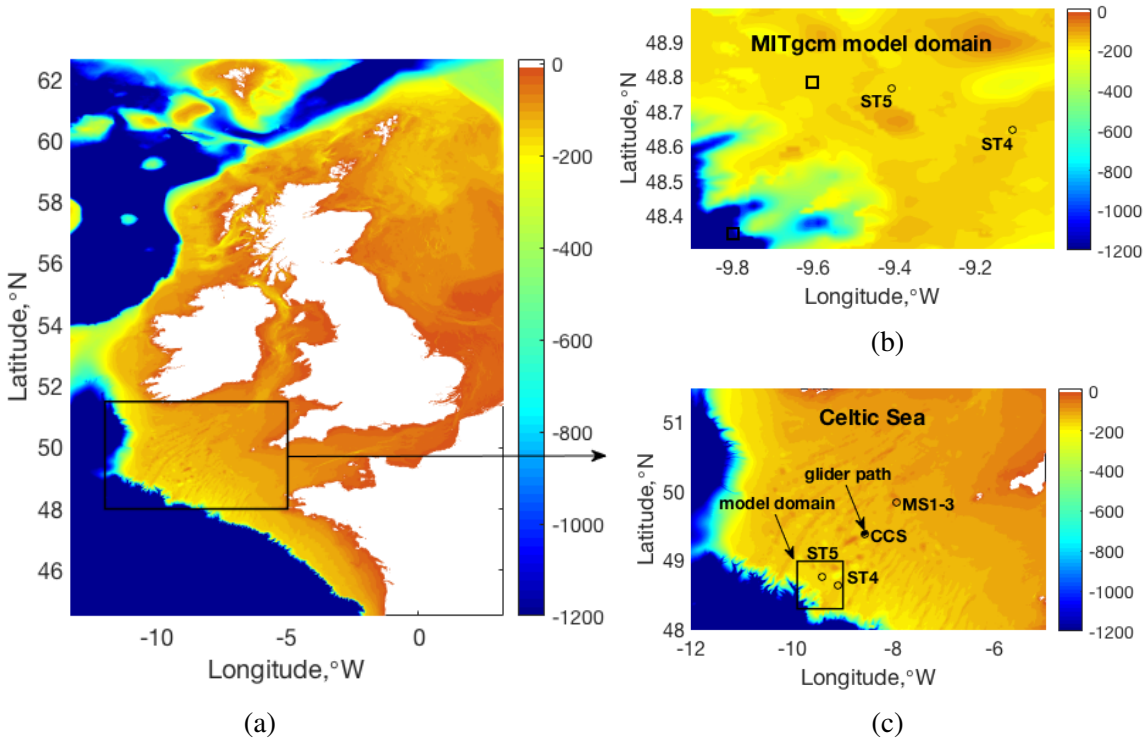

Fig. 2.1 (a) Map of UK and Ireland with local bathymetry for this region. Colours represent the depth in metres. (b) Map of the MITgcm model domain with two mooring locations - ST4 and ST5. Colours represent the depth in metres. (c) Celtic sea map with points ST4, ST5, CCS, MS1, MS2, MS3 showing the mooring positions and the model domain. Colours represent the depth in metres.

2.1.1 MIT General Circulation Model (MITgcm)

The MITgcm is a numerical model designed to study a wide range of processes in the atmosphere and ocean and it has a non-hydrostatic formulation which allows it to study processes from small to large scales - see the figure 2.2 [Marshall et al., 1997, MITgcm]. MITgcm is an open source code and freely available to all.

The modelled data from MITgcm configuration for the Celtic Sea with very high horizontal resolution were provided by Vasyl Vlasenko and Natalia Shaschuck, made especially for this research. To enable the production of high-frequency, short wavelength IWs, this configuration of the MITgcm model uses an ultra-fine grid with 50m horizontal resolution in both meridional and zonal directions over a region from 48.3 to 50.0N and from 9.0 to 10.0W, figure 2.1. The data from this model were stored each hour, apart from two locations,

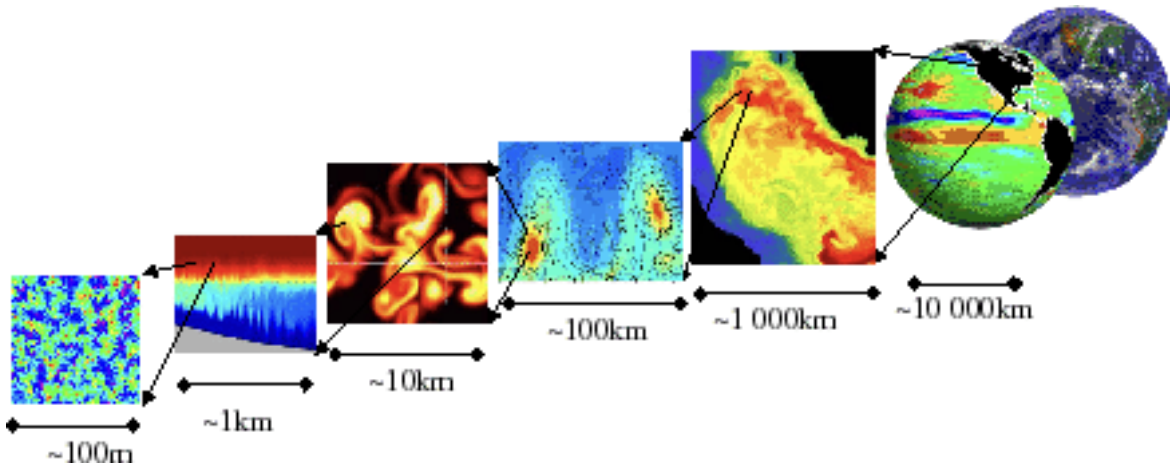

Fig. 2.2 MITgcm's non-hydrostatic capabilities, which allows it to model a wide range of processes - from convection on the left to global ocean circulation on the right [MITgcm].

Table 2.1 MITgcm data

Characteristic	Result
Hydrostatic	Non-hydrostatic
z-levels	25 layers (15 layers of 10m, deeper layers of 25m, 50m, 100m, 300m)
Fixed grid	yes
Domain size	80km in longitudinal and 100km in latitudinal scales
Resolution	50m
Initial conditions	temperature and density profiles from moorings ST4 and ST5
Bathymetry	GEBCO 30 arc-second global grid
Forcing	Tidal (M2 frequency, 12h)
Spin-up	12h
Boundary conditions	Sponge layer
Output resolution	T, U, V - 1min for ST4, ST5, 1h for the whole domain

ST4 and ST5, where they were stored each minute in order to validate our model with in-situ data and see the energy cascade from both data sources. There are 25 layers in a vertical direction, the first 15 layers have depth of 10m with deeper layers of 25m, 50m, 100m and 300m respectively. Some additional grid points were added in order to reduce reflection of internal waves from boundaries, which is called a sponge layer (for more information please check [Stashchuk and Vlasenko, 2017, Stashchuk et al., 2014, Vlasenko et al., 2013, 2014]).

Topography was used from the release of GEBCO 30 arc-second global grid of elevations (*GEBCO*2014*Grid* - www.gebco.net). Tidal forcing was added in the model by setting extra periodical terms in the right hand side of the momentum equation [Vlasenko et al., 2014].

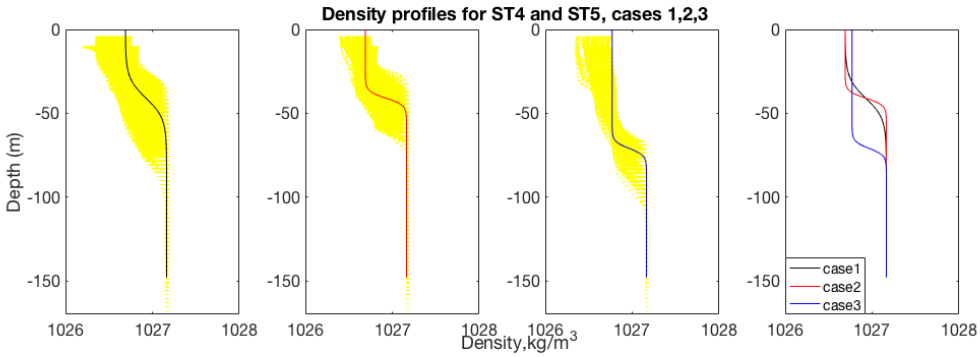

(a)

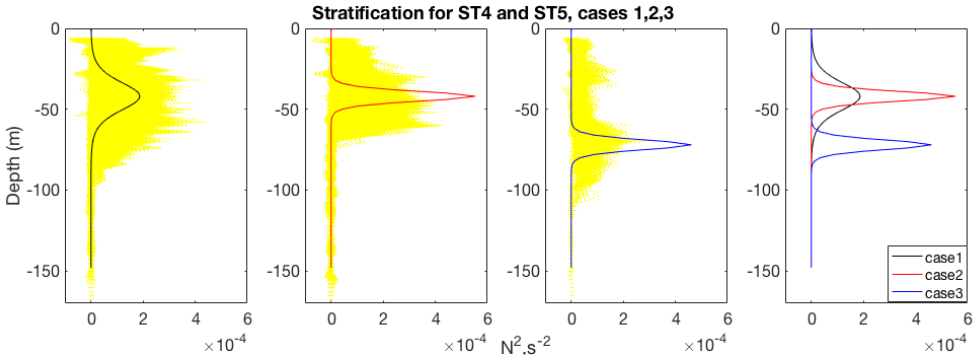

(b)

Fig. 2.3 Idealised density and stratification profiles for 3 basic scenarios: before storm - Normal (black colour), after wind mixing - Tight (red colour) and after storm - Deep (blue colour). Yellow colour represents observational data from points ST4 and ST5, separated into three cases. The N^2 profile has identical values for all three cases near the bottom at the range $136 - 150m$ and is equal to $10^{-5}s^{-2}$.

Initial stratification conditions were based upon temperature and salinity profiles collected from observations from two moorings described in [Hopkins et al., 2014], ST4 and ST5 (positions are shown on figure 2.1). The smoothed density profiles, figure 2.3, represent 3 typical scenarios:

Normal: typical summer conditions (black). The pycnocline is well established and primarily controlled by a temperature difference of around 8°C. The upper and lower limits

of the pycnocline change gradually towards a mixed upper and lower layer due to wind and tidal mixing.

Tight: windy summer conditions (red). Conditions are a modification of the Normal scenario, when enhanced summer winds introduce additional mixing energy at the limits of the pycnocline, resulting in tighter stratification.

Deep: storm-driven, deep pycnocline (blue). Here a deep, tight pycnocline is used to represent the dramatic change in structure that can be caused by strong levels of wind mixing that can punctuate otherwise calm summer conditions at temperate latitudes.

Figure 2.4 shows the temperature distribution at the 40m depth from the MITgcm output. The black line represents the shelf break region with 200m contour, white lines represent the local topographical features. From this figure it is possible to see the complexity of the internal wave field in this region and that the model recreates much of the natural variability observed in the shelf seas - from low to high frequency internal waves and solibores. The positions of two in-situ moorings ST4 and ST5 are also shown on the same figure. These moorings provide full water column temperature and current data collecting over 11.9 and 15.7 days in June 2012 respectively (Figure 2.4).

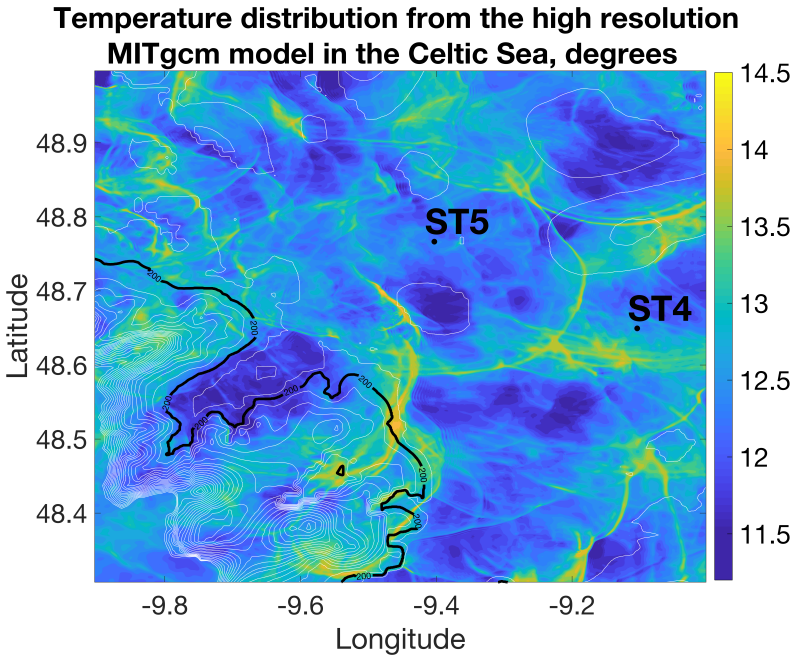

Fig. 2.4 Temperature (degrees) distribution at 40m depth from the high-resolution MITgcm model in the Celtic Sea. The black line represents 200m contour line around the shelf break area, whereas white thin lines represents topographical contour lines. Points ST4 and ST5 have been used for the model validation.

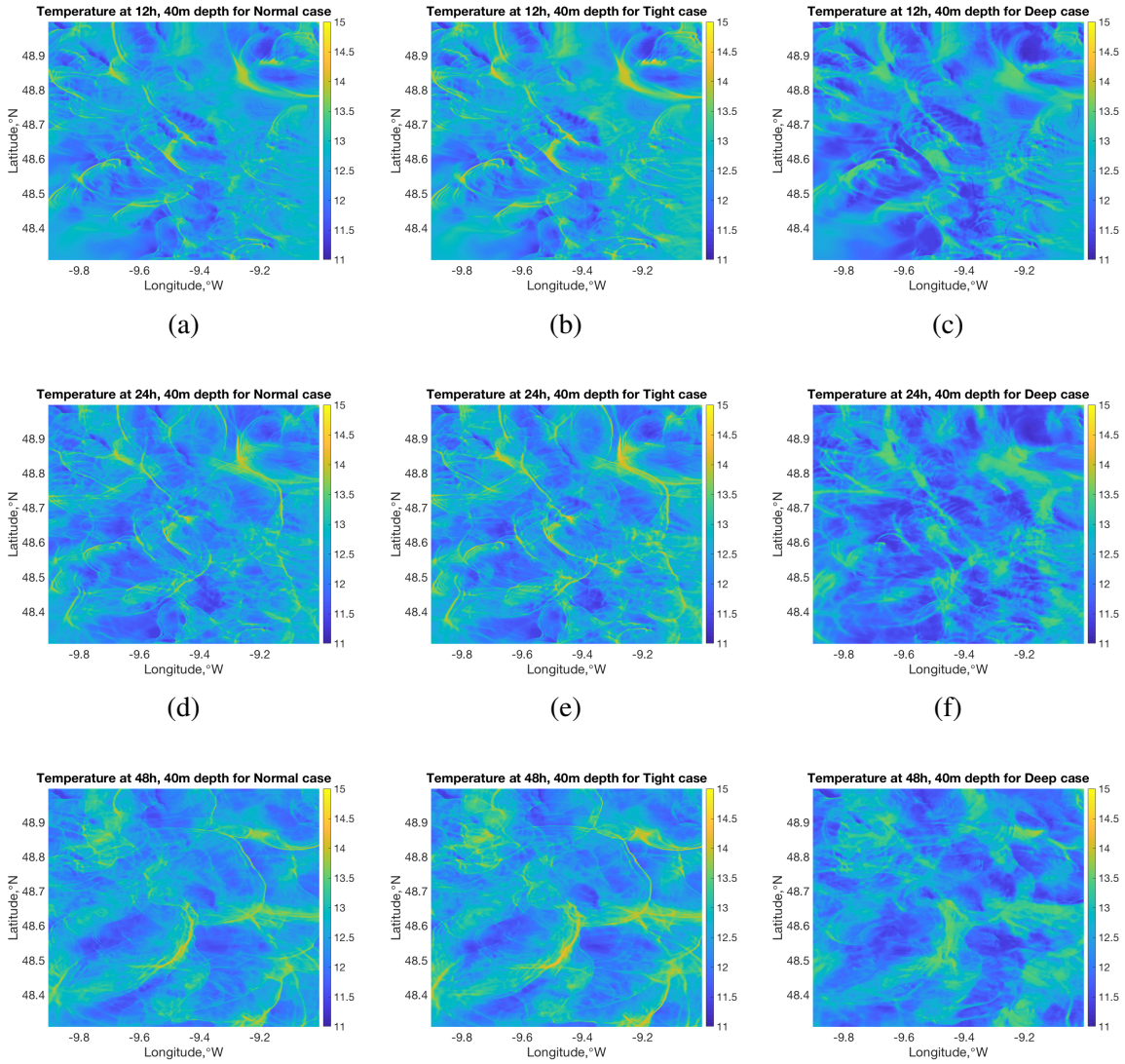

Fig. 2.5 Temperature (degrees) distribution at 40m depth from the high-resolution MITgcm model in the Celtic Sea for three different cases: a) Normal case at 12h, b) Tight case at 12h, c) Deep case at 12h, d) Normal case at 24h, e) Tight case at 24h, f) Deep case at 24h, g) Normal case at 48h, h) Tight case at 48h, i) Deep case at 48h.

Model data were stored each hour over the whole of the domain. Higher resolution data were collected at the corresponding locations of the ST4 and ST5 moorings, where data were stored each minute to enable better comparison with in-situ data (section 2.1.1). Figure 2.5 shows the temperature distribution at the 40m depth from the MITgcm output for three different cases (in columns) and at time steps 12h, 24h and 48h. These figures shows the evolution of IWs depend on initial stratification. By comparing the figures for 12h and 24h, it is possible to see that the system does not change much and the IW field is fully developed by 12h. Therefore, we will use the results from our model output starting from 12h.

Model validation

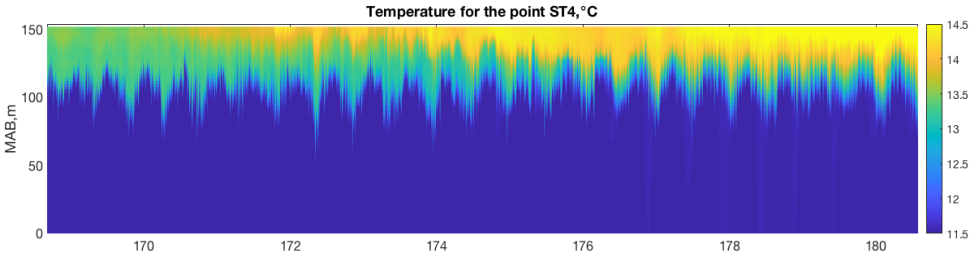

(a)

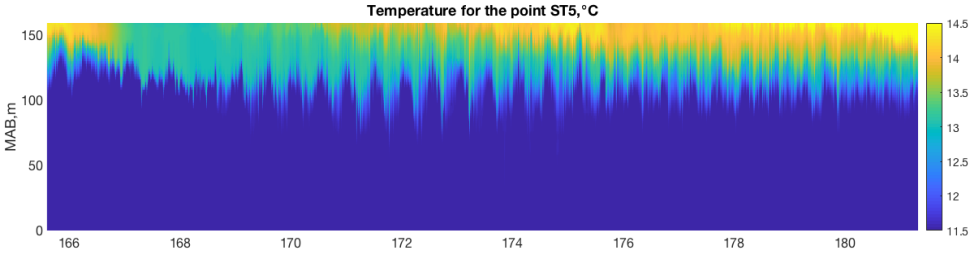

(b)

Fig. 2.6 In-situ data for the temperature distribution, points ST4 (top) and ST5 (bottom).

From the research of Hopkins et al., 2014, it has been shown that in the Celtic Sea, points ST4 and ST5 (figure 2.6), there were two main storms during summer 2012. The first storm starts on day 166 and lasts till days 168.5-169. The second storm begins on day 174-174.5 and dies on day 177. During the days 167-168 and 180-181.5 the idealised density profile was averaged and taken for the Deep case. On the days 167-168 the thermocline deepens

from 40 to 60m on ST5 and on the days 180-181.5 the thermocline deepens from 60 to 65m on ST5.

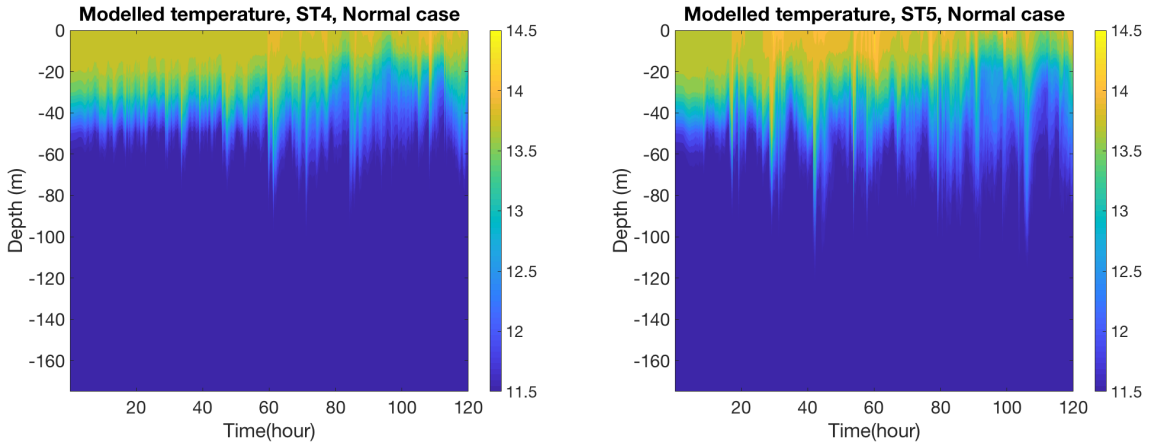

(a) (b)

Fig. 2.7 Modelled temperature distribution in points ST4 (left) and ST5 (right) for the Normal case.

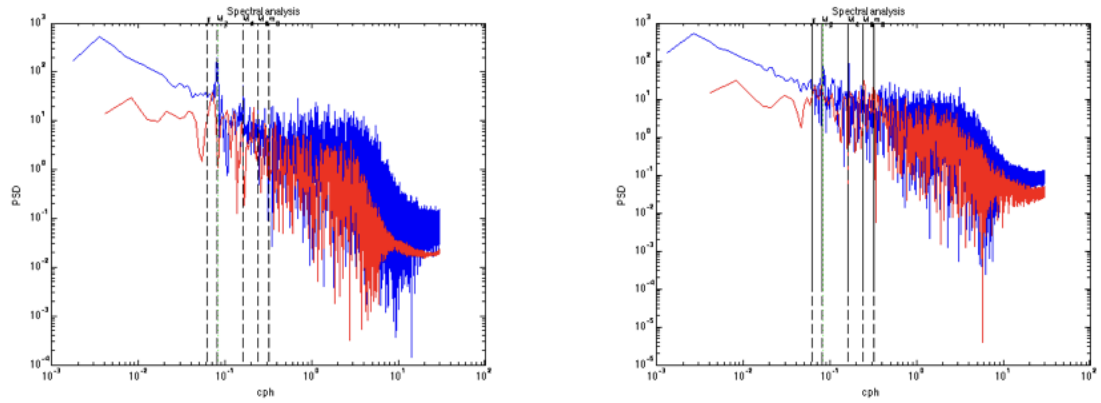

(a) (b)

Fig. 2.8 Spectral analysis of pycnocline displacement in points ST4 (left) and ST5 (right) for the Normal case, modelled (red) and in-situ (blue) data.

In order to make a comparative analysis of in-situ and modelled data, the data of temperature and salinity from two virtual points with positions of ST4 and ST5 has been recorded each minute. There are several figures for three different scenarios comparing modelled and in-situ data in points ST4 and ST5 (figure 2.7 for the Normal case, figure 2.9 for the Tight

case, figure 2.11 for the Deep case). In order to make a comparative analysis of in-situ and modelled data, the data of temperature and velocity has been analysed qualitatively.

In order to make a brief validation of the model versus in-situ data, the spectral analysis was made for both sites ST4 and ST5. Figure 2.8 shows the plots of spectral analysis of pycnocline displacement for ST4 and ST5 sites for modelled, red colour, and in-situ, blue colour, for the Normal case. There is some underestimation of the analogous potential energy mostly in higher frequencies, higher than M_8. As well, it is smaller in M_2 and M_4 frequencies, whereas it is overestimating the energy in M_6 and M_8 frequencies. This under- and over estimations are due to the fact that we are comparing here the Normal case with the sum of all three cases, as it is very difficult to decompose in-situ data exactly into those three cases, and because there is no wind forcing and fine-scale data for topography. From this we can conclude that the Normal case has lower amount of energy in M_2-M_4 frequencies and frequencies > M_8, whereas it contains more energy in M_6-M_8 frequencies.

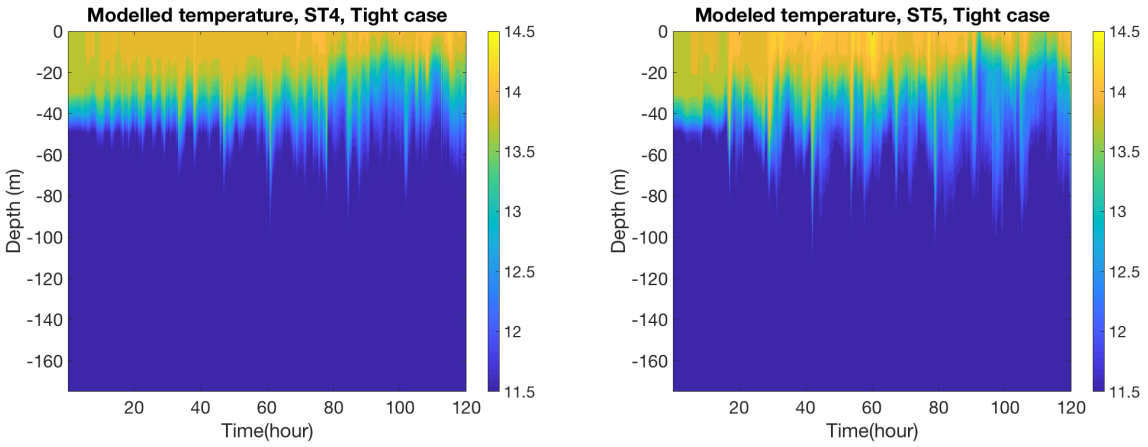

(a) (b)

Fig. 2.9 Modelled temperature distribution in points ST4 (left) and ST5 (right) for the Tight case.

The behaviour of two curves is almost the same - it has a sharp drop in energy after Vaisala-Brunt frequency, in case of ST5 the model is even closer to reality because of its location on research domain-in the centre, whereas ST4 is situated not far from the border and it is missing internal waves from eastern side, which leads to lower energy.

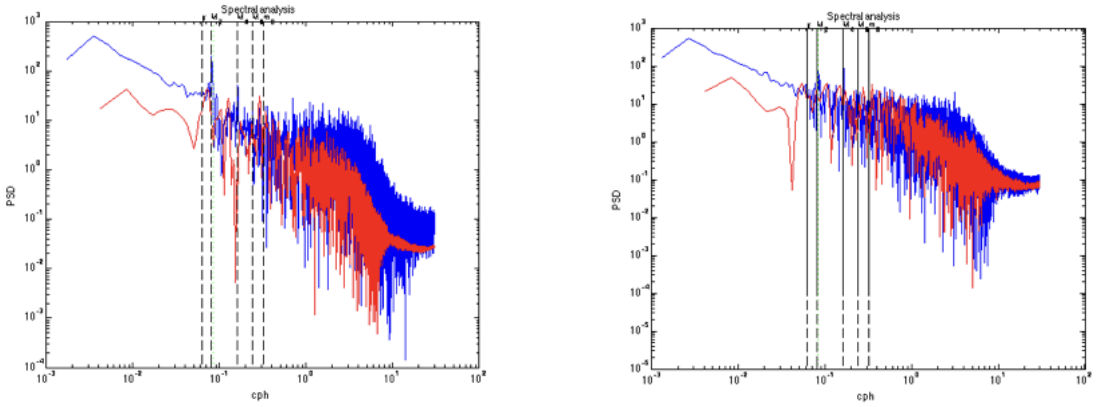

(a) (b)

Fig. 2.10 Spectral analysis of pycnocline displacement in points ST4 (left) and ST5 (right) for the Tight case, modelled (red) and in-situ (blue) data.

Figure 2.10 represents the spectral shape of pycnocline displacement for the modelled and in-situ for the points ST4 and ST5, where the modelled data are shown for the Tight case with wind mixing. The Tight case does contain more energy in lower frequencies than the sum of three cases - this is due to the fact that the tight pycnocline case could be only just a fraction from the whole time period in reality, but for the Tight case it was the normal state and during the whole period the pycnocline was tight there. But there is an underestimation of spectral density for ST4 in much higher frequencies, higher than M_8, which mean that even tighter pycnocline will not increase the spectral density in high frequencies closer to reality.

Figure 2.12 represents the spectral shape of pycnocline displacement for the modelled and in-situ for the points ST4 and ST5, where the modelled component shows the Deep case, after storm event. From this plot we can conclude that the case with tight and deep pycnocline does contain much more energy in low and higher frequencies than in reality, whereas there is still a small underestimation of energy in high frequencies. These results and inter-comparison of them gives very interesting ideas about the energy cascade of internal wave field and their behaviour in different stratification scenarios. For example, we can see that the Normal and Tight cases are coming close to the reality at the lower frequencies, whereas the Deep case is much better representing the high frequency representation.

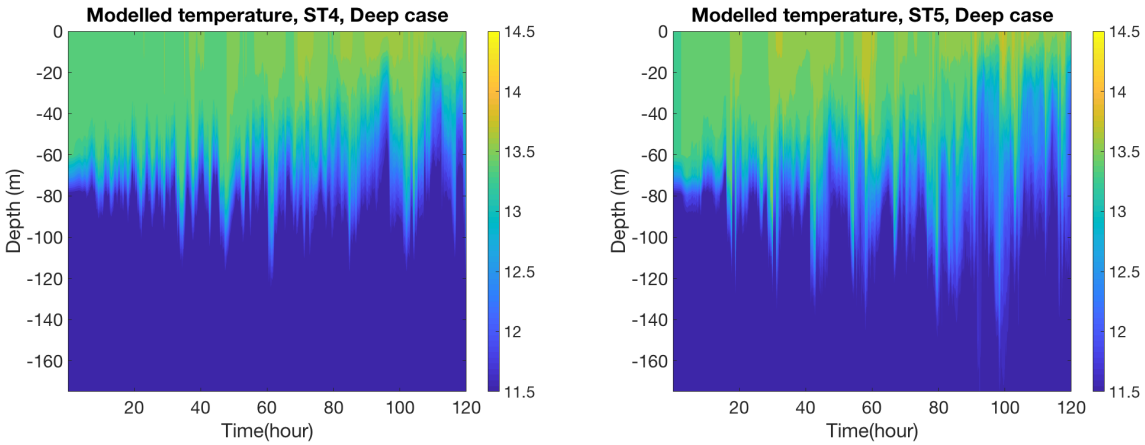

(a) (b)

Fig. 2.11 Modelled temperature distribution in points ST4 (left) and ST5 (right) for the Deep case.

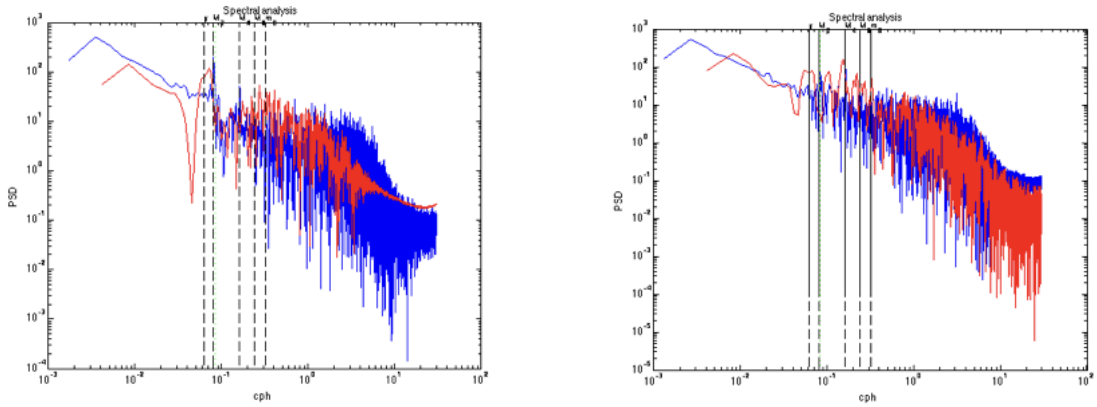

(a) (b)

Fig. 2.12 Spectral analysis of pycnocline displacement in points ST4 (left) and ST5 (right) for the Deep case, modelled (red) and in-situ (blue) data.

2.1.2 Mooring data

Observational data used in the following work were collected as part of three separate research programmes in the Celtic Sea (figure 2.1): the UK FASTNEt project (Fluxes Across Sloping Topography of the North East Atlantic), Oceans2025 and the UK Shelf Sea Biogeochemistry (SSB) programme. FASTNEt provides data from instrumentation attached to 2 moorings, identified as ST4 and ST5. Hopkins et al (2014) provide a thorough overview of data collected at these moorings along with analysis of hydrographic data. As well, 3

Table 2.2 Observational data

Characteristic	Result
ST4	
Location	48° 38.908' N; 09° 06.363' W
Duration	11.9 days (16-28 June 2012)
Mean depth	156m
ADCP	2m, 1min
T chain	2 – 20m, 1min
ST5	
Location	48° 46.138' N; 09° 24.378' W
Duration	15.7 days (13-29 June 2012)
Mean depth	169m
ADCP	2.5 m, 2min
T chain	2 – 20m, 1min
MS1	
Location	49.93° N; 7.95° W
Duration	19 days (5-24 July 2008)
Mean depth	70m
ADCP	2m, 1Hz
T chain	2 – 5m, 1min
MS2	
Location	49.9° N; 7.86° W
Duration	19 days (5-24 July 2008)
Mean depth	90m
ADCP	2m, 1Hz
T chain	2 – 5m, 1min
MS3	
Location	49.95° N; 7.78° W
Duration	19 days (5-24 July 2008)
Mean depth	140m
ADCP	4m, 1Hz
T chain	2 – 5m, 1min
CCS	
Location	49.4° N; 8.6° W
Duration	550 (T) and 450 (U) days (March 2014-July 2015)
Mean depth	145 m
ADCP	2m, 2.5 min
T chain	2.5 m, 5min

hydrographic moorings (MS1, MS2, MS3) were maintained at and around Jones Bank as part of the UK Natural Environment Research Council Oceans2025 strategic marine science programme. A thorough overview of data collected is available in Palmer et al., 2013. The SSB programme provides a 17-month long hydrographic time-series from the aptly named Central Celtic Sea (CCS) mooring [Wihsgott et al., 2019].

These moorings collected data in water typically around 140m, with the exception of data collected on Jones Bank, which was approximately $70-80$m at its shallowest point (MS1). All data used in this analysis is taken from strongly stratified summer conditions, when a strong pycnocline is formed in the upper water column. While moorings CCS and MS1, MS2, MS3 are situated within the mid-shelf region, ST4 and ST5 are located relatively close to the shelf break (40km on-shelf and 26km apart from each other, [Hopkins et al., 2014]), and are included in our model domain, as shown on the figure 2.1. They were deployed for 11.9 and 15.7 days in June 2012, and comprised of a full water column temperature chain with 1min sampling and bottom mounted 150kHz ADCP recorders with 2.5 m vertical bins and 2min sampling [Hopkins et al., 2014]. These allow us to resolve internal waves from low to high frequencies.

The moorings MS1, MS2, MS3 were deployed for 19 days from the 5th July to 24th July 2008 at and around Jones Bank and funded by the UK Natural Environment Research Council Oceans2025 strategic marine science programme. Three sites are spaced 10km apart from each other and located on the bank (MS1), on the bank slope (MS2) and at the base of the bank (MS3). Each mooring had a bedframe mounted RDI 300 kHz ADCP which recorded along beam velocities at 1Hz with a depth resolution of 2m (MS1), 2m (MS2) and 4m (MS3). Temperature was recorded on each station every minute and every 2m at the surface layers and every 5m at deeper layers. There were some failures in the ADCPs at MS2 and MS3, which gave us data only till the 12th July 2008. All data used in this analysis is taken from strongly stratified summer conditions, when a strong pycnocline is formed in the upper water column [Palmer et al., 2013].

The CCS mooring is situated in the Central Celtic Sea, giving its name CCS, and was collected as part of the UK SSB programme. It was chosen to be suitably distanced from

extreme topography of banks and the shelf break to be away from internal generation hotspots. These data combined with the Jones Bank data therefore represent as broad as possible coverage of IW conditions on temperate shelf sea. The CCS mooring has the longest time series among all observational points which are represented in this chapter and consists of more than 550 days in 2014-2015 for the temperature profiles and around 450 days for the baroclinic velocity profiles, due to ADCP failure [Wihsgott et al., 2019]. The average depth at this mooring is around 145m and this mooring is situated at about $70-80$km from ST5. This mooring had a bottom mounted 150kHz FlowQuest acoustic current profile (ACP) with a vertical resolution of 2m and temporal frequency of 2.5 min, and temperature-salinity (TS) chain with temporal resolution of 5min and vertical resolution of 2.5 m at the top and $5-20$m near bottom, which was linearly interpolated onto vertical resolution of 2.5 m throughout the whole water column [Wihsgott et al., 2019]. The CCS data series contains a lot of spring and neap cycles and storm events which allows us to find several examples to compare with MITgcm model. Some occasional short-term instrument failures result in data gaps that are evident in figure 2.18. The duration of the CCS time-series does still however provide our best opportunity of finding similar stratification scenarios to the three cases examined with the MITgcm model for direct comparison. Along with Jones Bank (MS1, MS2 and MS3) and FASTNEt data, it is therefore possible to examine differences in IW characteristics at a range of distances from topographical features - over a bank, near to a bank slope, close to the shelf-break and over the relatively smooth topography.

Near the shelf break: ST4 and ST5

Figures 2.13 and 2.14 show the distribution of barotropic and baroclinic velocity components and temperature through depth and time for stations ST4 and ST5. Velocity data from both moorings shows that data were recorded over the spring tide period, with the strongest tidal flows recorded around day 175. The slightly earlier deployment of the ST5 moorings resulted in ST4 missing a storm event at the beginning of the ST5 observational period, occurring on days 166-168 and pushing the pycnocline to around $40-50$m depth. This storm event is evident as increasing pycnocline depth and rapid cooling that is evident in temperature data

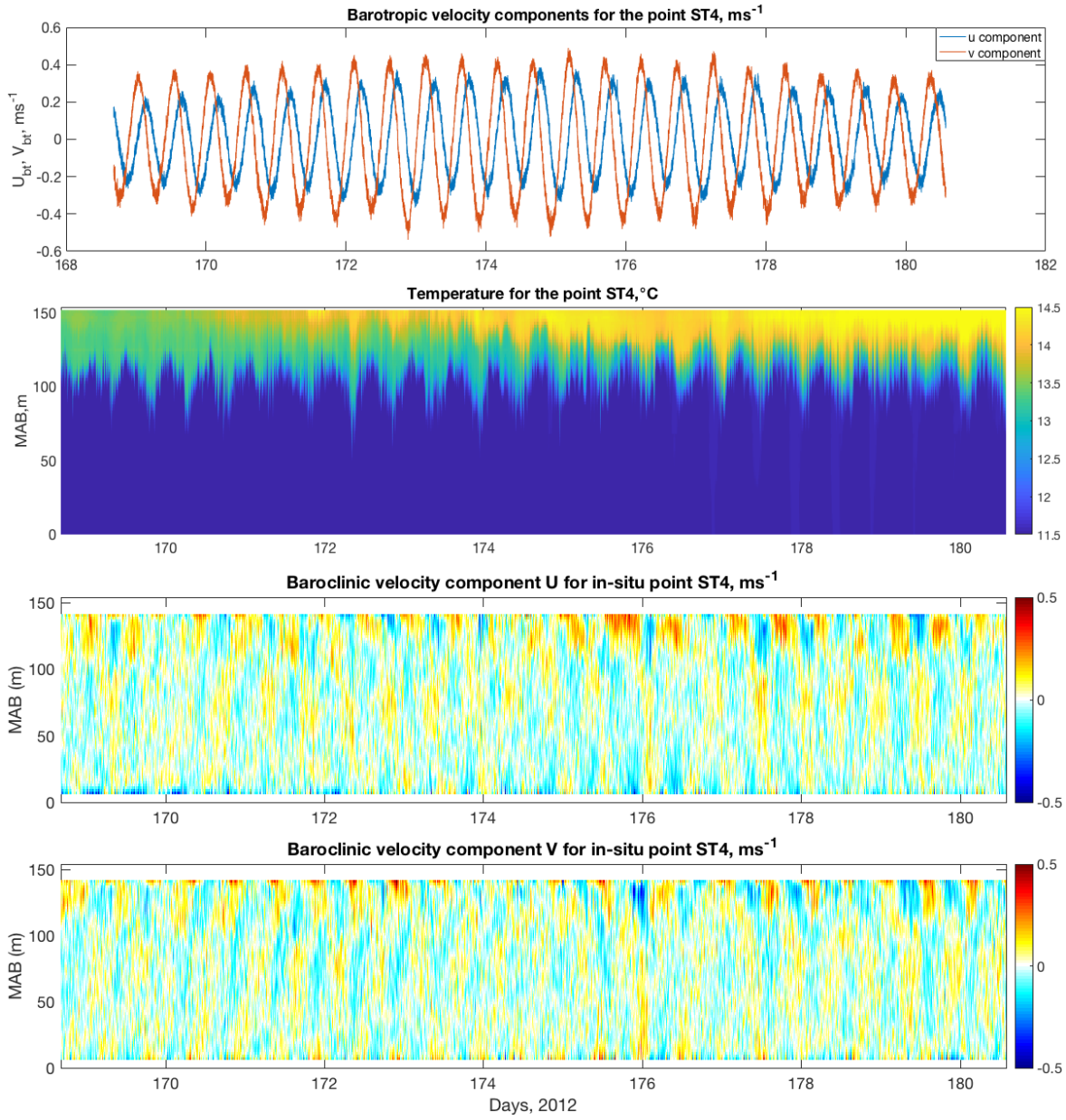

Fig. 2.13 ST4 data from top-bottom: Barotropic velocity components in the east direction (u_{bt}, blue) and north direction (v_{bt}, red). Temperature (°C) structure. Baroclinic velocity components in the east (u_{bn}) direction. Baroclinic velocity components in the north (v_{bn}) direction.

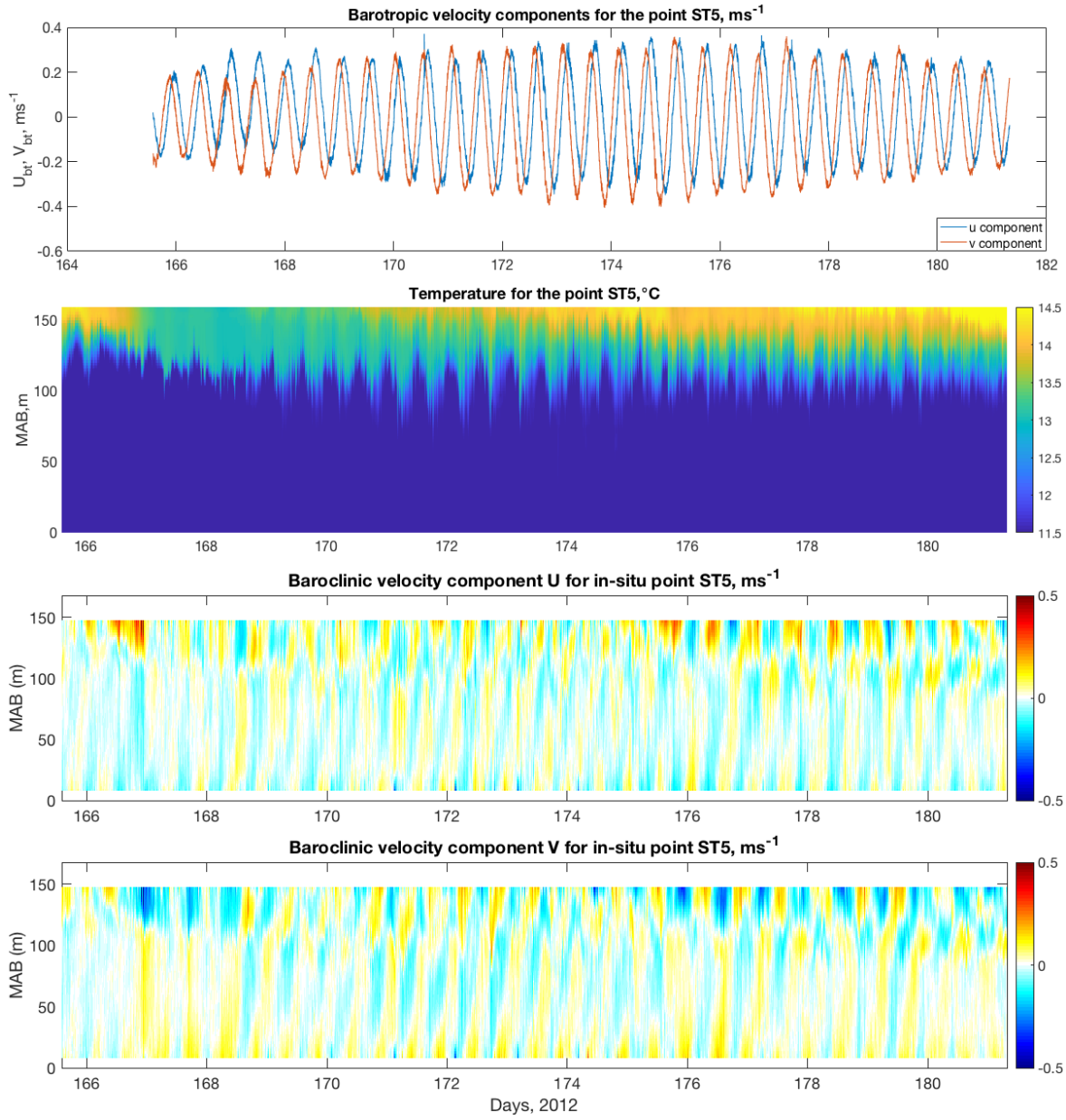

Fig. 2.14 ST5 data from top-bottom: Barotropic velocity components in the east direction (u_{bt}, blue) and north direction (v_{bt}, red). Temperature (°C) structure. Baroclinic velocity components in the east (u_{bn}) direction. Baroclinic velocity components in the north (v_{bn}) direction.

in Figure 2.14. These storm related data will later be compared with results from the Deep case MITgcm data, which represents post-storm conditions. Data from ST4 will be restricted to comparison with MITgcm Normal and Tight cases only. Following the storm, after day 168 surface temperature conditions slowly recover at both ST4 and ST5, with pre-storm conditions not being observed until after day 174. By day 176 thermal structure shows a far sharper and shallower pycnocline centred on depths of around 20m.

Barotropic components for the point ST4 range from $-0.35\,\mathrm{m\,s^{-1}}$ and $0.41\,\mathrm{m\,s^{-1}}$ for the u_{bt} component and $-0.55\,\mathrm{m\,s^{-1}}$ and $0.5\,\mathrm{m\,s^{-1}}$ for the v_{bt} component. Barotropic components for the point ST5 range from $-0.35\,\mathrm{m\,s^{-1}}$ and $0.37\,\mathrm{m\,s^{-1}}$ for the u_{bt} component and $-0.41\,\mathrm{m\,s^{-1}}$ and $0.37\,\mathrm{m\,s^{-1}}$ for the v_{bt} component.

MS1, MS2 and MS3 data

Data from Jones Bank moorings MS1, MS2, MS3 were collected for around 19 days from the 5th July to 24th July 2008 [Palmer et al., 2013]. These points were evenly distributed around 10km apart from each other spreading from the top, slope and off slope of the bank. Each mooring consisted of Acoustic Doppler Current Profiler (ADCP) and vertical chain of thermistors which were recording data each minute. Unfortunately there were some failures in ADCPs deployed at MS2 and MS3 resulting in shorter time-series at these locations.

MS1 was located close to the crest of Jones bank, which is around 30m above the surrounding flat topography. MS1 provides the most complete time series among from these deployments at around 19 days in total for both temperature and velocity. Figure 2.15 shows the distribution of barotropic and baroclinic velocity components alongside temperature structure at MS1 throughout this period. The extended duration of this deployment permits observation of spring and neap tidal phases. During this deployment there was a storm event around day 188 when average wind velocities were observed in excess of $10-15\,\mathrm{m\,s^{-1}}$ [Palmer et al., 2013]. This strong and sustained wind event is clearly identifiable in temperature data at MS1, producing high amplitude pycnocline fluctuations approaching 30m magnitude through days 188-190, equivalent to approximately 40% of the water depth. Enhanced baroclinic velocities u_{bn} and v_{bn} are also evident, particularly in the northerly

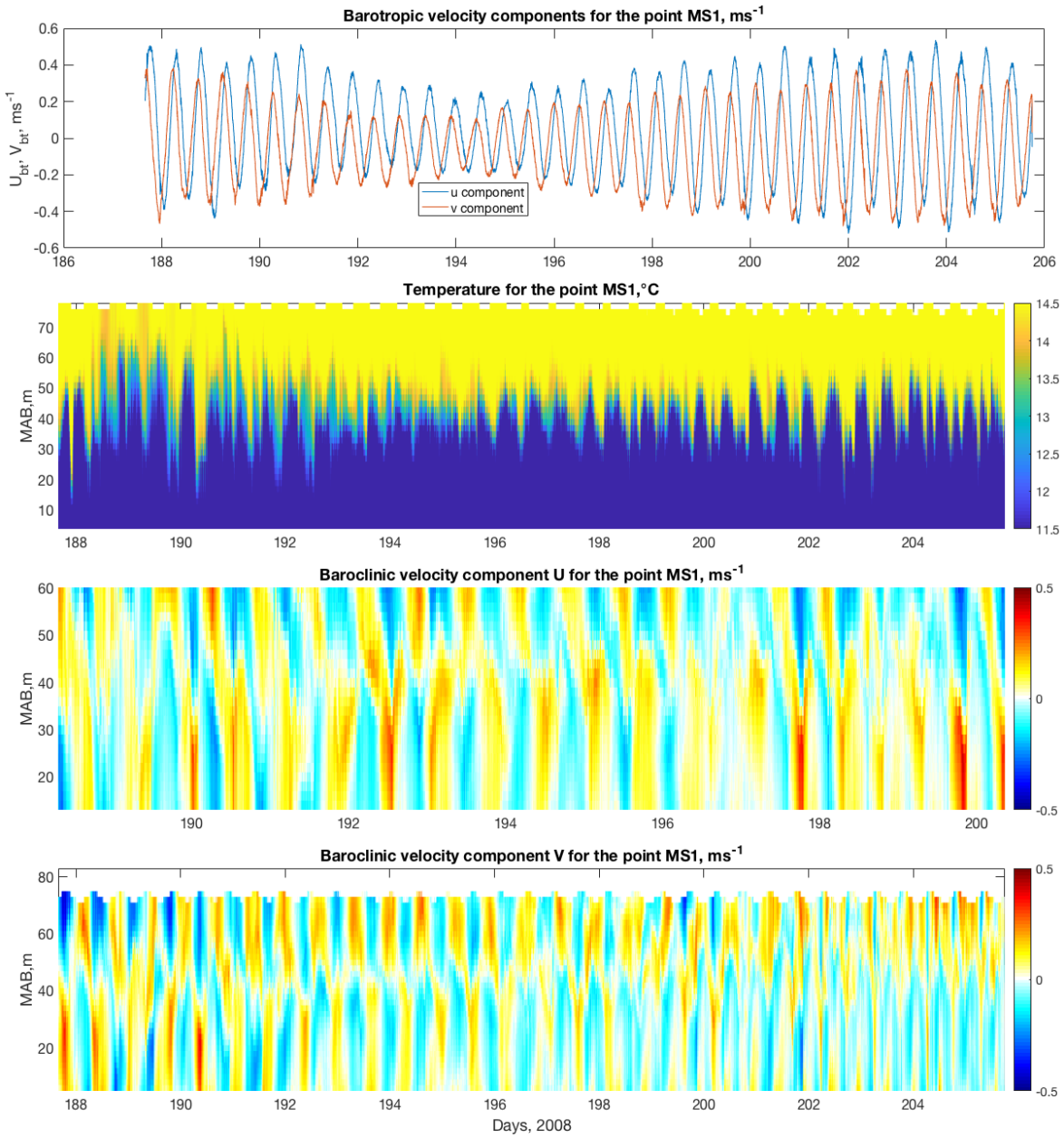

Fig. 2.15 MS1 data from top-bottom: Barotropic velocity components in the east direction (u_{bt}, blue) and north direction (v_{bt}, red). Temperature (°C) structure. Baroclinic velocity components in the east (u_{bn}) direction. Baroclinic velocity components in the north (v_{bn}) direction.

(v_{bn}) component during this time (Figure 2.15). Strong stratification exists throughout the time series ranging between $11-16$°C in bottom and surface waters, separated by a tight pycnocline. After day 188, when the storm began, there is increase in low-frequency IW amplitude, clearly evident in temperature data in figure 2.15, lasting beyond day 190. Following this period, as the tide transitions into a neap period, the observed IW field becomes less energetic and displacement amplitudes decrease significantly to $10-15$m maximum. The barotropic components for the point MS1 oscillate between $-0.2\,\mathrm{m\,s^{-1}}$ and $0.25\,\mathrm{m\,s^{-1}}$ for the neap cycle and from $-0.55\,\mathrm{m\,s^{-1}}$ to $0.55\,\mathrm{m\,s^{-1}}$ for the spring cycle, the u_{bt} component has higher for positive values (sometimes by $0.1\,-0.2\,\mathrm{m\,s^{-1}}$) amplitude compared to v_{bt} velocity component. The baroclinic components fluctuates between $-0.5\,\mathrm{m\,s^{-1}}$ and $0.5\,\mathrm{m\,s^{-1}}$.

The MS2 mooring was located on the slope of Jones bank [Palmer et al., 2013]. Due to the previously mentioned ADCP failure, the coincident current velocity and temperature time-series lasted for only approximately 8 days. Figure 2.16 shows the distribution of barotropic and baroclinic velocity components and temperature through depth and time for the point MS2. While the spring-neap cycles was not fully resolved, these data do still provide a range of energetic conditions as velocities reduce significantly throughout the period from critical strong spring-tide currents; from $-0.4\,\mathrm{m\,s^{-1}}$ to $0.5\,\mathrm{m\,s^{-1}}$ during peak flow reducing to $-0.2\,\mathrm{m\,s^{-1}}$ to $0.2\,\mathrm{m\,s^{-1}}$ as neap tides are approached. During storm event following day 188, the apparently disordered production of high amplitude IWs that were observed at MS1 are not identified. Instead, a series or high-amplitude IWs are observed are regular semi-diurnal periods during days 188-190, with displacement amplitudes of $30-40$m, accounting for similar $35-40\%$ of the whole depth as seen at MS1 (Figure 2.15). Towards the end of this time-series (days 191-193) IW amplitudes decreased substantially to around $10-15$m, again following similar behaviour to MS1. The baroclinic components of flow are relatively strong when compared to the barotropic tide, featuring similar magnitudes; peak currents between $-0.4\,\mathrm{m\,s^{-1}}$ and $0.4\,\mathrm{m\,s^{-1}}$ and $-0.5\,\mathrm{m\,s^{-1}}$ and $0.5\,\mathrm{m\,s^{-1}}$ for u_{bt} and v_{bt} velocity components respectively, and for the v_{bn} baroclinic velocity component there are

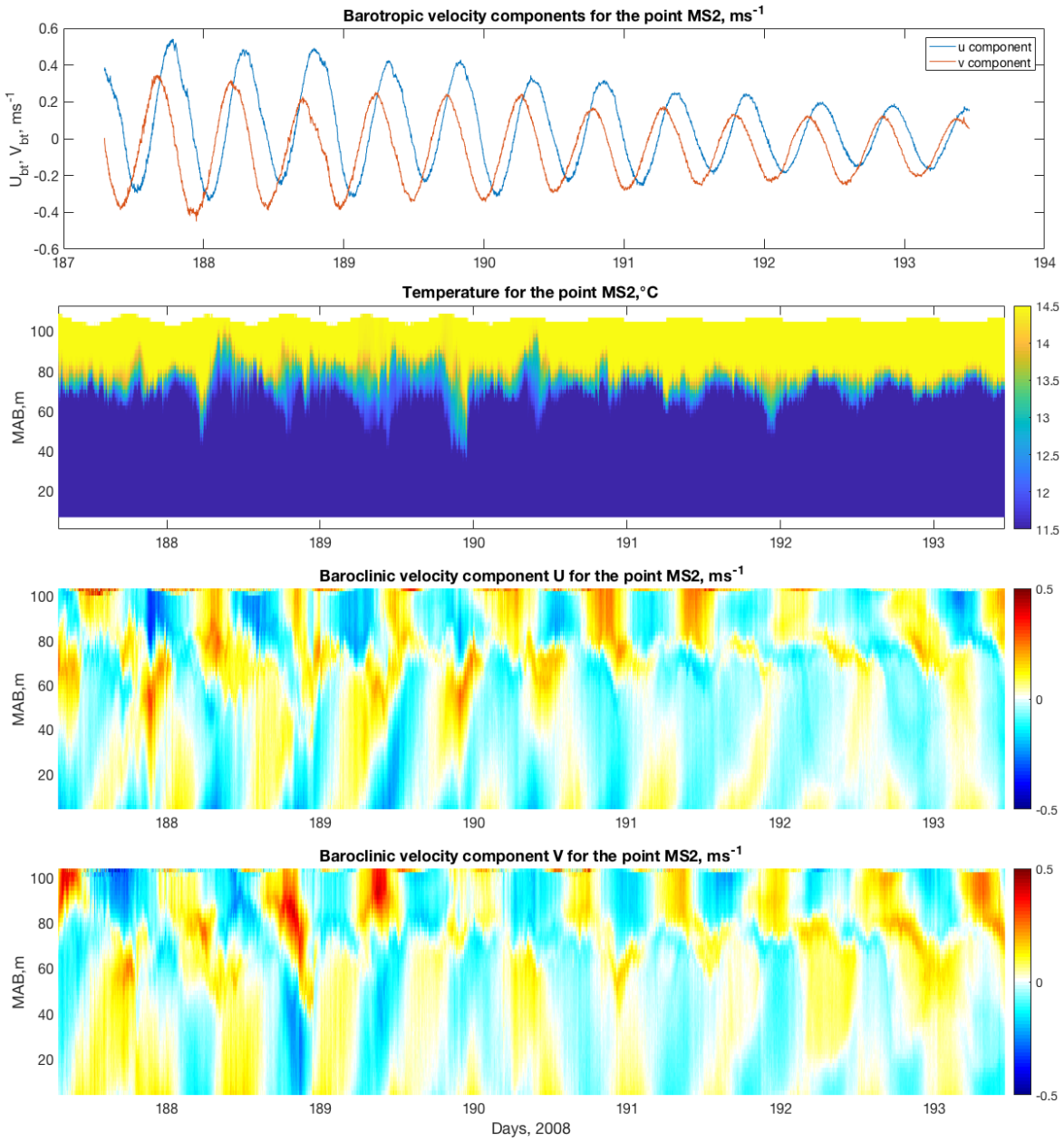

Fig. 2.16 MS2 data from top-bottom: Barotropic velocity components in the east direction (u_{bt}, blue) and north direction (v_{bt}, red). Temperature (°C) structure. Baroclinic velocity components in the east (u_{bn}) direction. Baroclinic velocity components in the north (v_{bn}) direction.

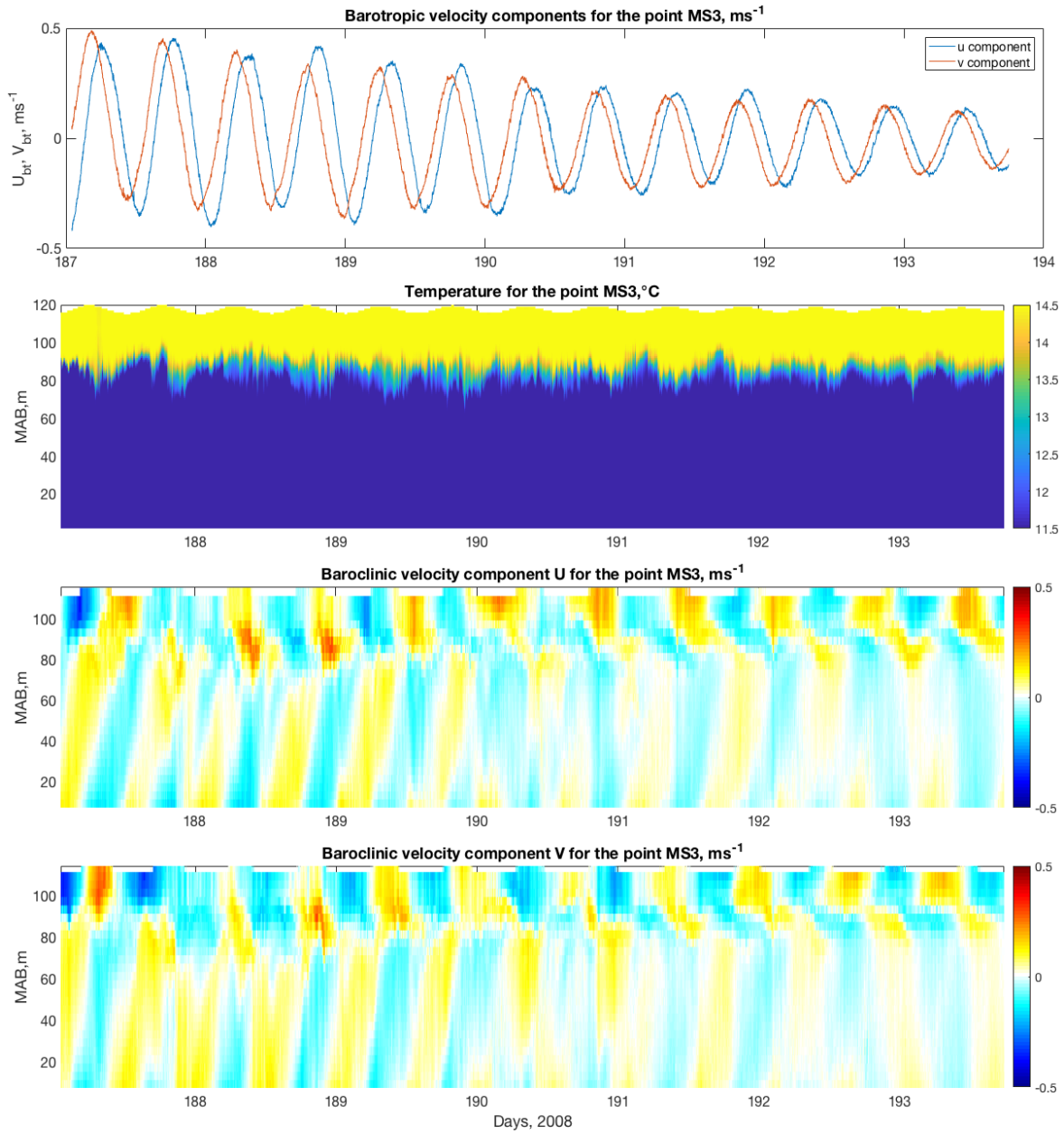

Fig. 2.17 MS3 data from top-bottom: Barotropic velocity components in the east direction (u_{bt}, blue) and north direction (v_{bt}, red). Temperature (°C) structure. Baroclinic velocity components in the east (u_{bn}) direction. Baroclinic velocity components in the north (v_{bn}) direction.

several times when it has reached the highest values, which coincided with the storm event after days 188-189.

The MS3 mooring was located just off slope of Jones bank, within 10km of MS2. A similar ADCP failure produced a similar length time-series to MS2, around 8 days in total. Figure 2.17 shows the distribution of barotropic and baroclinic velocity components and temperature through depth and time for the point MS3. Covering a similar period as MS2, this mooring produced a comparable subsection of the spring-neap cycle and covered a similar range of tidal current amplitudes; barotropic velocity amplitudes changed from $-0.45\,\mathrm{m\,s^{-1}}$ to $0.5\,\mathrm{m\,s^{-1}}$ during peak flow, close to spring tides, and from $-0.25\,\mathrm{m\,s^{-1}}$ to $0.25\,\mathrm{m\,s^{-1}}$ as tides approached neaps. The reduction in IW pycnocline displacement compared to MS1 and MS2 is immediately evident in temperature data. Despite this, IWs are still significant with amplitude fluctuations during the storm event reaching up to 20m on day 188 during the strongest observed winds, less than 17% of the whole water depth at this location and significantly less than that observed on the bank. Baroclinic velocity however remains strong with magnitude as high as $0.5\,\mathrm{m\,s^{-1}}$, similar to MS1 and MS2.

CCS data

The CCS mooring is situated in the Central Celtic Sea in a depth of 143m (fig. 2.1), CCS is located over 70km on shelf from ST5 and is suitably distanced from extreme topography to be considered away from points of active IW generation. These data consists of more than 550 days in 2014-2015 for the temperature distribution and around 450 days for the baroclinic velocity distribution [Wihsgott et al., 2019]. This data series covers numerous neap cycles and full variability in meteorological forcing, including storm events. This allows us to find several good examples for all MITgcm cases in observational data.

Figure 2.18 shows the distribution of barotropic and baroclinic velocity components and temperature through depth and time for the point CCS. The barotropic components for the point CCS typically oscillate between $0.45\,\mathrm{m\,s^{-1}}$ peak magnitude during spring tides and $0.25\,\mathrm{m\,s^{-1}}$ magnitude during neap tides. Baroclinic velocity is again, of similar order with regular occurrences of $0.5\,\mathrm{m\,s^{-1}}$ magnitude. The full seasonal coverage of this time-series

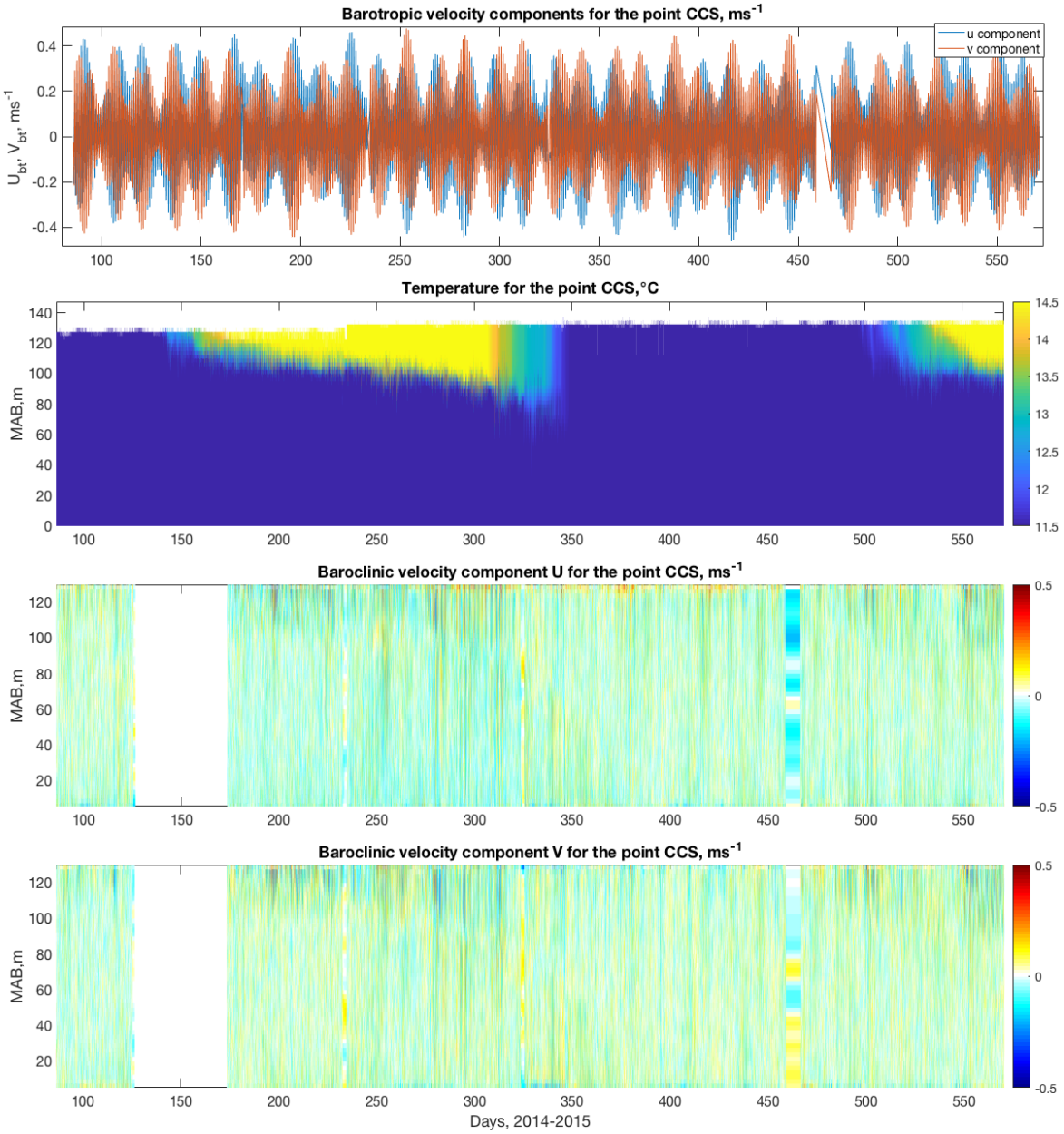

Fig. 2.18 CCS data from top-bottom: Barotropic velocity components in the east direction (u_{bt}, blue) and north direction (v_{bt}, red). Temperature (°C) structure. Baroclinic velocity components in the east (u_{bn}) direction. Baroclinic velocity components in the north (v_{bn}) direction.

provides opportunities for examining summer and post storm conditions that are analogous to those represented by Normal, Tight and Deep cases during MITgcm simulations presented earlier. Only data collected during strongly stratified conditions will be considered to best relate to these model results, covering the early summer period.

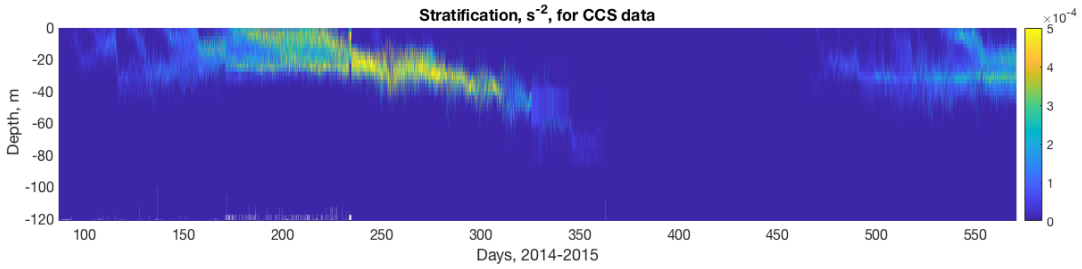

Fig. 2.19 Stratification for the CCS data, N^2, s^{-2}.

Figure 2.19 shows the vertical distribution of buoyancy frequency for the point CCS. The stratification varies between 0 and $5 \times 10^{-4}\,\mathrm{s}^{-2}$. The most interesting period for this study was during the days 250-320, because the depth of the pycnocline has increased by 40m, which is around 30% of the whole depth at this point.

2.1.3 Ocean microstructure glider (OMG) data

Ocean gliders are autonomous underwater vehicles that move up and down through the water by adjusting their buoyancy and collecting data on the way, check [Palmer et al., 2015] for technical details. The OMG data were collected during the UK Shelf Sea Biogeochemistry programme [SSB].

The glider was deployed around $5-10$km from the CCS mooring which is 120km far from the shelf break region. The depth in this region is 140m. The glider recorded for two weeks, from 15th July till 31st July 2015, figure 2.20. The OMG was measuring shear microstructure and corresponding density structure, thee data were used to find the dissipation rate of turbulent kinetic energy ε, more information could be found in Palmer et al paper [Palmer et al., 2015], where they have shown methods employed to provide trustworthy turbulent parameters.

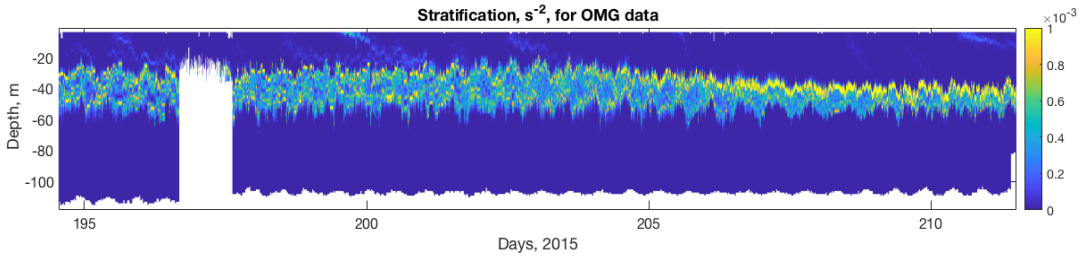

Fig. 2.20 Stratification for the OMG data, N^2, s^{-2}.

The MITgcm model does not have the turbulence and mixing which could be found in reality, therefore, in order to find the link between three different scenarios and turbulence the OMG data were used with a combination of CCS data.

2.2 Methodologies for data analysis

2.2.1 Slope criticality

Behaviour of normally incident internal waves approaching a shelf slope from offshore can be predicted from the ratio of the topographic slope to the internal wave characteristic slope [Hall and Carter, 2011]. The slope criticality is calculated only using the buoyancy frequency above the seabed, following the methods described in papers from [R. Stephenson Jr. et al., 2015] and [Zarroug et al., 2010], where the depth mean values of N^2 are used. To calculate the slope criticality, the following equations have been used:

$$\alpha = \frac{s_{topog}}{s_{wave}} = \frac{\partial H/\partial x}{\sqrt{(\omega^2 - f^2)/(N^2 - \omega^2)}}, \tag{2.1}$$

where s_{topog} is topographical slope, s_{wave} is internal wave characteristic slope, H is total depth, x is across-slope distance, ω is the angular frequency of internal waves, f is the Coriolis frequency and N^2 is the buoyancy frequency. If $\alpha < 1$, then the regime is subcritical, which means that slope generated internal waves will travel onto the shelf. If $\alpha > 1$, then the regime is supercritical, which means that the internal waves will be mostly reflected back from the slope. In case of $\alpha = 1$ - the regime will be critical, the linear theory is broken

down, which leads to nonlinearity, most of the internal waves will be broken down and the energy will go to turbulent mixing [Hall and Carter, 2011].

2.2.2 Froude number

The Froude number (Fr) is a dimensionless number defined as the ratio of a characteristic fluid velocity U_0 and the gravity wave speed c_p, named after William Froude:

$$Fr = \frac{U_0}{c_p}, \tag{2.2}$$

where U_0 is tidal speed and c_p is the internal wave phase speed [Vlasenko et al., 2005].

When $Fr < 1$, the regime is considered subcritical, pycnocline displacements generated as flow passes over topography result in the generation of internal waves at the same frequency as the forcing velocity, producing an internal tide, and flow is linear. When $Fr = 1$, the regime becomes critical, nonlinearity becomes important resulting in the generation of lee waves, tidal bores and solitary internal waves [Vlasenko et al., 2005]. As the fluid speed exceeds the wave speed and $Fr > 1$, the regime becomes supercritical. In such cases highly unstable lee waves are generated that will likely break, losing significant amount of their energy locally with some additional energy escaping as solitary internal waves [Vlasenko et al., 2005].

2.2.3 Available potential energy (APE)

The available potential energy (APE) represents the potential energy that is available from the wave disturbance relative to the water column at rest [Moum et al., 2007]. In order to calculate this energy we have used the equation 1.7.

The definition of the reference density you could see on the figure 2.21, where the area of ADC is equal to the available potential energy. In our case the reference density profile was calculated as an average in a tidal (M_2) period. The APE results were integrated through depth and averaged through time. There are still some difficulties in calculation of reference density state because the system is not in equilibrium during our measurements. In our

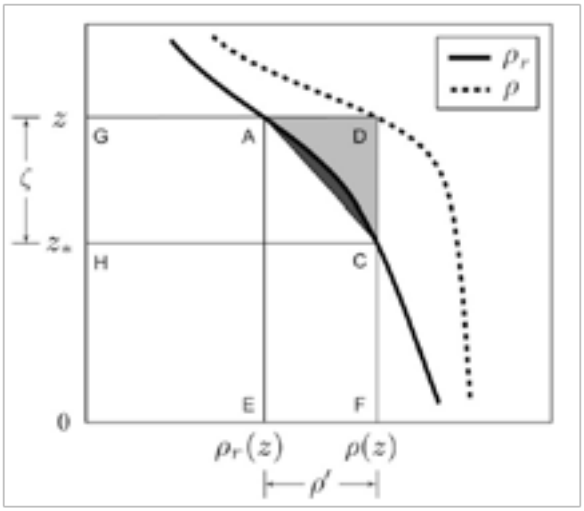

Fig. 2.21 Schematic diagram depicting the different formulations of the APE density.

research we have tried to improve the calculation of the reference state. We have calculated two different APE with two different reference states: the first method - reference state was calculated with a moving window average equivalent to the tidal M2 period (method 1), the second method - reference state was calculated by finding the APE between each two densities in M2 window (method 2).

The results of APE calculations could see on the figure 2.22. As you could see, there is a huge difference between these two APEs, our method is highlighted by red colour. We still need to explore some questions concerning how better our new method is, does is bring less error in a total energy budget calculation, which would be answered during following years.

2.2.4 Horizontal kinetic energy (HKE)

Horizontal kinetic energy (HKE) was calculated by using the following equation:

$$HKE = \frac{1}{2} \cdot \rho \cdot (u(z)^2 + v(z)^2), \tag{2.3}$$

where u and v are velocity components in the east and north directions and ρ is the density profile.

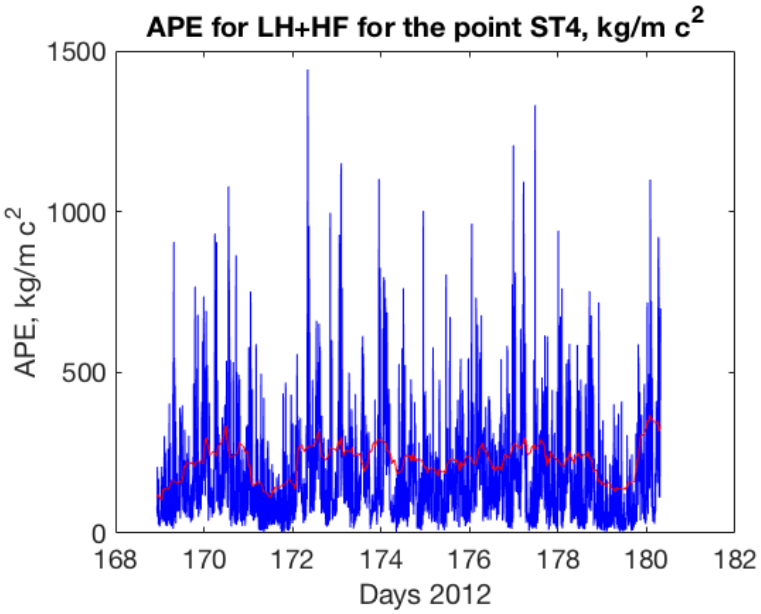

Fig. 2.22 Available potential energy for low (If+M2) + high (M4-N) frequencies calculated with two different methods, an the example of the ST4 data, 1st method - blue and 2nd method - red colour.

2.2.5 Modal structure

Modal decomposition of the internal tide energy flux is accomplished from least squares fits of U_0 to vertical normal modes [Dushaw et al., 1995, Nash et al., 2005]. The in-situ data of U and V components of velocity for ST4 and ST5 sites have been used in order to find the first five modes of internal waves velocities. Our observation data are more complex compared to the MITgcm model.

Most of the time the highest baroclinic energy is sitting in the first mode and it is considered as a dominant mode. Figure 2.23 shows the effect of storm events on the baroclinic energy in the 1st mode. The interesting thing is that the majority of these two peaks are coming from the 1st mode, other modes are not affected by storm in a such strong way, but there are some peaks in the 3rd and 4th modes.

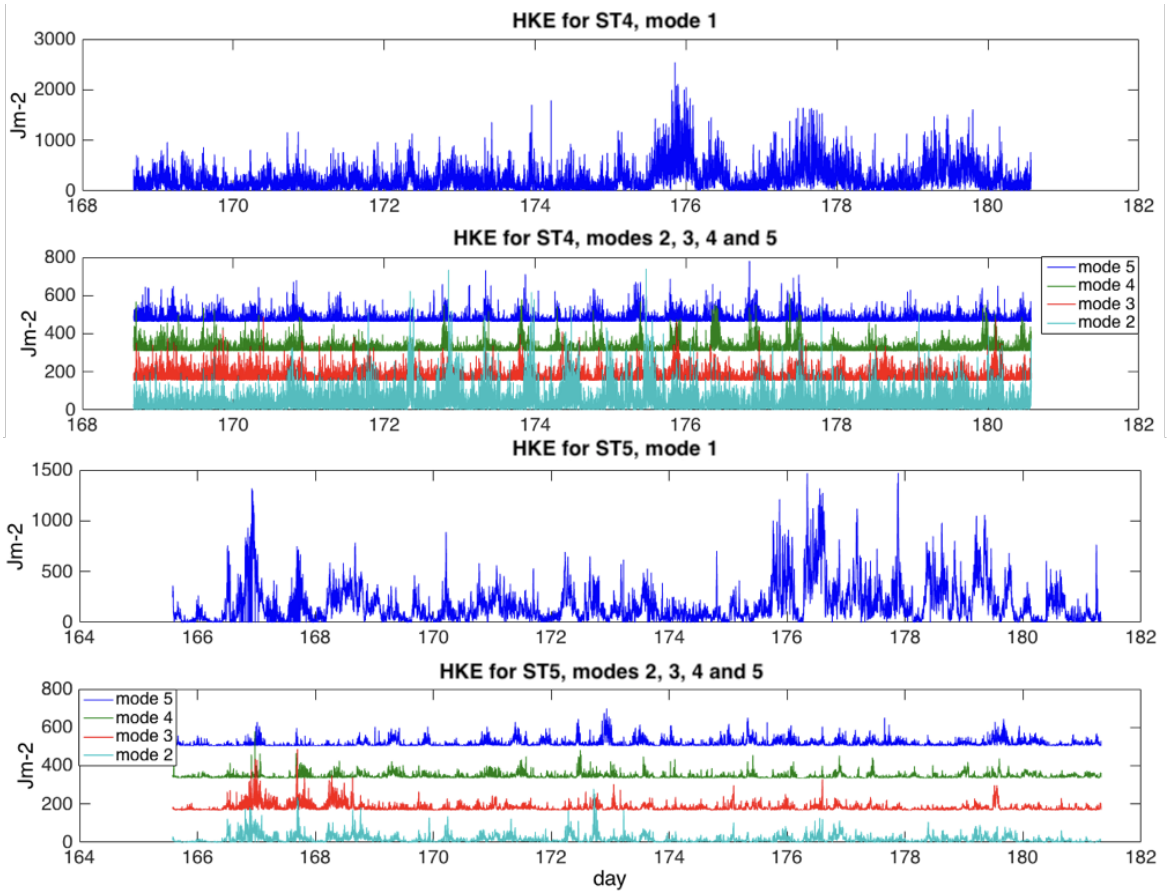

Fig. 2.23 HKE for different modes for points ST4 and ST5

2.2.6 Richardson number

The gradient Richardson number, Ri_g, is always considered positive for the investigation of shear instability. A negative value of N^2 indicates unstable density with active convective overturning.

The $Ri_g < 1$ is a necessary condition for mixing and turbulence, when shear overcomes stratification, and is considered as a marginal stability criterion [Mack and Schoeberlein, 2004, St. Laurent and Schmitt, 1999].

Another type of Richardson number is the bulk Richardson number, Ri_b. The Ri_b is an approximation of the Ri_g number. The Ri_b is a dimensionless ratio between stratification and shear, which are determined between the top and the bottom of pycnocline. It is usually used to show the formation of turbulence.

$$Ri_b = \frac{N_b^2}{S_b^2}, \tag{2.4}$$

where N_b^2 is the bulk stratification and S_b^2 is the bulk shear, which are analogous to the maximum characteristics of N^2 and S^2 divided by the thickness of pycnocline:

$$N_b^2 = -\frac{g}{\rho_0}\frac{\rho_{bottom} - \rho_{top}}{\Delta z}, \tag{2.5}$$

$$S_b^2 = (\frac{u_{bottom} - u_{top}}{\Delta z})^2 + (\frac{v_{bottom} - v_{top}}{\Delta z})^2, \tag{2.6}$$

where Δz is the pycnocline thickness and top and bottom are the pycnocline boundaries. The pycnocline boundaries were based on the stratification data, the top and bottom of the pycnocline were calculated when the stratification values were exceeding $10^{-5} s^{-2}$.

Chapter 3

Internal wave predictability over continental shelf seas. Modelled data

3.1 Abstract

In this chapter we aim to increase our understanding of internal wave (IW) dynamics over different topographies and under different dynamical forcing in a continental shelf sea using the results of a new, high-resolution (50m horizontal) configuration of the MITgcm, introduced in chapter 2. This model allows the investigation of the shelf sea IWs throughout their "lifecycle", from generation, through propagation to dissipation and uses the Fr number to quantify spacial and temporal variability in IW behaviour under a range of different stratification scenarios. Our model suggests that increasing stratification, such as that attributable to storm conditions, the IW field becomes more energetic at all frequencies. This increase in energy however, is not evenly distributed spatially or spectrally and is clearly divisible between on-shelf and off-shelf environments. Off-shelf, the spectral cascade of internal wave energy is similar to that proposed for open-ocean conditions by [Garrett and Munk, 1975]. On-shelf, the spectral distribution of energy is shown to vary under changing stratification, with a disproportionate increase of energy across frequencies higher than the dominant forcing frequency (M_2), that results in an inverse relation between stratification and spectral slope; the strongest stratification resulting in the shallowest slope. While the most

dramatic changes in IW characteristics result from the most extreme stratification scenarios these results also suggest that even slight changes in stratification and topography lead to a redistribution of IW energy, in both geographical and spectral space.

3.2 Introduction

Internal waves (IW) have been recognised as an important mixing mechanism in the ocean. In continental shelf seas, energy converted to baroclinic IWs from the barotropic tide and wind triggered inertial oscillations provide mixing at the pycnocline that is critical for redistributing nutrients, saturated gases, heat and density in the water column [Sharples et al., 2001]. Internal waves are ubiquitous throughout our oceans, the largest IWs in the world are formed in the deep ocean around dramatic topography, such as at the Hawaiian Ridges [Carter et al., 2008, Klymak et al., 2006], and the Luzon Strait [Rudnick et al., 2013] and in on-shelf areas, such as the Malin shelf [Rippeth and Inall, 2002], the Celtic shelf [Hopkins et al., 2014, Palmer et al., 2015], the Washington continental shelf [Zhang and Alford, 2015].

One of the best examples where internal waves could play an important role in shelf sea physical and biogeochemical dynamics is the Celtic Sea, where the amplitude of nonlinear internal waves have been observed to reach up to 105m and the waves can propagate up to 100km onto the shelf [Inall et al., 2011, Vlasenko et al., 2014]. These waves usually have the character of internal tides, dominated by the semi-diurnal lunar constituent M_2, generated when the barotropic tide meets the local topography.

Despite of their importance, IWs are often poorly represented in ocean models due to limited resolution or missing physics. While the latest regional scale models can produce some level of realistic generation of low frequency internal tides, higher frequencies are typically still missing in these models (for more information about model data check the chapter 2) and so the variability in IW characteristics and their contribution to ocean dynamics is not resolved. This chapter will use a high frequency, non-hydrostatic model capable of replicating a natural IW field over a broad expanse of the Celtic Sea to gain an improved understanding of how energy cascades from low frequencies to higher frequencies

under changing stratification conditions. Results will examine IWs throughout generation, propagation and dissipation to investigate how downstream behaviour might be predicted under variable stratification conditions.

In section 3.1, 3.2 the abstract and introduction are presented, providing a short overview of this chapter. In the third section (3.3) additional information about the MITgcm model is provided, for more information please refer to the chapter 2. In the fourth section (3.4) we are covering the internal wave energetics (available potential energy and horizontal kinetic energy). Later, in the section 3.5, we are moving closer to the different spectral energy slopes and their connection to the changes in topography and stratification.

By the end of this chapter we will show how the changes in stratification and topography could affect the spectral slope.

3.3 Energy assessment for internal waves in continental shelf seas

3.3.1 Slope criticality

For simplicity and to minimise numerical errors in the model, an 'idealised' profile was used in each case that provided a smooth transition from a surface mixed layer to a bottom mixed layer. While observations did suggest quite complex vertical structure at times, modal analysis (chapter 2.2.5) shows that IWs were dominated by mode 1 structure and so this was assumed to be an acceptable compromise between model performance and realistic results. Slope criticality is derived from these idealised density profiles for each of the three cases.

Figure 3.1 shows the slope criticality distribution for the three different MITgcm outputs. The majority of the shelf has slope which is subcritical, whereas on the shelf break the slope is mostly supercritical, which means that the most of internal waves should be reflected. On the shelf the generated internal waves will travel away from the shelf break, spreading its energy further onto the shelf, where the majority of the slope are subcritical which will allow them to spread even further. Although, there are a few spots near rough topographies, where

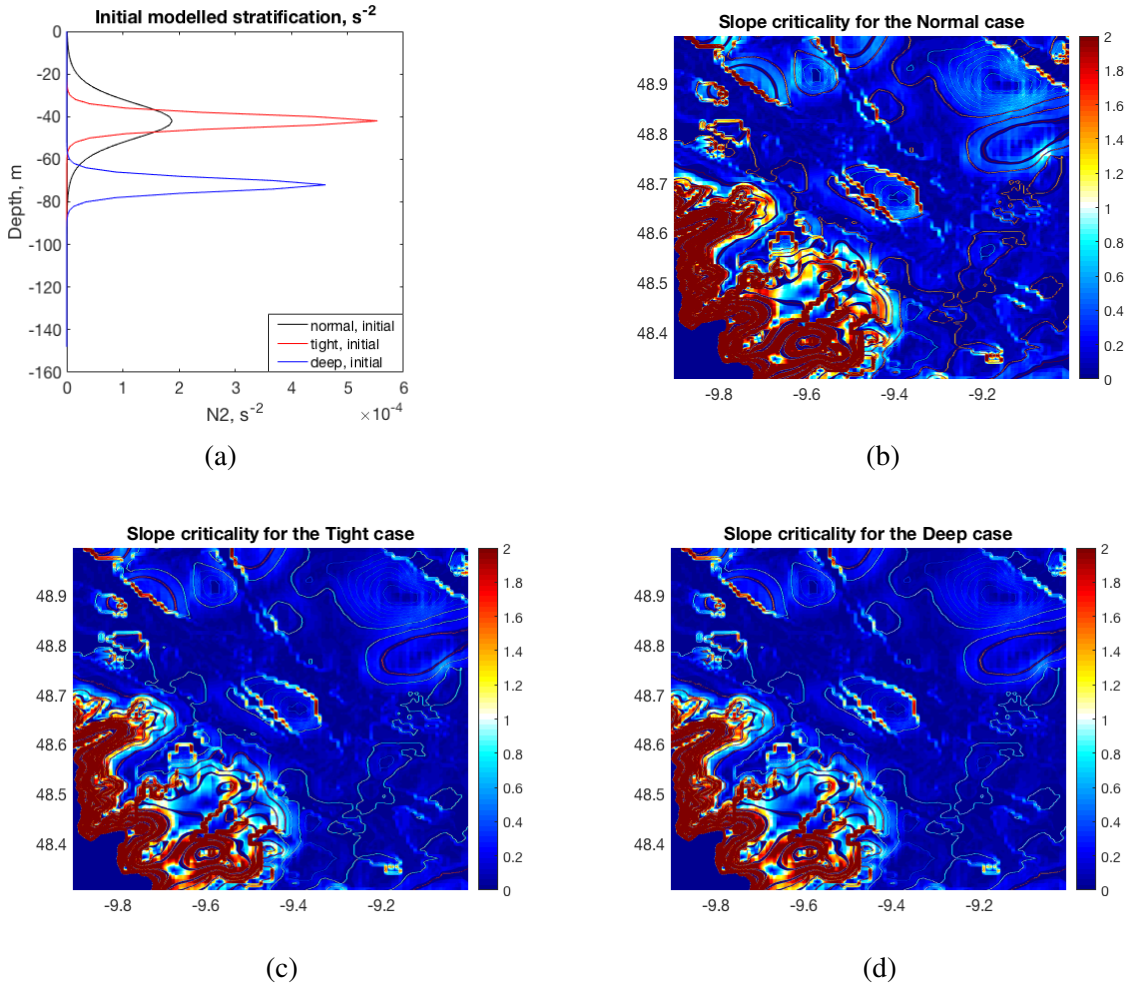

Fig. 3.1 Stratification for 3 basic scenarios from ST4 and ST5: Normal (black), Tight (red), Deep (blue). Slope criticality for the three different cases: (b) Normal, (c) Tight, (d) Deep.

$\alpha = 1$, which means that at these places internal wave may be broken down and will dissipate their energy locally. Comparing to our three cases, there are fewer places in the shelf break area with supercritical slope in the Deep case compared to the Normal and even Tight cases, this might help internal waves to propagate on shelf and bring more energy to these regions to dissipate, as less of them will be reflected by the supercritical slope.

3.3.2 Froude number

Figure 3.2 shows three different Froude number scenarios over the whole domain for the three different initial model conditions. All three cases reveal clear differences between on and

off shelf regions, which have relatively high and low Froude numbers respectively. Most of the domain is described by the Froude number of order of 1, which suggests the widespread potential for lee wave generation. There are several regions with supercritical Froude number higher than 1, typically associated with banks and other topographical features, suggesting the generation of unstable Lee waves with high possibility of breaking locally. The Deep case scenario promotes the highest values of Fr, although the distribution is similar in each case.

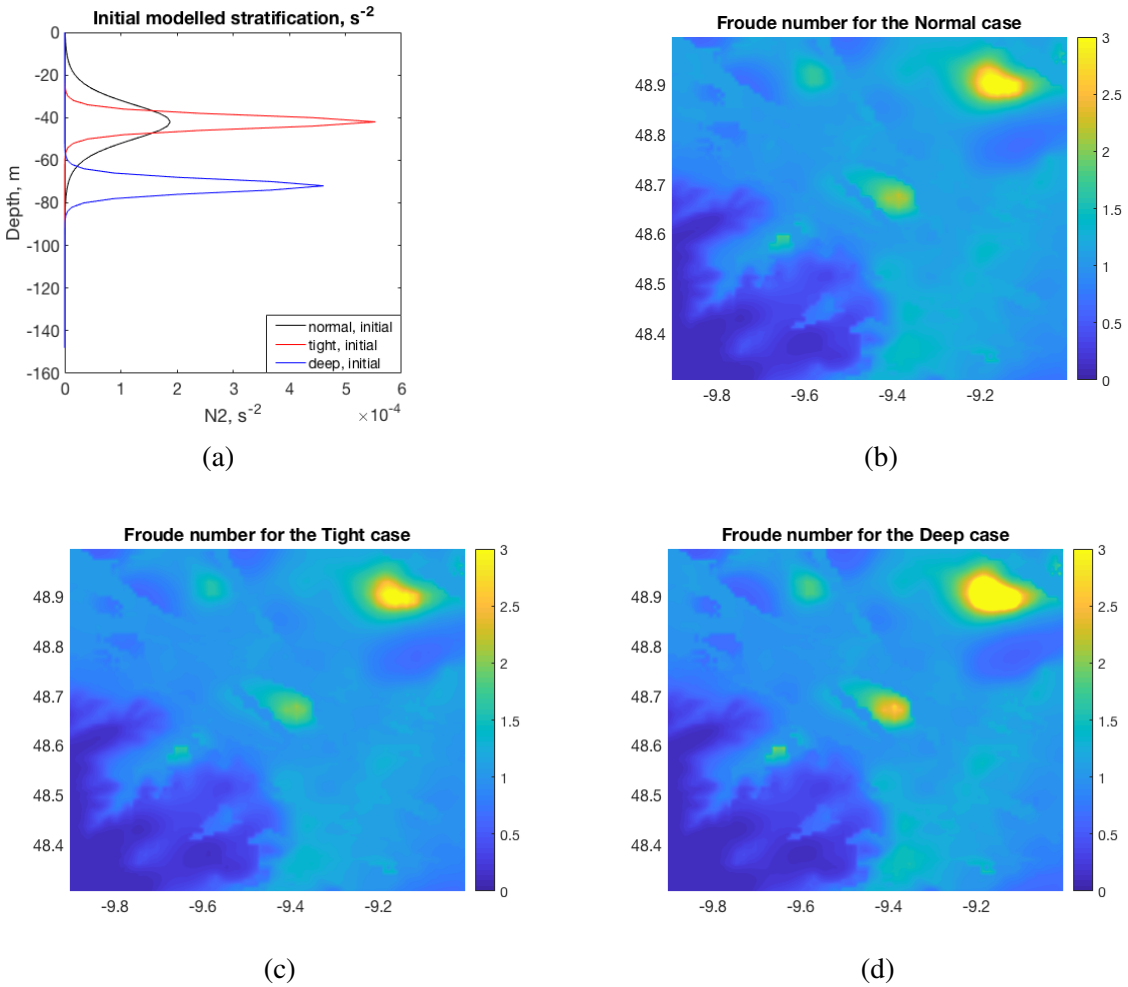

Fig. 3.2 Stratification for 3 basic scenarios from ST4 and ST5: Normal (black), Tight (red), Deep (blue). Froude number for the chosen MITgcm domain under three different stratification: (b) Normal, (c) Tight, (d) Deep. In the Deep case with deep and tight pycnocline there is a dramatic change in Froude number values over banks making them the areas of highly unstable lee wave generation.

3.3.3 Available potential energy

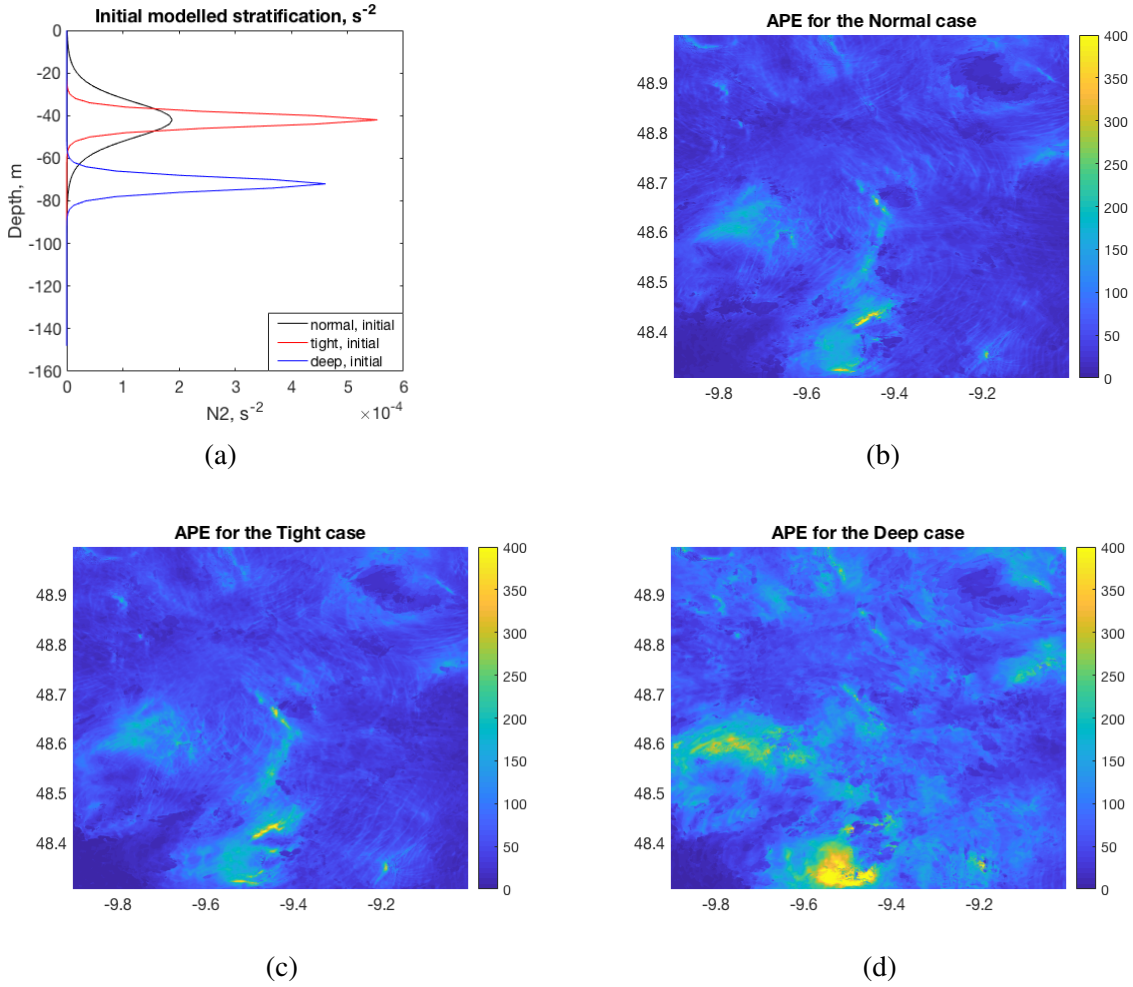

Fig. 3.3 Stratification for 3 basic scenarios from ST4 and ST5: Normal (black), Tight (red), Deep (blue). Available potential energy, $\mathrm{J\,m^{-2}}$, for the chosen MITgcm domain under three different stratification scenarios averaged through time (5 M_2 periods) and integrated through depth: (b) Normal, (c) Tight, (d) Deep. The stratification plot shows three different scenarios for MITgcm runs.

Figure 3.3 shows the results of APE calculations for the three different cases from the MITgcm model. Changes to pycnocline strength from the Normal to Tight case does provide a subtle increase in APE in the system, most notable around the larger banks. The Deep case however introduces significantly more APE across the domain, doubling the intensity from the Normal and Tight cases. It is intuitive that pycnocline depth will significantly impact on the initial displacement of IWs as they are generated and subsequently on their APE close to

the sites of generation. Figure 3.3 confirms these energy hot spots close to banks and the shelf break.

3.3.4 Horizontal kinetic energy

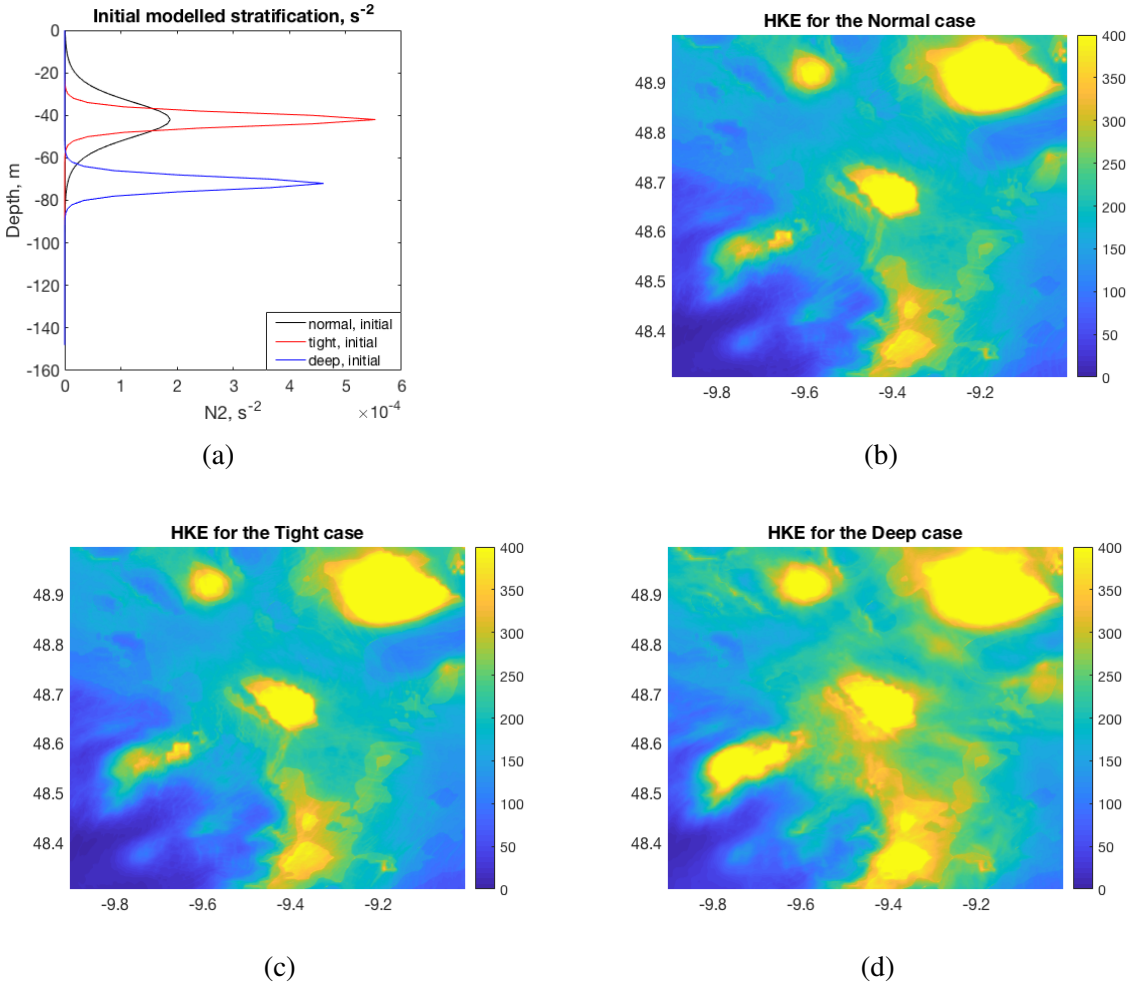

Fig. 3.4 Stratification for 3 basic scenarios from ST4 and ST5: Normal (black), Tight (red), Deep (blue). Horizontal Kinetic Energy, $\mathrm{J\,m^{-2}}$, for the chosen MITgcm domain under three different stratification averaged through time and integrated through depth: (b) Normal, (c) Tight, (d) Deep. The dramatic change in stratification leads to the increase in HKE, especially on a shelf break and areas with critical topography.

Figure 3.4 shows the results of HKE calculations for three different cases from the MITgcm model. HKE responses under the Deep case scenarios are similar to APE. There is a small, subtle increase in HKE from the Normal to Tight case, with the more dramatic

change in stratification in the Deep case producing a similarly dramatic change in HKE. In the Deep case HKE throughout the majority of the domain doubles in magnitude from the cases with shallower pycnocline. Areas over and immediately next to banks and the shelf break are all shown to be highly energetic throughout.

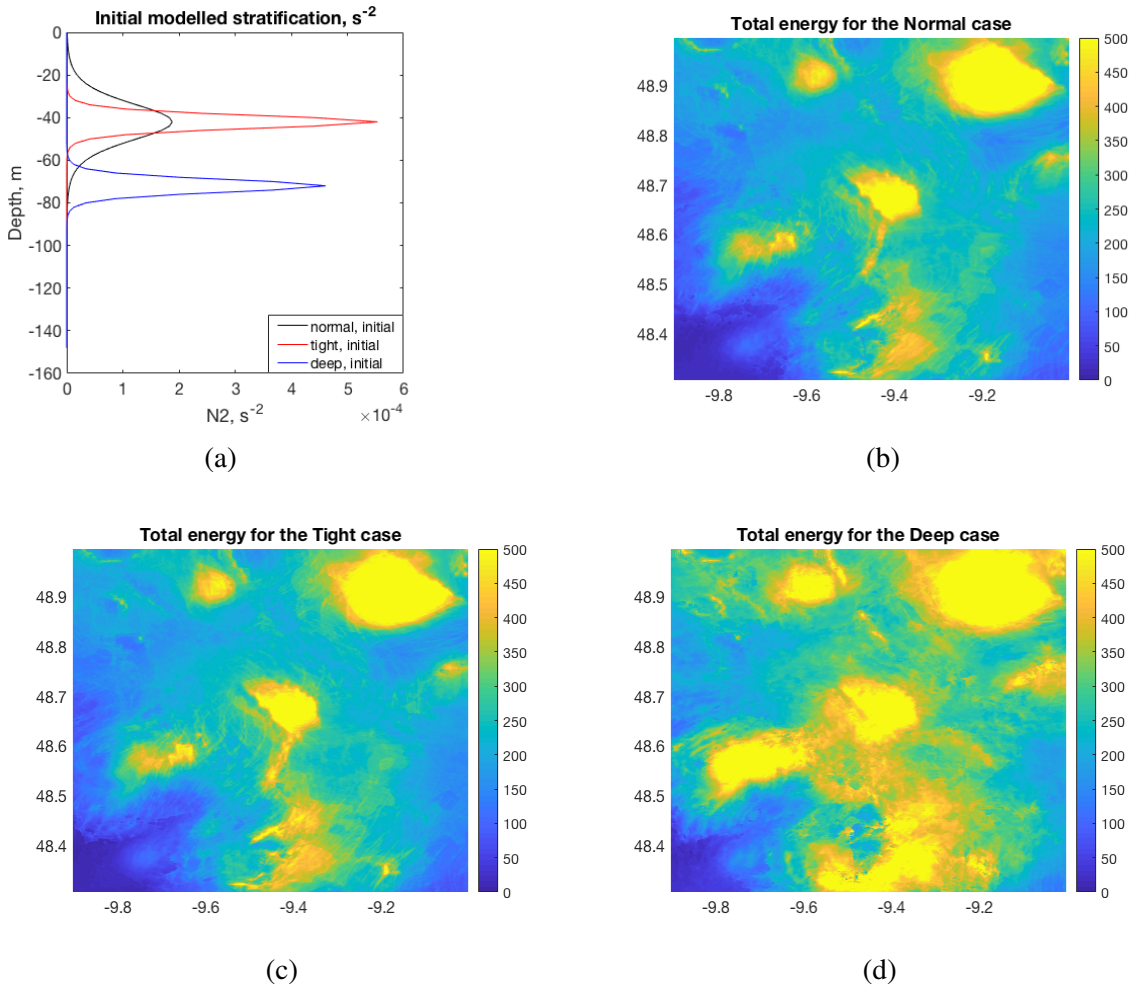

Fig. 3.5 Stratification for 3 basic scenarios from ST4 and ST5: Normal (black), Tight (red), Deep (blue). Total energy, $\mathrm{J\,m^{-2}}$, for the chosen MITgcm domain under three different stratification averaged through time and integrated through depth: (b) Normal, (c) Tight, (d) Deep. In the Deep case with deep and tight pycnocline there is a dramatic change in total energy in areas with critical topography.

3.3.5 Total IW energy (TE)

The total IW energy was calculated as a sum of HKE and APE throughout the whole domain for three different cases. Figure 3.5 shows the results of total energy calculations for three different cases from the MITgcm model. As we have seen in APE and HKE calculations, there is only a subtle increase in energy between Normal to Tight case, which maintains the same average pycnocline depth. There is however, a dramatic increase in energy in the Deep case; the deeper pycnocline case has considerably more energy within the IW field, with a clear link between energy hotspots and areas of rough topography. To summarise these results, which were presented on figures 3.3, 3.4, 3.5, internal wave hotspots are clearly identifiable and are well correlated to the distribution in Fr number space.

3.4 Predictability of IWs spectral shape in continental shelf seas from modelled data

Where processes exist that are beyond the technical capability of ocean models to simulate, a parameterisation must be used that links what can be simulated to the consequences of those unresolved processes. In the case of internal waves models will often require parameterisation of the energy content of internal waves, the spectral distribution of that energy and ultimately, the energy that they provide for mixing. One such parameterisation is the Levine normalisation of energy spectrum, which was considered in the Chapter 1 [Filonov and Novotryasov, 2005, Levine, 2002]. A number of studies show that on the shelf, IW spectra typically deviate from the standard form described by Garrett-Munk (GM75) [Garrett and Munk, 1975] as observed in the open ocean and subsequently, some have described continental shelf internal waves as unpredictable [Nash et al., 2012] . This section however, will examine whether the previously shown response in IW energy are well described by changes in stratification and whether on-shelf topography may have a predictable effect on the IW spectrum.

By the end of this section the following questions should be answered:

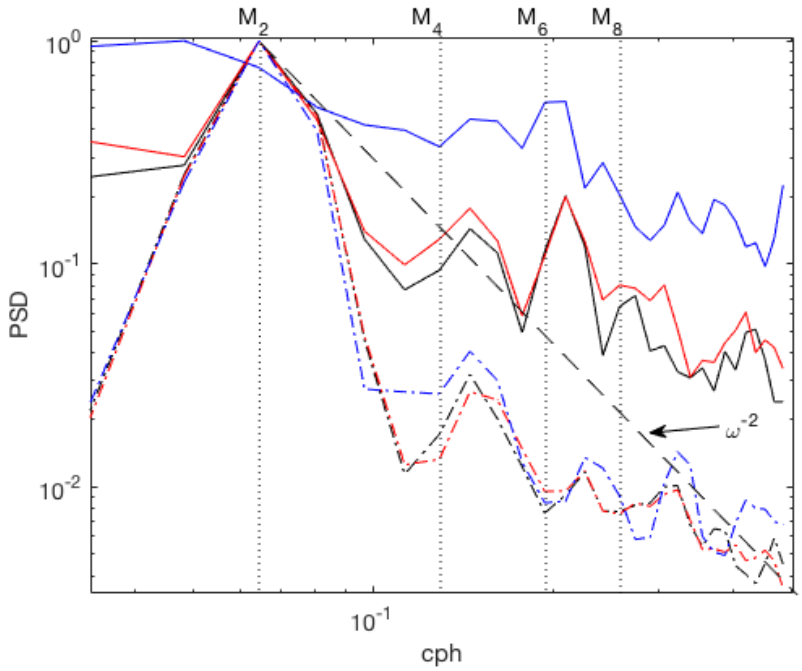

Fig. 3.6 Spectral analysis of baroclinic energy for off-shelf (dot-dash line) and on-shelf (solid line) points. Colours correspond to the cases in Fig. 3.2.

- do we have a predictable spectrum, comparable to GM75 [Garrett and Munk, 1975] open ocean energy cascade in continental shelf seas?

- if not, how does the shelf sea IW energy cascade differ from GM75 and is it predictable?

Table 3.1 Power spectrum density (PSD) slope for the three cases in on-shelf and off-shelf areas - two boxes are shown on the figure 2.1b.

Case	on-shelf	off-shelf
Normal	-1.7	-2.4
Tight	-1.6	-2.4
Deep	-1.2	-2.3

Filonov et al paper have an example of energy cascade of power -2, please check the Fig.4 in [Filonov and Novotryasov, 2005] where they are discussing ω^{-2} law in more details. Two different areas in our model domain are used to examine the dependence of the spectral slope of IW energy on different regions and stratification. Two areas are considered - off-shelf and the on-shelf region. The results are averaged in these two areas, which represents on-shelf and off-shelf areas. The highest values for slope criticality have already been identified to be

concentrated at the shelf break. As can be seen from the depth integrated spectral analysis for baroclinic energy, figure 3.6, the off-shelf energy cascade is analogous to the GM spectrum. This result supports the assumption that super-criticality in this region likely leads to a high proportion of IW energy being reflected directly back to deep ocean, where an absence of shallow water effects means IWs will behave similarly to deep ocean IWs.

In on-shelf regions the energy cascade is shown to vary under changing stratification. There is a relative increase of energy across all frequencies higher than the semi-diurnal forcing frequency. For the Normal and Tight cases spectral slope is similar. The Deep case energy spectra however are significantly shallower than the Normal and the Tight cases suggesting that as well as resulting in a general increase in energy conversion to internal waves, energy is also disproportionately increased in higher frequencies resulting in a much different slope character to open ocean IWs. These results confirm the hypothesis that the GM spectrum is not generally applicable for the shelf sea IWs. The steadily changing response in spectral shape under changing stratification however does provide further confidence that IW characteristics may yet be predictable.

An interesting result is how energy is distributed through the model domain at different frequencies. The spectral density of horizontal kinetic energy for the whole domain integrated through depth was calculated for four different frequencies - M_2, M_4, M_6 and M_8 (Figures 3.7, 3.8). As might be expected from analysis presented in section 3.4 and figure 3.6, energy increases in the Tight case are often only a few percent. Figures 3.7, 3.8 however confirm that even this slight modification to stratification, with no change in pycnocline depth does result in an increase in spectral energy with a disproportionate increase in energy at higher frequencies. The Deep case scenario in Figures 3.7, 3.8 provide another example of how the deeper pycnocline produces a dramatic increase in IW energy conversion. Interestingly, increases in spectral energy are mostly observed between topographic features (banks and slopes) rather than at the features themselves. This suggests that the increased energy observed, concentrated in the high frequency end of the spectrum, is associated with propagating waves rather than locally generated waves.

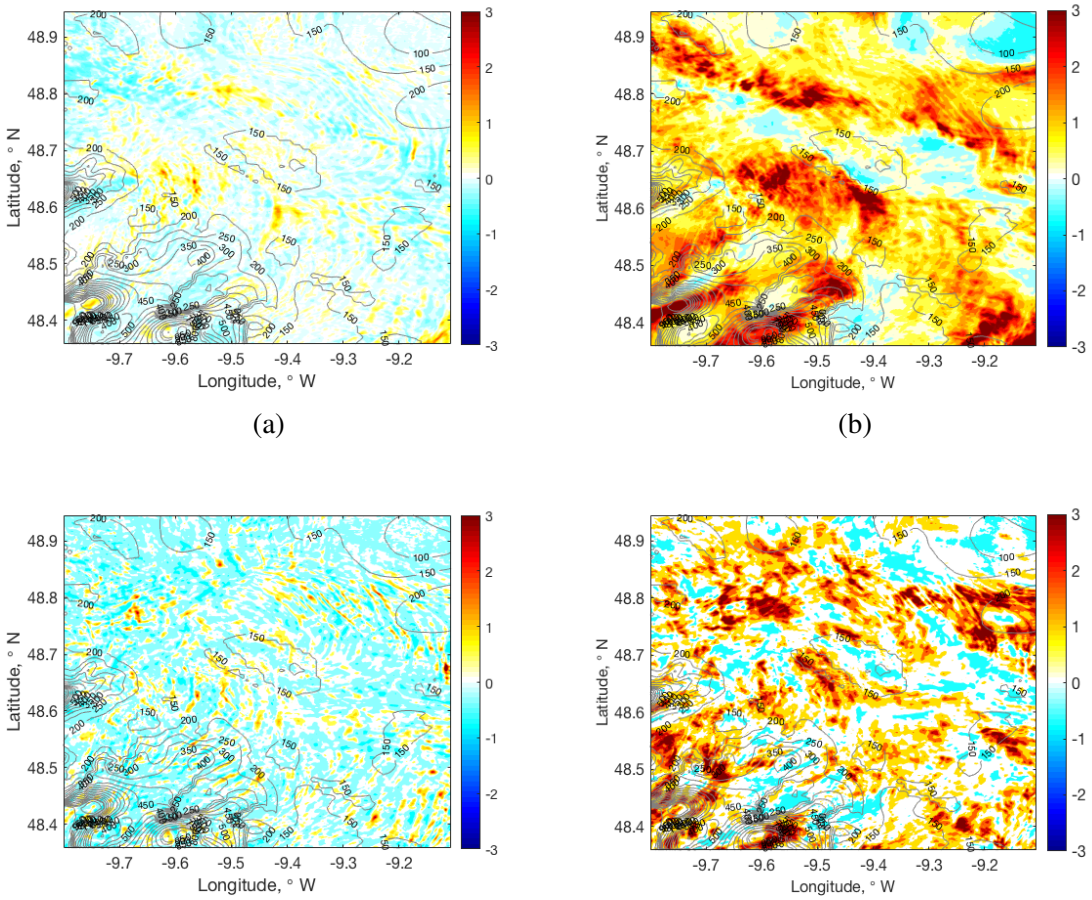

Fig. 3.7 Map of PSD differences between cases separated into different frequencies. The 1st column shows differences between the Tight and Normal cases normalised by the PSD from the Normal case to indicate the relative change in energy. The 2nd column shows normalised differences between the Deep and Normal cases. a),b) correspond to the M_2 frequency, c), d) correspond to the M_4 frequency.

In order to represent the changes in spectral slopes we have fitted a slope (via the main frequencies - M2, M4, M6, M8) to spectral density distribution in each point of the whole MITgcm domain. On Figure 3.9 you can see the result of slope fitting - the first plot is showing different examples of fitting through the transect in our model domain and on the second plot you can see two different slope, one is representing the off-shelf region and equal to $f^{-3.5}$ and another is representing the on-shelf region and equal to f^{-2}. The average spectral density slope for the whole domain for the Normal case is $f^{-2.7\pm0.5}$, for the Tight

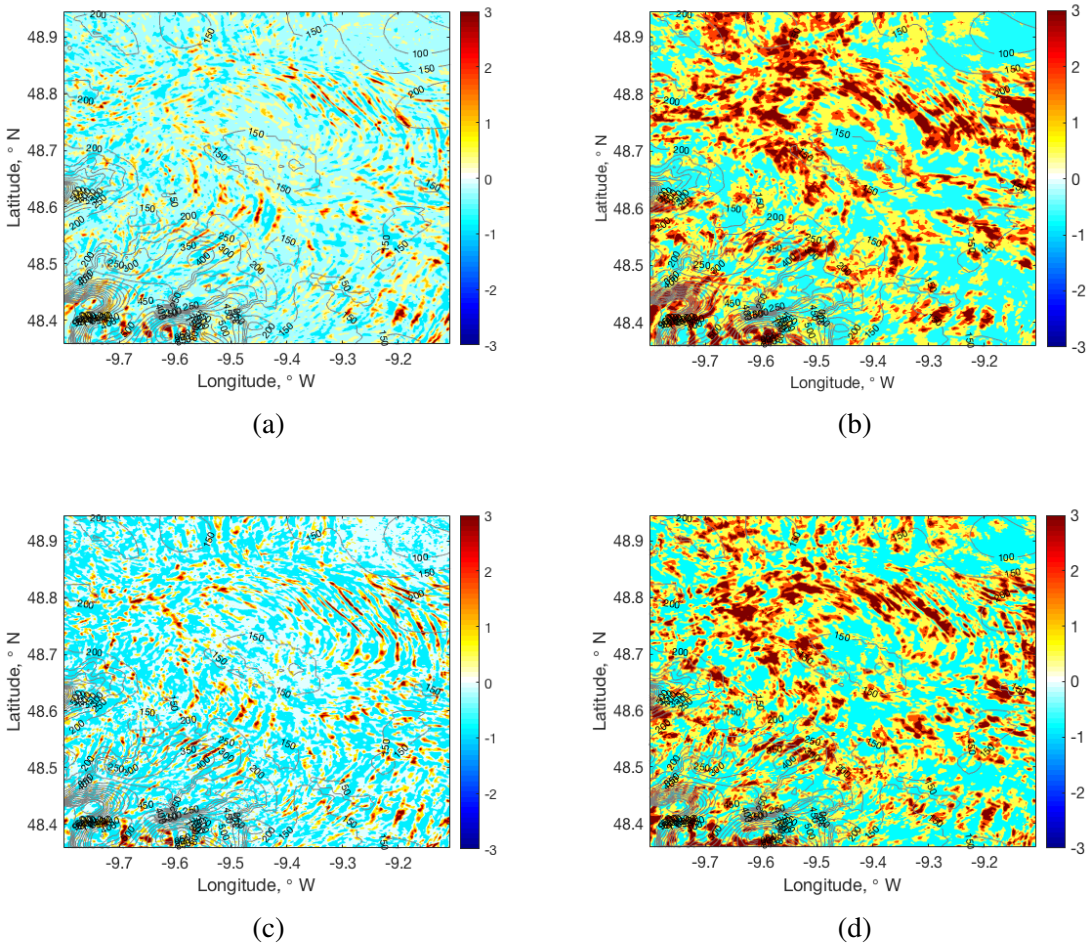

Fig. 3.8 Map of PSD differences between cases separated into different frequencies. The 1st column shows differences between the Tight and Normal cases normalised by the PSD from the Normal case to indicate the relative change in energy. The 2nd column shows normalised differences between the Deep and Normal cases. a),b) correspond to the M_6 frequency, c), d) correspond to the M_8 frequency.

case is $f^{-2.7\pm0.5}$ and for the Deep case is $f^{-2.5\pm0.5}$. This means that overall the Deep case has shallower spectral density slopes compared to the Normal and Tight cases.

The changes in PSD in the Tight case (PSD2) and the Deep case (PSD3) relative to the Normal case (PSD1) are investigated at each point in the model as (PSD2 - PSD1)/PSD1 and (PSD3-PSD1)/PSD1 respectively. Subsequent changes to the spectral density slopes are similarly calculated. Results are shown in Figure 3.10. The geographical shift in energy compared to the Normal case is clearly identifiable in the Tight case as positive/negative banding radiating away from generation hotspots (i.e. banks and the shelf break). The net

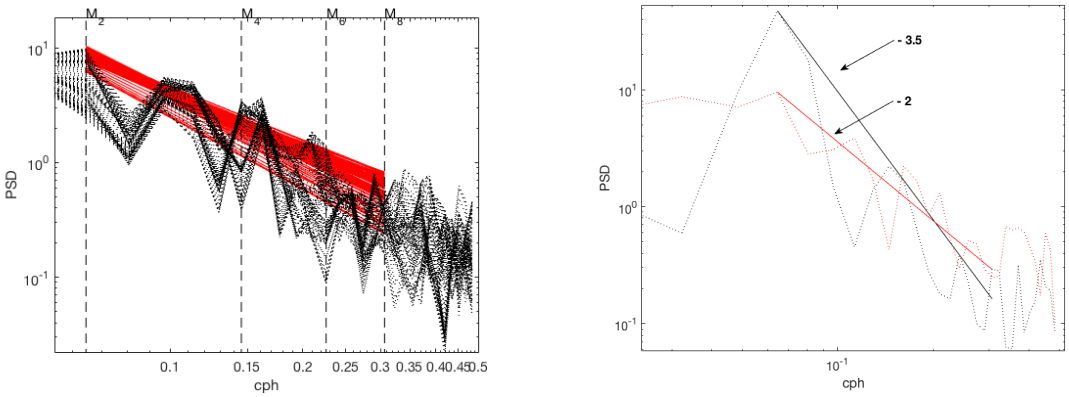

(a) (b)

Fig. 3.9 Examples of spectral slopes for power spectral densities from the MITgcm model. The left-hand plot shows some examples of fitting a log-normal line to different points in the model domain. The right-hand plot presents two distinctly different spectral slopes from the off-shelf region (black, slope $f^{-3.5}$) and on-shelf region (red, slope f^{-2})

increase in energy is around 10%, indicating that this subtle adjustment to stratification does produce an increase in the input of energy to IWs. The Deep case results however, indicate a substantial jump in total energy with only occasional instances of a reduction in energy in relatively small geographical regions. The net increase in energy is around $50-60\%$ relative to the Normal case.There are more positive values in the shelf break areas rather than in on-shelf and over bank areas, whereas for the difference between the Tight and Normal cases positive values are spread throughout whole domain. Shifts in the spectral slope clearly differ between the Tight and Deep scenarios. Shifts in the Deep case conditions cover much larger areas of the shelf, although positive/negative banding is seen in both the Tight and Deep cases, suggesting much of this adjustment to spectral distribution of energy represents a geographical shift rather than a broad scale shift in energy distribution.

To see the difference between the spectral density slopes, the histogram for the spectral slopes was calculated. The first plot of the figure 3.11 shows the histogram for the three different cases. This histogram was calculated as probability density function estimate. All of three graphs follow a normal distribution, however, the Deep case, which is represented by the blue colour, has a peak slightly to the right, which means there is higher probability to have a shallower slope of -2.5 compared to the Tight and Normal cases with higher

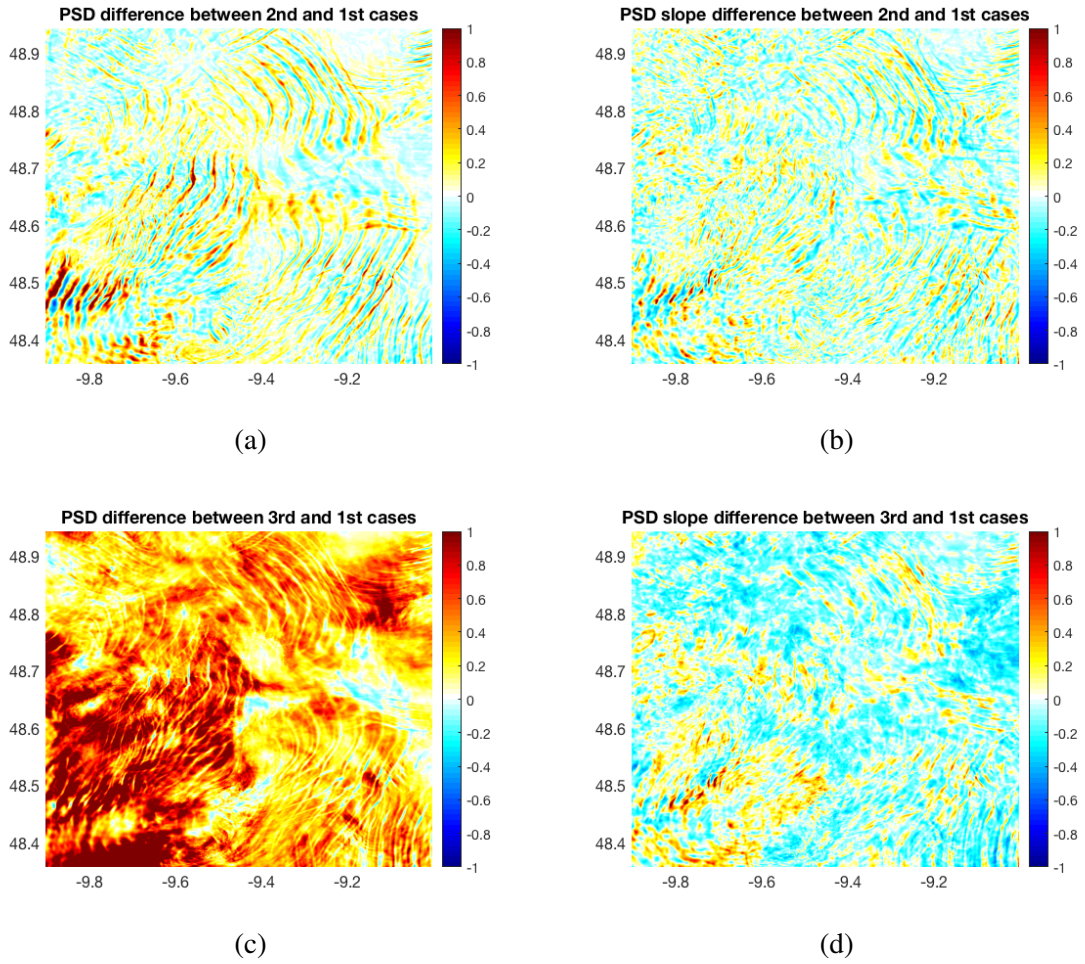

(a) (b)

(c) (d)

Fig. 3.10 PSD differences between cases normalised by the PSD1 (left-hand column) and the subsequent changes in spectral slope (right-hand column) at each point in the model. The upper plots relate to differences between the Tight and the Normal cases. The lower plots correspond to the difference between the Deep and the Normal cases.

probability slopes of -2.8 . The Deep case, however, has a higher probability to have a slope of -2 and -1.5, which is much shallower, means that more energy stays in higher frequencies. On the second plot of the same figure there are two histograms - blue colour represents the pdf estimation for the difference between the Deep and the Normal cases, red colour represents the pdf estimation for the difference between the Tight and the Normal cases, which we have seen on figure 3.10. There is higher probability to have no changes between the Tight and Normal cases, compared to the Deep and Normal cases, but there is higher probability to have shallower slopes in the Deep case.

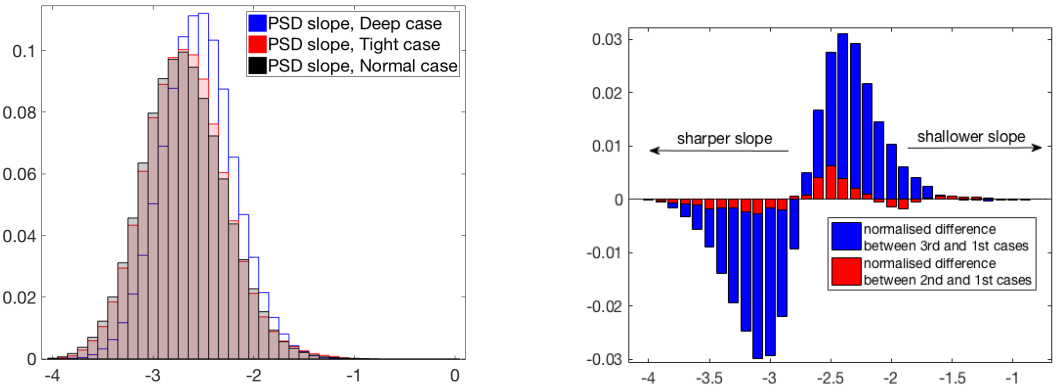

(a) (b)

Fig. 3.11 Histograms of spectral slopes for three different cases (colours correspond to the Fig. 3.1) and histograms for the differences in spectral slopes between Deep and Normal (red), and Tight and Normal (blue) cases. Black colour is for the Normal case, red colour is for the Tight case and blue colour is for the Deep case.

3.5 Summary

Our model results suggests that even subtle changes in stratification modify the IW energy levels and spectral slope. The spectral slope shapes in the MITgcm model are clearly divisible between on-shelf and off-shelf environments - off- shelf, the cascade of internal wave energy is analogous to that of the GM spectrum. On-shelf, the slope of energy cascade is shown to vary under changing stratification, with a disproportionate increase of energy across higher frequencies resulting in a flatter spectral shape. The results from our model have shown that the internal wave-field is immediately modified by varying levels of stratification and even small changes in stratification, like between the Normal and Tight cases, lead to the increase of internal energy, whereas the dramatic changes in stratification, like after storm events - the Deep case, increase internal energy disproportionally - there is much more energy in higher frequencies, compared to lower frequencies.

Chapter 4

Internal wave predictability over continental shelf sea. Observations

4.1 Abstract

In this chapter we further investigate the character of IWs in shelf sea using observational data collected from a series of campaigns in the Celtic Sea in 2012 and 2015. Results from the previous chapter are used as a framework to investigate whether changes in the energy level and spectral distribution of observed IWs replicates that found in results from a high-resolution, non-hydrostatic MITgcm model. This model suggests that under increased forcing, the IW field becomes more energetic at all frequencies. While realistic variability in tidal forcing and seasonal stratification makes direct comparison of results difficult, there is evidence of a similar reaction to the spectral cascade of IW energy. We investigate this changing spectral shape in continental shelf sea further using a unique 17-month time series of current velocity and vertical density structure and assess the predictability of internal wave energy under seasonally varying forcing.

4.2 Introduction

Model data analysis (Chapter 3) suggests that IW energy magnitude and frequency distribution varies under different stratification scenarios. Results reveal that increased stratification results not only in broad scale increases in kinetic energy in the IW field but also modifies the frequency distribution of this energy, enhancing energy transmission to higher frequency waves and resulting in a shallower spectral slope. This deviation from open ocean conditions means that commonly used scalings for energy cascades from IWs, such as those proposed by GM75 are not applicable to shelf sea environments [Levine, 2002]. Since such scalings form the basis of many open ocean mixing models [Gregg, 1989a, Henyey et al., 1986, MacKinnon and Gregg, 2003, Polzin et al., 1995]; internal wave mixing in shelf sea is often considered less predictable. Results from chapter 3 however suggest that some links do exist between the generation and propagation pathway of IWs on the shelf that make IW energy predictable from bulk parameters, such as tidal velocity magnitude and bulk stratification. Here, observational data collected from moored instrumentation is used to assess whether these model results are replicated in true ocean scenarios and whether similarly ordered behaviour might also be predictable.

While the MITgcm model data used in this study had suitably high resolution to be considered directly comparable to observations, the necessary spatial and temporal constraints on this complex model result in a number of naturally occurring processes being underrepresented or absent from model results. Far field processes, such as IWs generated at banks outside of our model domain are clearly absent. Also, the relatively short timeframe within which the chosen model configuration remains stable is too short to cover spring-neap variability. Further, the model is not coupled with the atmosphere, instead being directly forced under an initial stratification. In this chapter several observational time series are employed, each from the Celtic Sea (figure 2.1). Three time series were collected in close proximity to a bank (MS1, MS2, MS3), representing conditions moving from the bank slope to off-bank, smooth flat conditions [Palmer et al., 2013]. Three further time series were considered representative of summer stratified conditions away from dramatic topography, ST4, ST5 [Hopkins et al., 2014] and CCS [Wihsgott et al., 2019]. Collectively these 6 time

series present a range of different stratification scenarios for comparison with the range of available model results.

In section (4.3) the observational data used in this study is introduced with specific details provided regarding location and experimental setup. In section (4.4) the observed internal wave energetics are described using parameters introduced in chapters 2 and 3. Section 4.5 compares these observational results with model results presented in Chapter 3. By the end of this chapter the following questions will be covered:

- How does observed variability in shelf sea stratification impact on internal wave energy levels and frequency distribution?

- Do internal waves on shelf sea follow a repeatable redistribution of energy dependent on forcing irrespective of geographical location?

- Is there sufficient observational evidence to support the behaviour of shelf sea internal waves identified using the MITgcm model (Chapter 3)?

4.3 Energy assessment for internal waves in a continental shelf sea. Observational data

The depth integrated horizontal kinetic energy (HKE) at mooring sites ST4, ST5 and CCS are shown in Figure 4.1. The shorter time-series at ST4 and ST5 indicates background HKE levels of less than $50\,\mathrm{J\,m^{-2}}$ with occasional 2 to 5 fold increases. The largest observed HKE values relate to two storm events. The first storm event affected the ST5 site during the days 166-168, where the HKE increased to be in excess of $250\,\mathrm{J\,m^{-2}}$. A second storm event impacted both locations ST4 and ST5 during days 175-178 with similar energetic responses at both sites, reaching maximum of $150-180\,\mathrm{J\,m^{-2}}$. The first storm event produced a clear strengthening in stratification (indicated by increasing buoyancy frequency) and a deepening of the surface mixed layer depth and main pycnocline location. The second storm event has a less well-defined impact on the pycnocline with a more diffuse density structure being observed at both moorings. The first storm event was more energetic and remained in the region for over two days, whereas the second storm passed through throughout only half a day.

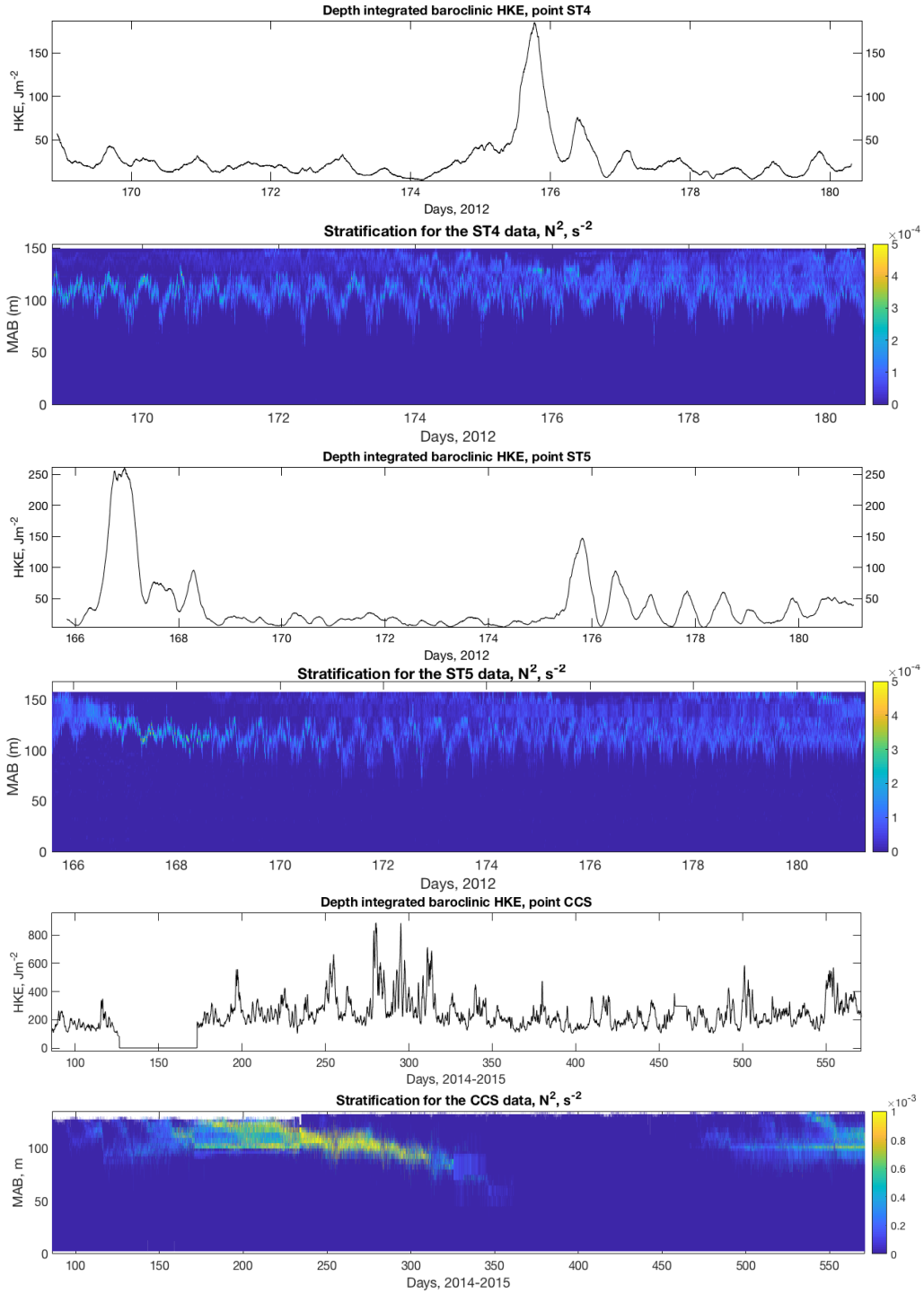

Fig. 4.1 Depth integrated moving averaged (M2) baroclinic HKE and stratification for points ST4, ST5 and CCS.

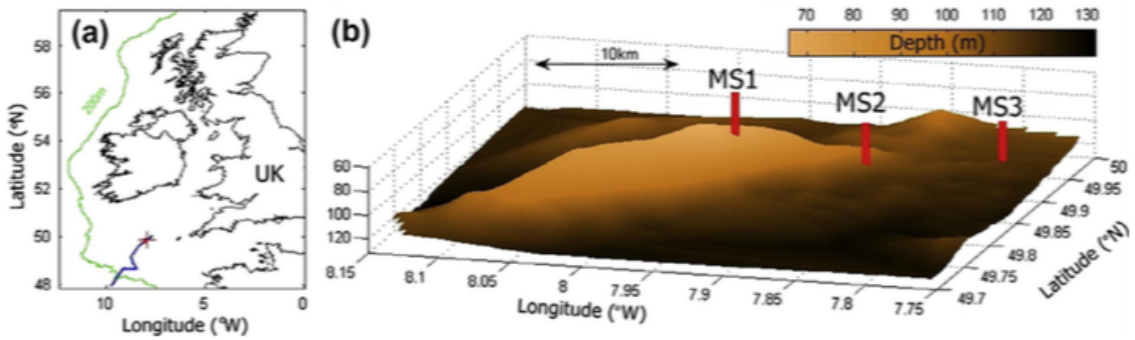

Fig. 4.2 (a) Map showing the location of Jones Bank (red cross). (b) The topography and positions of the three stations MS1, MS2 and MS3 points, from [Palmer et al., 2013].

During the second storm event a secondary pycnocline also formed in the near surface region, which will likely have interrupted direct transfer of energy to the main seasonal pycnocline. Results from the MITgcm model presented in Chapter 3 suggest that in the case of a tighter and deeper pycnocline, such as the ST5 scenario around day 166-168, that horizontal kinetic energy should increase relative to a shallow and diffused pycnocline. This suggests that the largest increase in baroclinic HKE at ST5 is likely a direct consequence of storm driven currents. The following changes in stratification however, could be linked to subsequent peaks of order $100\,\mathrm{J\,m^{-2}}$. The subsequent return to relatively low levels of baroclinic HKE however suggests that direct wind forcing was the primary factor in increasing HKE. The longer time-series of HKE for CCS over years 2014-2015 shows a clear seasonal cycle of stratification and IW forcing. Maximum values of baroclinic HKE reach $940\,\mathrm{J\,m^{-2}}$ during late summer 2014 with regular spring tide related increases in excess of $450\,\mathrm{J\,m^{-2}}$ reached around this period. This result is qualitatively in agreement with model results presented in Chapter 3 since stratification is strong but is also being forced deeper into the water column by autumnal winds. The strong deep pycnocline consistently produces the strongest forcing and baroclinic HKE, analogous to the Deep case MITgcm scenario.

Figure 4.11 shows baroclinic HKE and stratifications calculated for the Jones Bank mooring stations: MS1, MS2 and MS3. Maximum HKE values at each site are $990\,\mathrm{J\,m^{-2}}$, $705\,\mathrm{J\,m^{-2}}$, $274\,\mathrm{J\,m^{-2}}$ respectively at points MS1, MS2 and MS3.

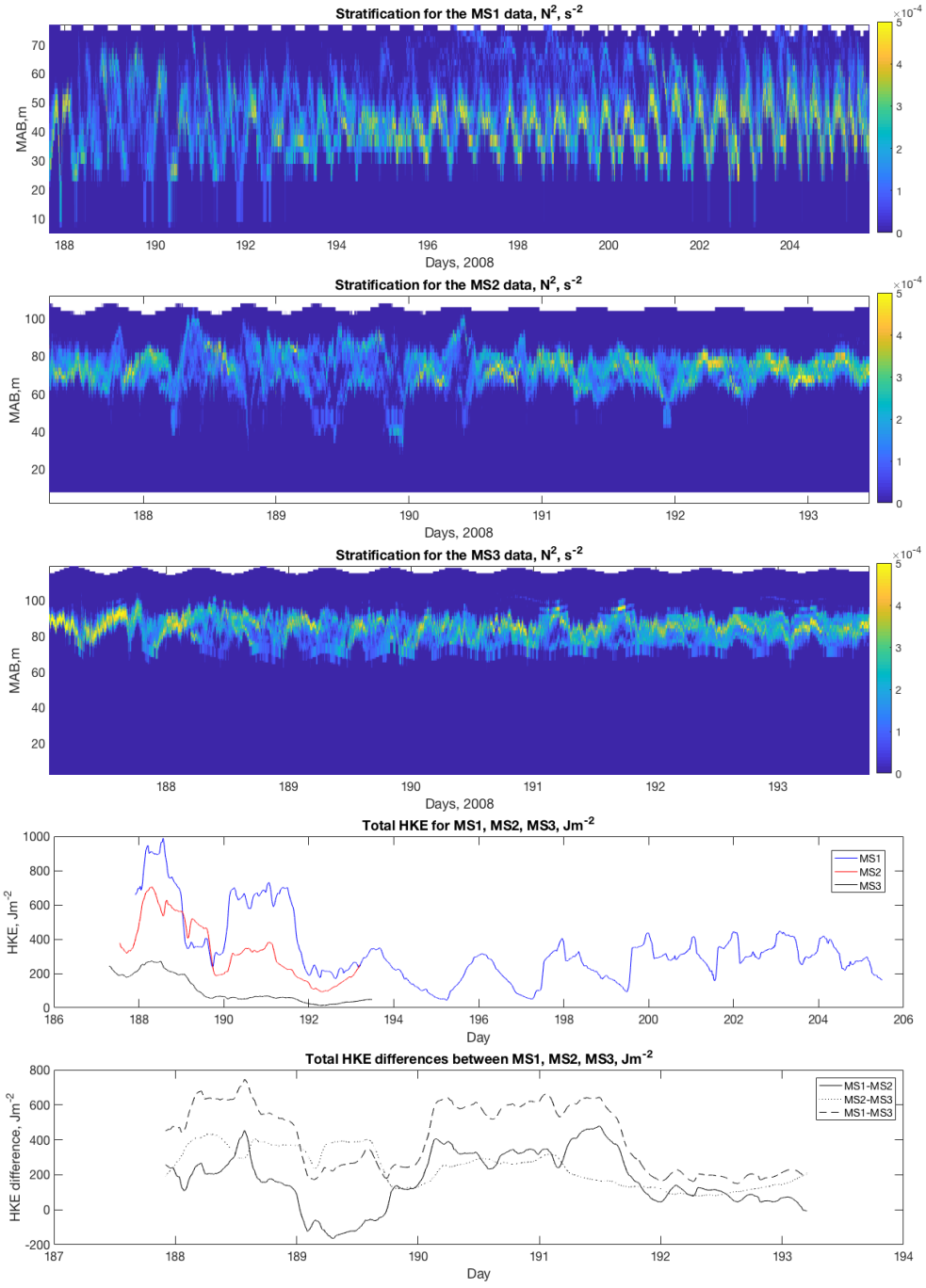

Fig. 4.3 Stratification, depth integrated moving averaged (M2) baroclinic HKE and energy loss between points MS1, MS2 and MS3.

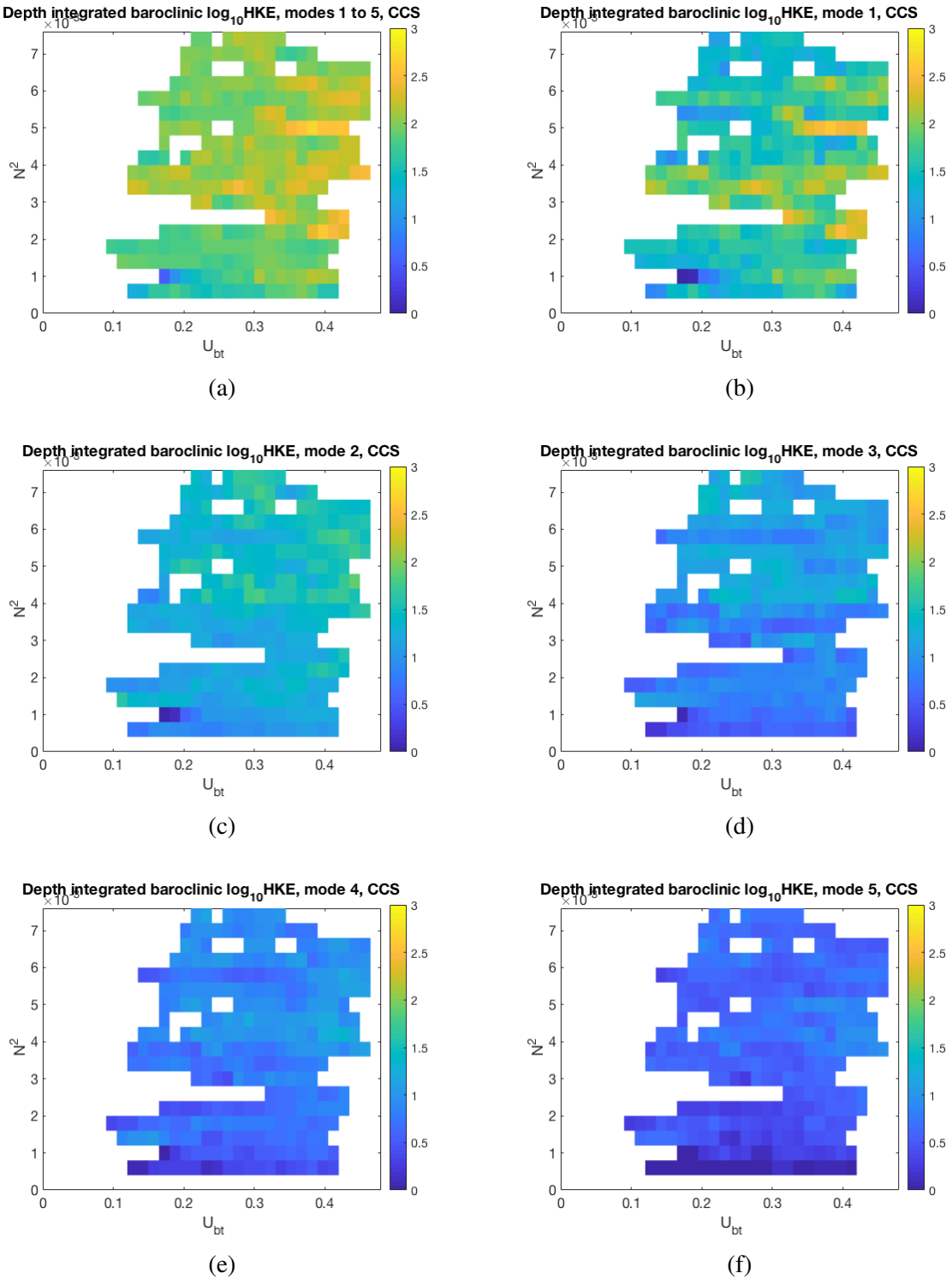

Fig. 4.4 Depth integrated moving averaged baroclinic HKE for the first 5 modes and sum of the first five modes vs U_{bt} and N^2 for CCS data.

Additionally, this figure contains the total baroclinic HKE differences between these three points. The difference between MS1 and MS3 is as high as 745 $\mathrm{J\,m^{-2}}$, the average difference is around 410 $\mathrm{J\,m^{-2}}$. The difference between MS1 and MS2 is reaching 478 $\mathrm{J\,m^{-2}}$, the average difference is around 173 $\mathrm{J\,m^{-2}}$. The difference between MS2 and MS3 is reaching 433 $\mathrm{J\,m^{-2}}$, the average difference is around 238 $\mathrm{J\,m^{-2}}$. The biggest difference in baroclinic HKE is, as expected, between points MS1 and MS3, due to the distance the internal waves travelling and dissipating energy, it is quiet intuitive. The maximum differences between MS1-MS2 and MS2-MS3 are very close to each other, probably due to the fact that there is 10 km distance between all these points, there is 45 $\mathrm{J\,m^{-2}}$ difference between them - there is a higher lost of energy between MS1-MS2, rather than between MS2-MS3. The average energy loss is the highest between points MS1-MS3, because the distance in this case is 20 km, and it is twice as high as the energy lost between MS1-MS2. The average energy loss between MS2-MS3 is higher than the average energy loss between MS1-MS2 by 65 $\mathrm{J\,m^{-2}}$.

All of these data points were used later in order to see the difference in spectral slope angles, but we will mostly focus on the CCS and MS1, MS2, MS3 data, due to their variability in time (long time-series of CCS data) and space (MS1, MS2, MS3 data).

In order to show the spread of all possible scenarios from the CCS data, the comparison between baroclinic HKE, U_{bt} and N^2 was performed. The figure 4.4 shows the dependency between logarithm of baroclinic HKE for the first 5 dynamical modes vs U_{bt}, N^2 and the dependency between the sum for the first 5 modes for the logarithm of baroclinic HKE vs U_{bt}, N^2. These plots were calculated from the CCS baroclinic velocities with omitted winter periods (between days 350-500) between 2014-2015. The first two modes are dominant for the CCS data, however, the baroclinic HKE for the 1st mode is almost twice high compared to the 2nd mode. The mean value of depth integrated moving averaged (averaged through M2 window) baroclinic HKE for whole U_{bt}, N^2 domain for the sum of the first 5 modes is 61 $\mathrm{m^2\,s^{-2}}$, the maximum value depth integrated moving averaged baroclinic HKE for the sum of the first 5 modes is 534 $\mathrm{m^2\,s^{-2}}$. The mean value of depth integrated moving averaged baroclinic HKE for whole U_{bt}, N^2 domain for 1st mode is 36 $\mathrm{m^2\,s^{-2}}$, the maximum value depth integrated moving averaged baroclinic HKE for the 1st mode is 487 $\mathrm{m^2\,s^{-2}}$. The mean

Table 4.1 Depth integrated moving averaged baroclinic HKE for the first 5 modes and sum of the first five modes vs U_{bt} and N^2 for CCS data.

mode	mean	max
1 to 5	$61\,m^2\,s^{-2}$	$534\,m^2\,s^{-2}$
1	$36\,m^2\,s^{-2}$	$487\,m^2\,s^{-2}$
2	$13\,m^2\,s^{-2}$	$119\,m^2\,s^{-2}$
3	$6\,m^2\,s^{-2}$	$57\,m^2\,s^{-2}$
4	$4\,m^2\,s^{-2}$	$32\,m^2\,s^{-2}$
5	$2\,m^2\,s^{-2}$	$19\,m^2\,s^{-2}$

value of depth integrated moving averaged baroclinic HKE for whole U_{bt}, N^2 domain for the 2nd mode is $13\,m^2\,s^{-2}$, the maximum value depth integrated moving averaged baroclinic HKE for the 2nd mode is $119\,m^2\,s^{-2}$. The mean value of depth integrated moving averaged baroclinic HKE for whole U_{bt}, N^2 domain for the 3rd mode is $6\,m^2\,s^{-2}$, the maximum value depth integrated moving averaged baroclinic HKE for the 3rd mode is $57\,m^2\,s^{-2}$. The mean value of depth integrated moving averaged baroclinic HKE for whole U_{bt}, N^2 domain for the 4th mode is $4\,m^2\,s^{-2}$, the maximum value depth integrated moving averaged baroclinic HKE for the 4th mode is $32\,m^2\,s^{-2}$. The mean value of depth integrated moving averaged baroclinic HKE for whole U_{bt}, N^2 domain for the 5th mode is $2\,m^2\,s^{-2}$, the maximum value depth integrated moving averaged baroclinic HKE for the 5th mode is $19\,m^2\,s^{-2}$. All these plots have one common feature, the baroclinic HKE values increase with U_{bt} and N^2, even the third-fifth modes have a slight increase in higher N^2 and U_{bt}. The higher baroclinic HKE values most of the time lie on N^2 values, higher than $2 \cdot 10^{-4} s^{-2}$. However, for the values lower than $2 \cdot 10^{-4} s^{-2}$, the first two modes differ approximately on a power of two, the first mode has higher baroclinic HKE for the U_{bt} higher than $0.3 ms^{-1}$. Whereas, the third and the fourth modes have smaller range throughout the whole N^2 range. Apart from the N^2 dependency, HKE depends depends on the changes in U_{bt}, though there is a slight increase of HKE values with increase in U_{bt} with higher modes.

The figure 4.5 shows the comparison of the depth integrated HKE for the point CCS between different modes, sum of the first 5 modes and the total HKE calculated from the original velocity components. The first plot shows the difference between the total HKE and

sum of the first 5 modes, the difference does not seem due to the amount of modes which were taken onto consideration, as there was a small difference between the HKE for the first 5 and first10 modes, as well this difference could not be due to the bottom mixed layer as well, as BML was eliminated from both calculations. One possibility that the dynamic vertical modes (dynmodes package in MATLAB) separate the velocity components to a numerous amounts of modes.

The figure 4.6 shows the similar comparison of the depth integrated HKE for points MS1, MS2, MS3 between different modes, sum of the first 5 modes and the total HKE calculated from the original velocity components.

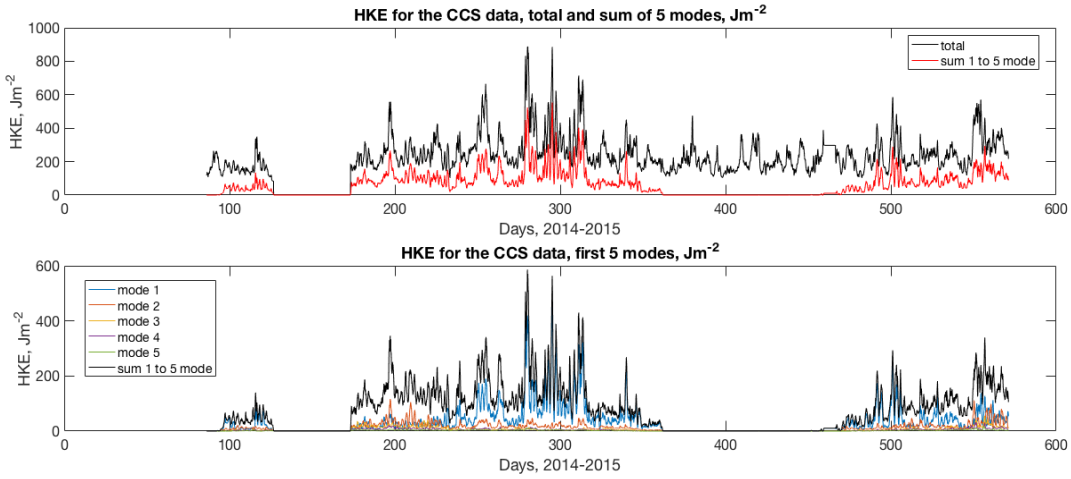

Fig. 4.5 Baroclinic depth integrated HKE for the point CCS, total, sum of the first 5 first modes separately.

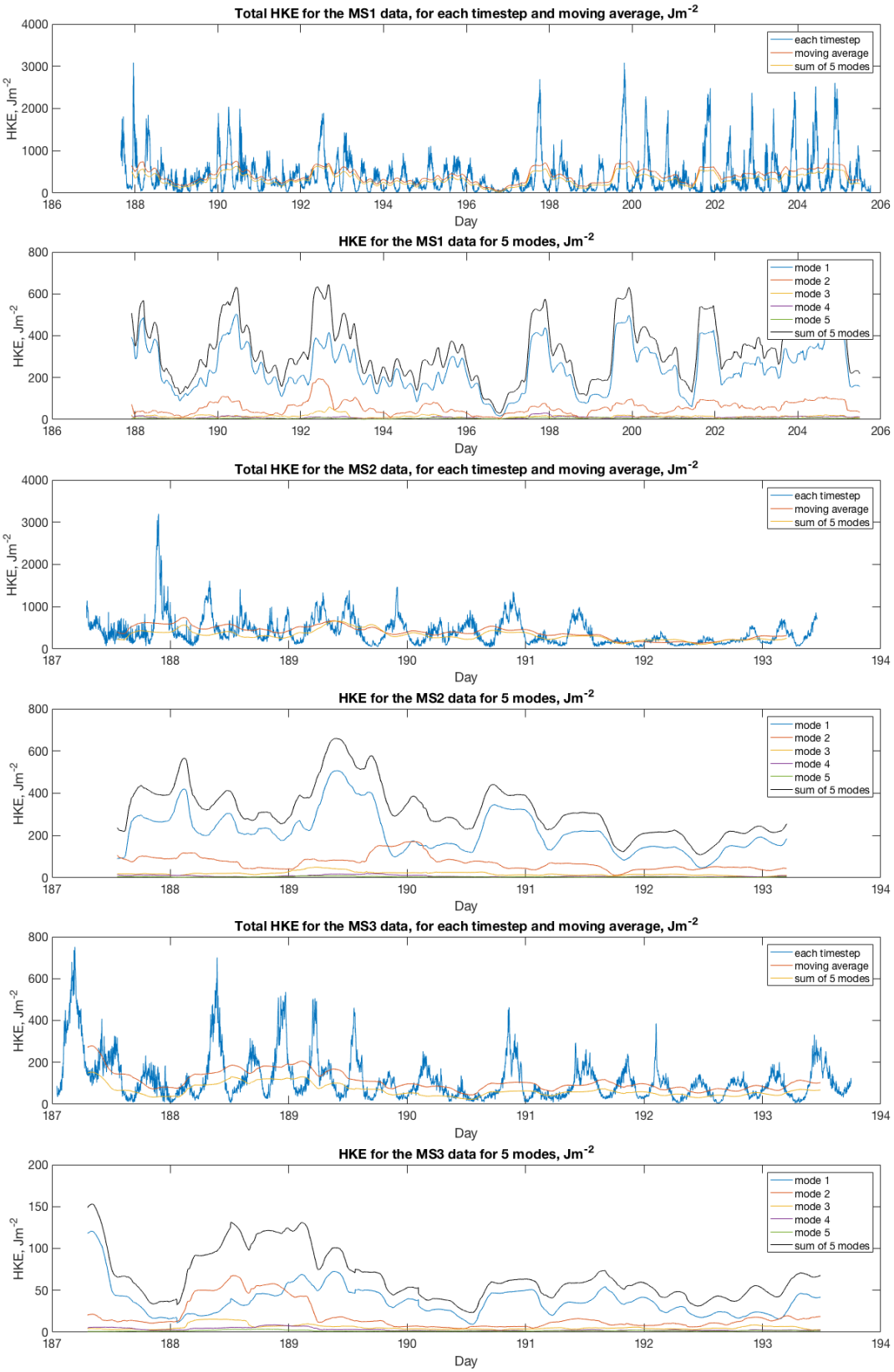

Fig. 4.6 Baroclinic depth integrated HKE for points MS1, MS2, MS3, total, sum of the first 5 first modes separately.

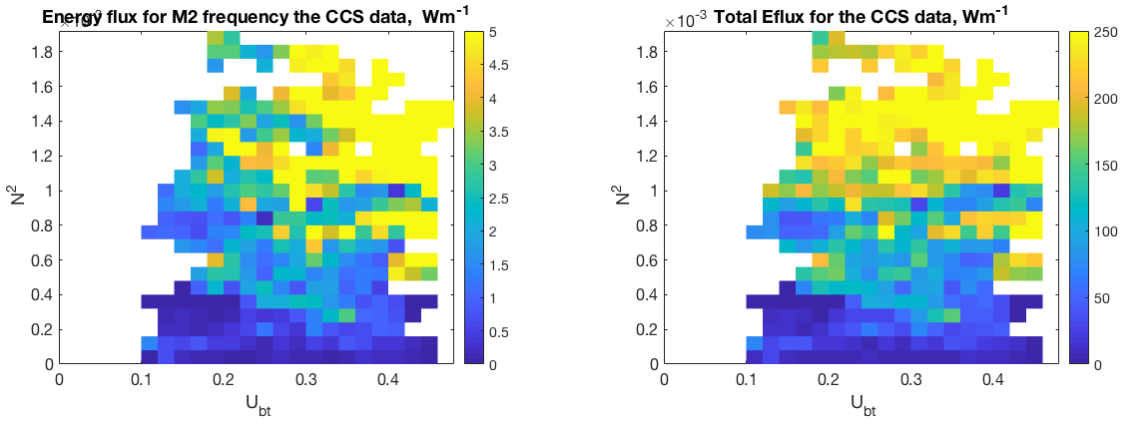

(a) (b)

Fig. 4.7 Energy flux for the CCS observational data, the left plot represents the energy flux only for the M_2 frequency, the right plot represents the total energy flux.

Similarly to the figure 4.4, the figure 4.7 shows the dependency between total energy flux and U_{bt}, N^2 and the dependency between energy flux for the M_2 frequency vs U_{bt}, N^2. These results suggests a coherent increase in total energy flux with U_{bt} and N^2. The higher total energy flux values, between 150 and 250 $\mathrm{m^2\,s^{-2}}$, most of the time lie on N^2 values, higher than $4 \cdot 10^{-4} s^{-2}$, similarly to the baroclinic HKE. However, for the values lower than $4 \cdot 10^{-4} s^{-2}$, there is a slight patch of high energy flux on the U_{bt} higher than $0.3 ms^{-1}$. The total energy flux is highly dependant on the N^2, rather on U_{bt}, though there is a slight increase of energy flux values with increase in U_{bt}, even for lower N^2.

Similarly to the CCS data, the comparison between baroclinic HKE, U_{bt} and N^2 for the MS1 data was performed. The figure 4.8 shows the dependency between logarithm of baroclinic HKE for the first 5 dynamical modes vs U_{bt}, N^2 and the dependency between the sum for the first 5 modes for the logarithm of baroclinic HKE vs U_{bt}, N^2. The mean value of depth integrated moving averaged baroclinic HKE for whole U_{bt}, N^2 domain for the sum of the first 5 modes is 331 $\mathrm{m^2\,s^{-2}}$, the maximum value depth integrated moving averaged baroclinic HKE for the sum of the first 5 modes is 645 $\mathrm{m^2\,s^{-2}}$. The mean value of depth integrated moving averaged baroclinic HKE for whole U_{bt}, N^2 domain for 1st mode is 244 $\mathrm{m^2\,s^{-2}}$, the maximum value depth integrated moving averaged baroclinic HKE for the 1st mode is 503 $\mathrm{m^2\,s^{-2}}$.

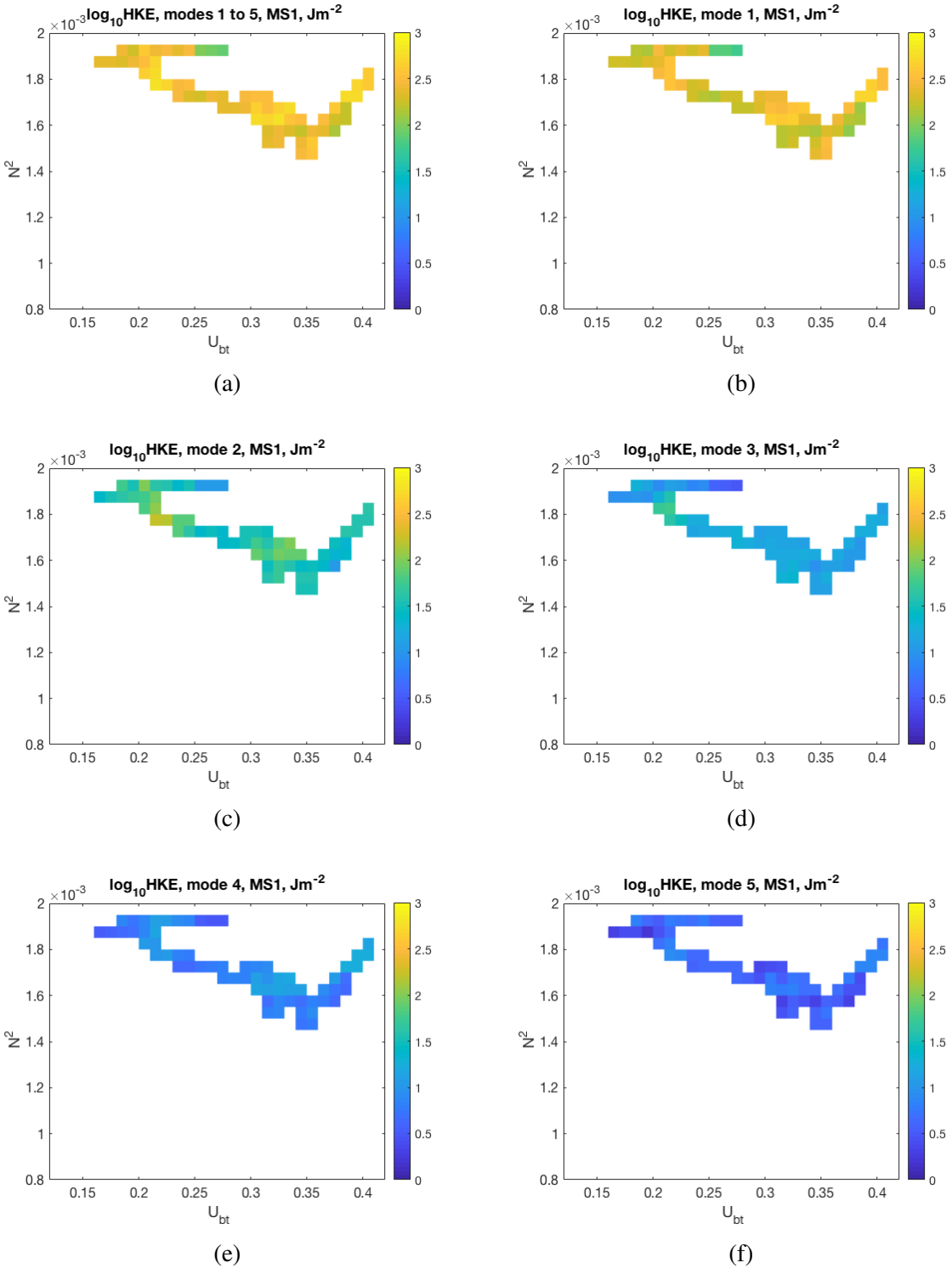

Fig. 4.8 Depth integrated moving averaged baroclinic HKE for the first 5 modes and sum of the first five modes vs U_{bt} and N^2 for MS1 data.

The mean value of depth integrated moving averaged baroclinic HKE for whole U_{bt}, N^2 domain for the 2nd mode is $57\,m^2\,s^{-2}$, the maximum value depth integrated moving averaged baroclinic HKE for the 2nd mode is $194\,m^2\,s^{-2}$. The mean value of depth integrated moving averaged baroclinic HKE for whole U_{bt}, N^2 domain for the 3rd mode is $15\,m^2\,s^{-2}$, the maximum value depth integrated moving averaged baroclinic HKE for the 3rd mode is $59\,m^2\,s^{-2}$. The mean value of depth integrated moving averaged baroclinic HKE for whole U_{bt}, N^2 domain for the 4th mode is $10\,m^2\,s^{-2}$, the maximum value depth integrated moving averaged baroclinic HKE for the 4th mode is $31\,m^2\,s^{-2}$. The mean value of depth integrated moving averaged baroclinic HKE for whole U_{bt}, N^2 domain for the 5th mode is $6\,m^2\,s^{-2}$, the maximum value depth integrated moving averaged baroclinic HKE for the 5th mode is $11\,m^2\,s^{-2}$. It is a little bit harder to see the definite behaviour, as there are only high N^2 values for the MS1 point. The figure 4.9 shows the dependency between logarithm of baroclinic HKE for the first 5 dynamical modes vs U_{bt}, N^2 and the dependency between the sum for the first 5 modes for the logarithm of baroclinic HKE vs U_{bt}, N^2 for the point MS2. The mean value of depth integrated moving averaged baroclinic HKE for whole U_{bt}, N^2 domain for the sum of the first 5 modes is $322\,m^2\,s^{-2}$, the maximum value depth integrated moving averaged baroclinic HKE for the sum of the first 5 modes is $660\,m^2\,s^{-2}$. The mean value of depth integrated moving averaged baroclinic HKE for whole U_{bt}, N^2 domain for 1st mode is $218\,m^2\,s^{-2}$, the maximum value depth integrated moving averaged baroclinic HKE for the 1st mode is $508\,m^2\,s^{-2}$. The mean value of depth integrated moving averaged baroclinic HKE for whole U_{bt}, N^2 domain for the 2nd mode is $72\,m^2\,s^{-2}$, the maximum value depth integrated moving averaged baroclinic HKE for the 2nd mode is $172\,m^2\,s^{-2}$. The mean value of depth integrated moving averaged baroclinic HKE for whole U_{bt}, N^2 domain for the 3rd mode is $20\,m^2\,s^{-2}$, the maximum value depth integrated moving averaged baroclinic HKE for the 3rd mode is $51\,m^2\,s^{-2}$. The mean value of depth integrated moving averaged baroclinic HKE for whole U_{bt}, N^2 domain for the 4th mode is $8\,m^2\,s^{-2}$, the maximum value depth integrated moving averaged baroclinic HKE for the 4th mode is $21\,m^2\,s^{-2}$.

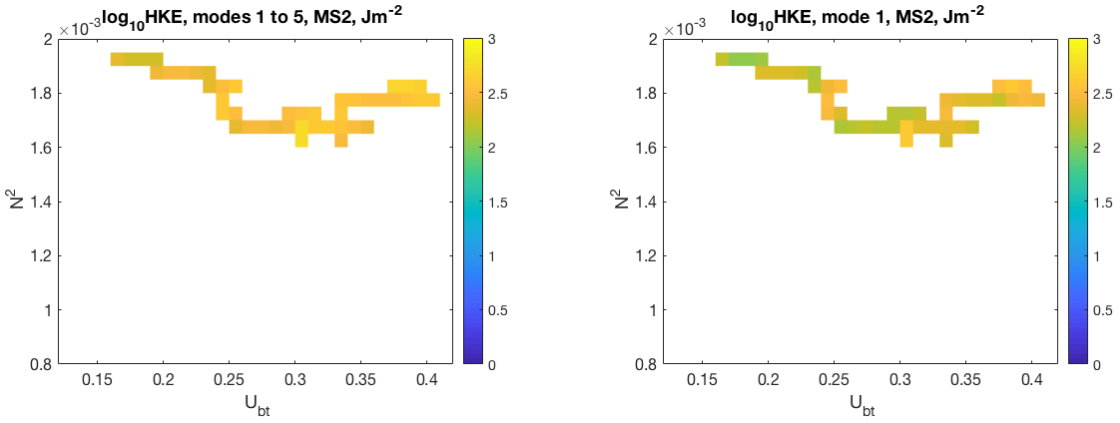

(a)

(b)

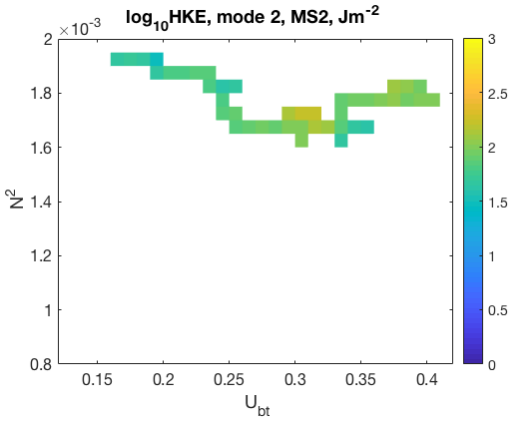

(c)

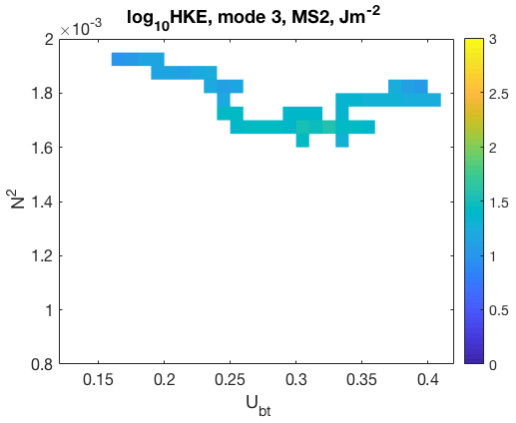

(d)

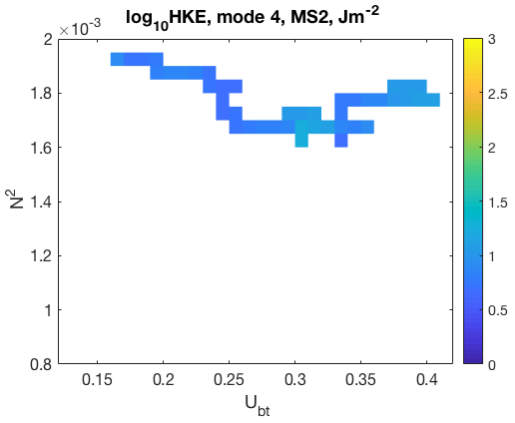

(e)

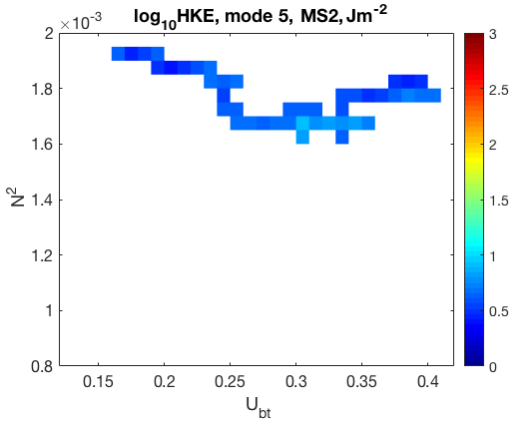

(f)

Fig. 4.9 Depth integrated moving averaged baroclinic HKE for the first 5 modes and sum of the first five modes vs U_{bt} and N^2 for MS2 data.

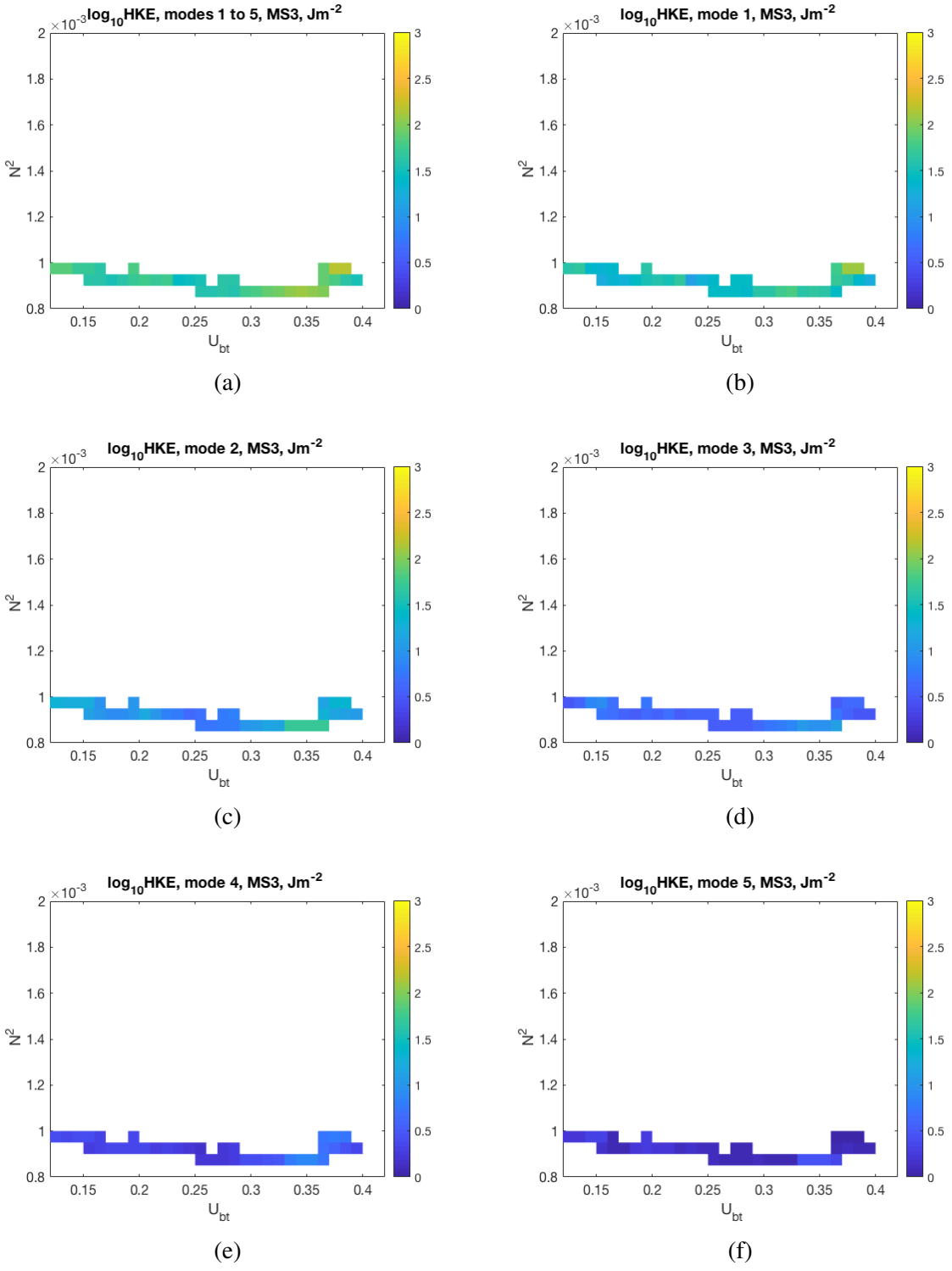

Fig. 4.10 Depth integrated moving averaged baroclinic HKE for the first 5 modes and sum of the first five modes vs U_{bt} and N^2 for MS3 data.

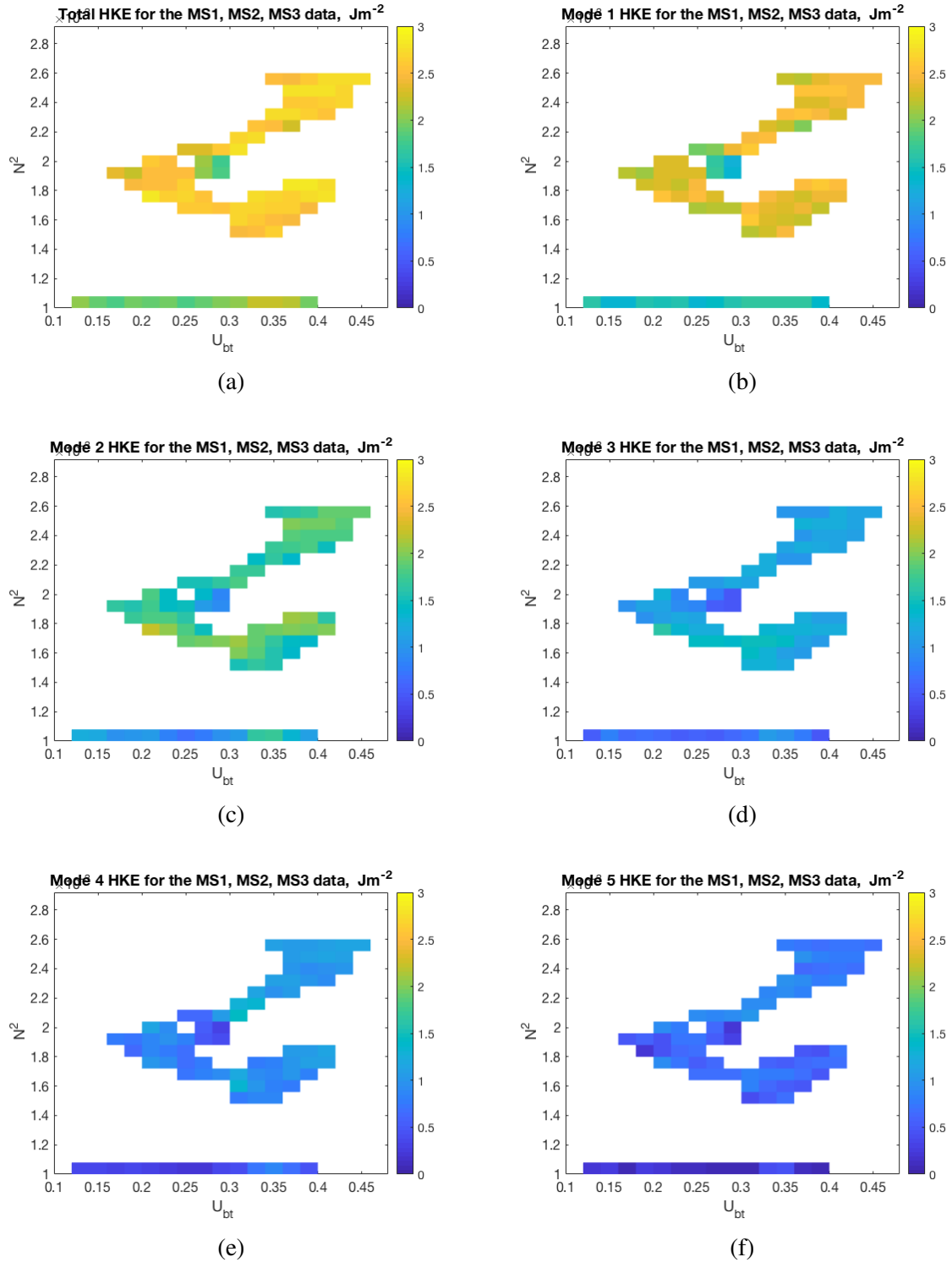

Fig. 4.11 Depth integrated moving averaged baroclinic HKE for the first 5 modes and sum of the first five modes vs U_{bt} and N^2 for combined MS1, MS2, MS3 data.

The mean value of depth integrated moving averaged baroclinic HKE for whole U_{bt}, N^2 domain for the 5th mode is $5\,m^2\,s^{-2}$, the maximum value depth integrated moving averaged baroclinic HKE for the 5th mode is $10\,m^2\,s^{-2}$.

The figure 4.10 shows the dependency between logarithm of baroclinic HKE for the first 5 dynamical modes vs U_{bt}, N^2 and the dependency between the sum for the first 5 modes for the logarithm of baroclinic HKE vs U_{bt}, N^2 for the point MS3. The mean value of depth integrated moving averaged baroclinic HKE for whole U_{bt}, N^2 domain for the sum of the first 5 modes is $66\,m^2\,s^{-2}$, the maximum value depth integrated moving averaged baroclinic HKE for the sum of the first 5 modes is $153\,m^2\,s^{-2}$. The mean value of depth integrated moving averaged baroclinic HKE for whole U_{bt}, N^2 domain for 1st mode is $37\,m^2\,s^{-2}$, the maximum value depth integrated moving averaged baroclinic HKE for the 1st mode is $121\,m^2\,s^{-2}$. The mean value of depth integrated moving averaged baroclinic HKE for whole U_{bt}, N^2 domain for the 2nd mode is $18\,m^2\,s^{-2}$, the maximum value depth integrated moving averaged baroclinic HKE for the 2nd mode is $68\,m^2\,s^{-2}$. The mean value of depth integrated moving averaged baroclinic HKE for whole U_{bt}, N^2 domain for the 3rd mode is $6\,m^2\,s^{-2}$, the maximum value depth integrated moving averaged baroclinic HKE for the 3rd mode is $16\,m^2\,s^{-2}$. The mean value of depth integrated moving averaged baroclinic HKE for whole U_{bt}, N^2 domain for the 4th mode is $3\,m^2\,s^{-2}$, the maximum value depth integrated moving averaged baroclinic HKE for the 4th mode is $9\,m^2\,s^{-2}$. The mean value of depth integrated moving averaged baroclinic HKE for whole U_{bt}, N^2 domain for the 5th mode is $2\,m^2\,s^{-2}$, the maximum value depth integrated moving averaged baroclinic HKE for the 5th mode is $4\,m^2\,s^{-2}$. Comparing all these points, MS1, MS2, MS3, we can see the definite behaviour of baroclinic HKE which is mostly increasing with stratification and less with increase in barotropic velocities.

The figure 4.11 shows the dependency between logarithm of baroclinic HKE for the first 5 dynamical modes vs U_{bt}, N^2 and the dependency between the sum for the first 5 modes for the logarithm of baroclinic HKE vs U_{bt}, N^2 for combined data for points MS1, MS2 and MS3. The main aim of this figure is to show that dominant modes hold more energy in each point and that energy is lost rapidly with distance from the site of generation (MS1 to MS3).

Table 4.2 Mean depth integrated moving averaged baroclinic HKE for the first 5 modes and sum of the first five modes vs U_{bt} and N^2 for combined MS1, MS2, MS3 data (over common period between all these three moorings).

mode	MS1	MS2	MS3
1 to 5	$331\,m^2\,s^{-2}$	$322\,m^2\,s^{-2}$	$66\,m^2\,s^{-2}$
1	$244\,m^2\,s^{-2}$	$218\,m^2\,s^{-2}$	$37\,m^2\,s^{-2}$
2	$57\,m^2\,s^{-2}$	$72\,m^2\,s^{-2}$	$18\,m^2\,s^{-2}$
3	$15\,m^2\,s^{-2}$	$20\,m^2\,s^{-2}$	$6\,m^2\,s^{-2}$
4	$10\,m^2\,s^{-2}$	$8\,m^2\,s^{-2}$	$3\,m^2\,s^{-2}$
5	$6\,m^2\,s^{-2}$	$5\,m^2\,s^{-2}$	$2\,m^2\,s^{-2}$

Table 4.3 Maximum depth integrated moving averaged baroclinic HKE for the first 5 modes and sum of the first five modes vs U_{bt} and N^2 for combined MS1, MS2, MS3 data (over common period between all these three moorings).

mode	MS1	MS2	MS3
1 to 5	$645\,m^2\,s^{-2}$	$660\,m^2\,s^{-2}$	$153\,m^2\,s^{-2}$
1	$503\,m^2\,s^{-2}$	$508\,m^2\,s^{-2}$	$121\,m^2\,s^{-2}$
2	$194\,m^2\,s^{-2}$	$172\,m^2\,s^{-2}$	$68\,m^2\,s^{-2}$
3	$59\,m^2\,s^{-2}$	$51\,m^2\,s^{-2}$	$16\,m^2\,s^{-2}$
4	$31\,m^2\,s^{-2}$	$21\,m^2\,s^{-2}$	$9\,m^2\,s^{-2}$
5	$11\,m^2\,s^{-2}$	$10\,m^2\,s^{-2}$	$4\,m^2\,s^{-2}$

By combining the data from all three points - MS1, MS2 and MS3, it becomes clear that there is a loss of HKE from the site of generation MS1 to the point MS3. To be precise, the mean loss of depth integrated moving averaged baroclinic HKE for the sum of the first 5 modes between points MS1 and MS3 is 80 %, whereas the mean loss of depth integrated moving averaged baroclinic HKE for the sum of the first 5 modes between points MS1 and MS2 is only 2.7 %, so a loss of more than 50 %, as indicated from HKE between MS1 and MS3, is attributable to local dissipation near the bank with the remainder propagating and losing energy further down the generation cite.

4.4 Spectral energy slopes in observational data

While realistic variability in tidal forcing and seasonal stratification makes direct comparison of results difficult, there is evidence of a similar reaction to the spectral cascade of IW energy in observations.

The figure 4.12 shows the spectral analysis of baroclinic velocities for the Normal and Deep cases at the points CCS, MS1, MS2, MS3, where the blue lines represents the Deep case and black lines represents the Normal case. As can be seen, MS2 and MS3 do not have big differences between these two cases (days 188-190 for the Deep case and 191-193 for the Normal case), whereas the MS1 and CCS have a significant difference in the spectral slope angle, which could mean that there is more energy stays in higher frequencies in case of tighter and deeper pycnocline - the same result we have observed in our MITgcm model.

There are not a lot of critical topographical features around CCS point, this is the reason why the spectrum shape looks quite smooth without many peaks in the high frequencies. This mooring is a bit different to other morings, where we have the highest energy in inertial frequencies, not in tidal frequency. In this case it is possible to use GM and L02 spectral shapes and L02 (Levine 2002) will work even better, than GM, as its spectral shape is very steep at the beginning till M6 frequency and after it becomes shallow, which means that in the CCS mooring we have more energy in high frequencies compared to other observational points. The blue line represents the cases closer to the Deep case that we analysed in the

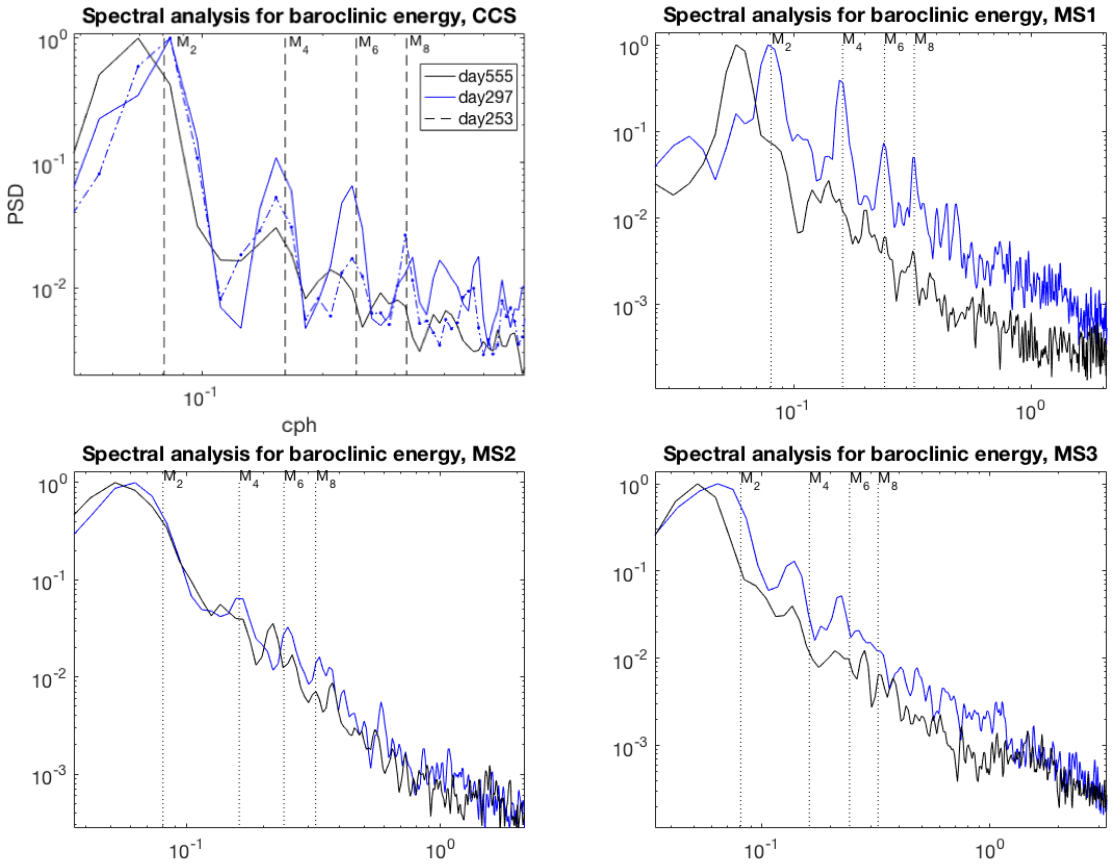

Fig. 4.12 Spectral analysis of baroclinic energy for the CCS, MS1, MS2 and MS3. Solid and dashed blue lines represent the Deep case, here the slope is shallower compared to the solid black line (Normal case). These results confirm the effect of deeper and stronger stratification on shape of spectral slopes found in the MITgcm results.

MITgcm model, the black line represents the Normal case that we have considered in the MITgcm model. These results agree with our model results where we had a shallower slope for the case with deep and tight pycnocline.

4.5 Summary

Our model results suggests that even subtle changes in stratification scenarios modify the IW energy levels and spectral slope. The observational data confirmed that there is a change in HKE and spectral slope depend on the initial stratification scenarios. We investigated this changing spectral shape and HKE in continental shelf sea using numerous moorings, as well as a unique 17-month time series of current velocity and vertical density structure. The observational data show the similar order of dependence between the stratification scenarios and baroclinic horizontal kinetic energy (HKE), as well as with spectral slopes. It was difficult to directly distinguish the three different model cases in the observational data, owing to an inconsistency in the occurrence of cases with only a small amount of Deep case scenarios being observed, all of which were during the autumn. Similar conditions to the Normal and Tight cases were observed throughout summer and spring stratified periods. While the amount of Deep case occurrences is not high, it is observed that this case did produce a significant increase in HKE during autumn months. HKE increases two-fold during these autumnal periods. This is an important result as it suggests that while the increase in wind energy acts to break down summer stratification, the relocation of the pycnocline deeper in the water column acts to increase baroclinic energy within the system.

Chapter 5

The contribution of internal waves to continental shelf seas turbulence and mixing

5.1 Abstract

In this chapter we aim to increase our understanding of connections between internal wave (IW) dynamics and turbulent mixing over different topographies and under different dynamical forcing in continental shelf seas. I use the results of the high-resolution (50m horizontal) MITgcm configuration and the results from the observational and ocean microstructure glider data. The $Ri_{g\%}$ is the number of times of gradient Richardson number lower than 1, which shows a clear dependency on stratification scenarios for the three modelled cases, with the highest numbers of order of 70% in the Deep case, which suggests that there is a higher chance of turbulent mixing in case of deep and tight pycnocline. The $Ri_{g\%}$ from observational data has a similar spread between three modelled cases.

5.2 Introduction

Turbulence plays a key role in mixing and dynamics of the shelf seas by transferring heat, mass and momentum [Simpson and Sharples, 2012]. As been discussed in the chapter 1, only $25-30\%$ of tidal energy dissipates in the deep ocean, the rest is dissipated in the shelf seas [Egbert and Ray, 2000]. Turbulence is much more variable in shelf seas, compared to the open-ocean scenario, due to variable topography, internal solitary waves and internal tides, which makes it difficult to predict and parameterise in numerical models. Currently researchers are trying to find different processes, that affect internal mixing in order to parameterise tidal dissipation [MacKinnon and Gregg, 2003, Nash and Moum, 2001, Simpson et al., 1996].

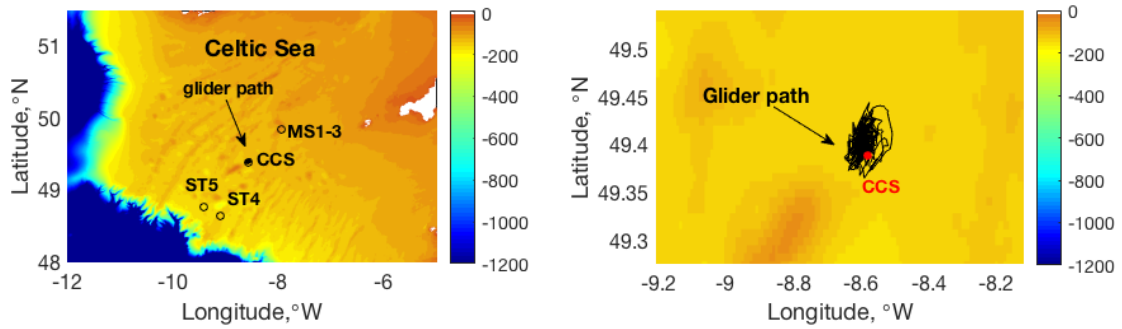

(a) (b)

Fig. 5.1 (a) Celtic sea map with points ST4, ST5, CCS, MS1, MS2, MS3 showing the mooring positions and the glider path location. (b) Map of the glider path and CCS location. Colours represent the depth in metres.

In this chapter we discuss the effect of different topographies and varying stratification on turbulent mixing in a continental shelf sea, we also identify the predictability of mixing hotspots based on the results from observations and output from a model. For this research glider and CCS data were used, the positions of those sources of data are shown on figure 5.1.

In section (5.3) methods and data, which were used in this chapter, are presented. Section 5.4 represents the impact of stratification and topography on internal mixing in a continental shelf sea. Later, the predictability of mixing in shelf seas is discussed.

Here we would like to answer to the following question - do we see the increase of mixing and turbulence under stronger stratification and deeper pycnocline, as we have seen with the IW field; and if there is such an increase, is it possible to predict it? By the end of this chapter we will show how changes in stratification and topography impact on mixing in a continental shelf sea.

5.3 The effect of stratification and topography on turbulence

In the previous chapters the results from the MITgcm model has shown that a tighter and deeper pycnocline results in an increase in baroclinic energy compared with a shallow and diffused pycnocline. This energy is a potential source for sustaining mixing and turbulence in the pycnocline. To test if mixing and turbulence are dependent on initial stratification scenarios, we have used a combination of modelled and observational (mooring and glider) data.

As introduced in the section 1.3.4, one of the most important properties of turbulence is that it generates large velocity gradients at small scales [Thorpe, 2005], resulting in enhanced shear. When shear increases relative to stratification in a stratified fluid, there is an increased chance for the flow to become unstable.This relationship is described by the equation 1.28.

Figure 5.2 shows the N_b^2 averaged through MITgcm timespan for the chosen domain for three different initial stratification scenarios, which are shown at the bottom-right panel on the figure 5.2, for the same dominant tidal forcing.

In the Normal case, the maximum values for the N_b^2 are over the largest banks, but it reaches $1.5 \times 10^{-4}\,\mathrm{s}^{-2}$. The similar distribution of the N_b^2 values is observed for the Tight case, the maximum values over main banks with the values reaching $1.6 \times 10^{-4}\,\mathrm{s}^{-2}$. Though there are high values of the N_b^2 in off-shelf region in the Tight case. The maximum values for the N_b^2 for the Deep case are the lowest and equal to $1.1 \times 10^{-4}\,\mathrm{s}^{-2}$, compared to the Normal and Tight cases, though the initial stratification was much stronger for the Deep cases, than for the Normal case. This is due to higher mixing in the Deep case.

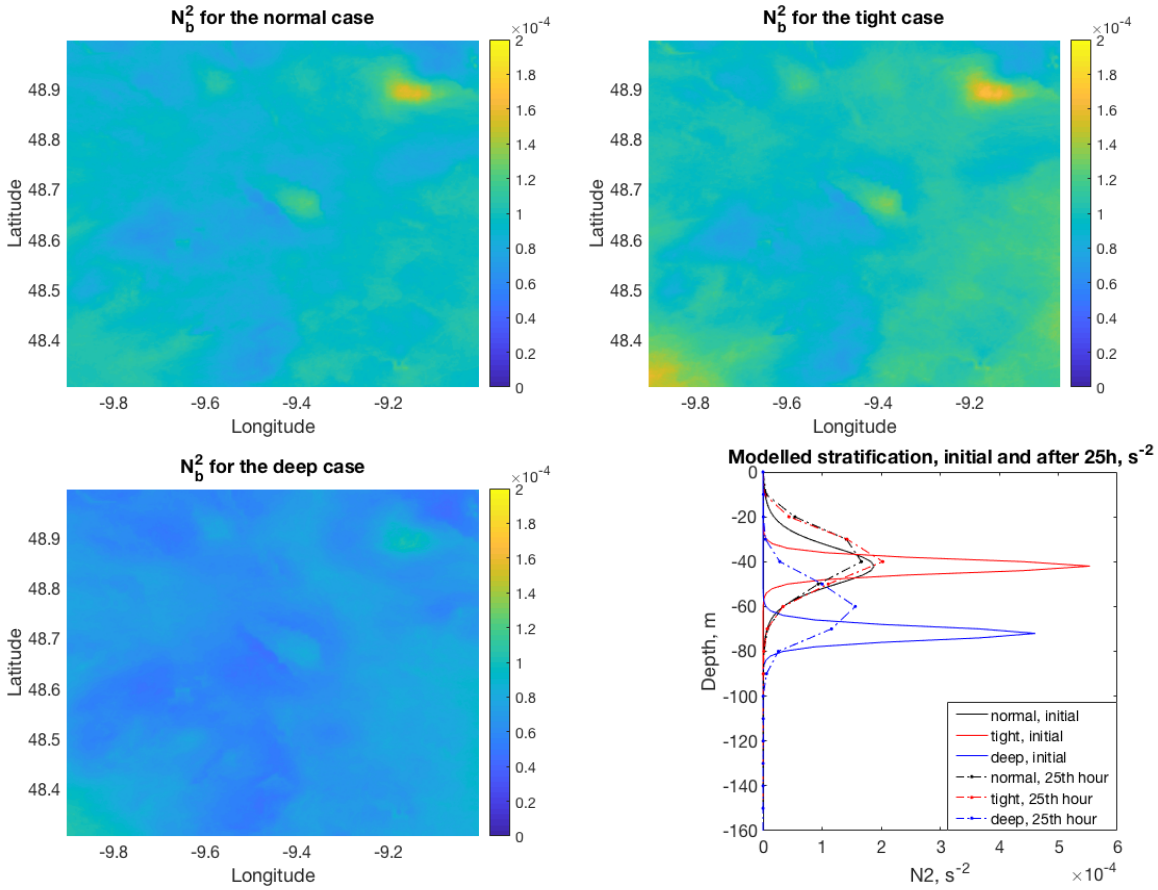

Fig. 5.2 N_b^2 for the chosen MITgcm domain under three different stratification scenarios, s^{-2}. The stratification plot shows the initial stratification scenarios and results after 25 hours for the three different scenarios for MITgcm runs.

Figure 5.3 shows the S_b^2 averaged through MITgcm timespan for the chosen domain for three different cases. The maximum values for the S_b^2 are near the largest banks, similar to the previous plot. The Normal case reaches values higher than $10^{-4}\,s^{-2}$, similar to the Tight case, though the Tight case has a broader area with such values. The Deep case is reaching values around $9 \times 10^{-3}\,s^{-2}$, which is larger than the Normal and Tight cases, mainly due to higher mixing in the Deep case. From these results we can conclude that the Deep case has higher chance for mixing and instability.

Figure 5.4 shows the minimum values (in depth and time) for $Ri_{g\%}$ (equation 1.35) for the chosen domain for the three different cases. The Deep case has much broader spread of critical $Ri_{g\%}$ of order of 1 and lower (this criticality was specified at the beginning of

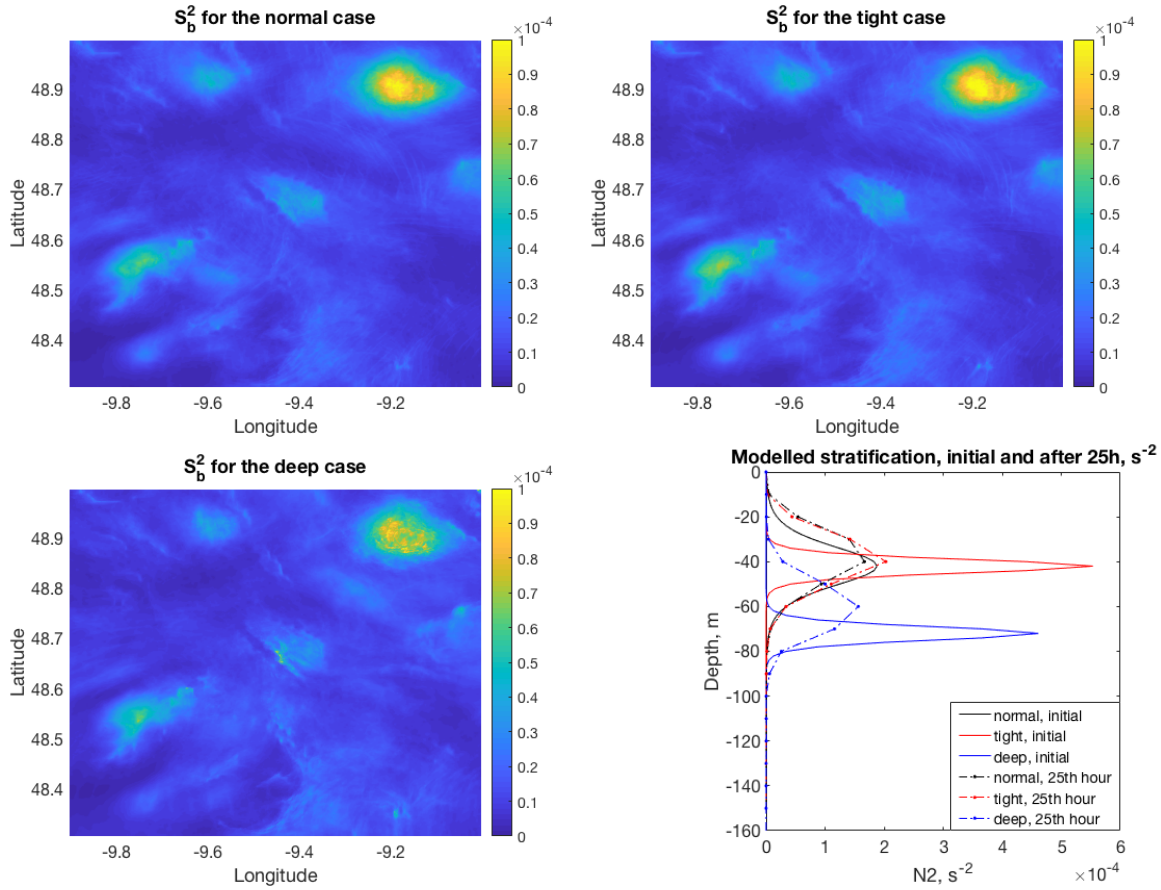

Fig. 5.3 S_b^2 for the chosen MITgcm domain under three different stratification scenarios, s^{-2}. The stratification plot shows the initial stratification scenarios and results after 25 hours for the three different scenarios for MITgcm runs.

the chapter 5.4), compared to the Normal and Tight cases. All three cases have critical Ri_g mainly over main banks and near shelf break.

Figure 5.5 shows the percentage of times when $Ri_{g\%}$ reached the critical value of 1 for the chosen domain for three different cases for the dominant tidal forcing. There is a similar distribution to the N_b^2, fig. 5.2 and S_b^2, fig. 5.3. However, the Deep case has much higher values compared to other two cases. In the Normal case, the over bank areas have from 15 to 30% of the model period, when the $Ri_{g\%}$ was close to critical values (less than 1). In these areas there is a higher chance of mixing and turbulence. The rest of the model domain is covered with values of order of $5-10\%$. In the Tight case, over bank areas were characterised by $Ri_{g\%}$ between 25 to 40% of the model period. In the rest of the model

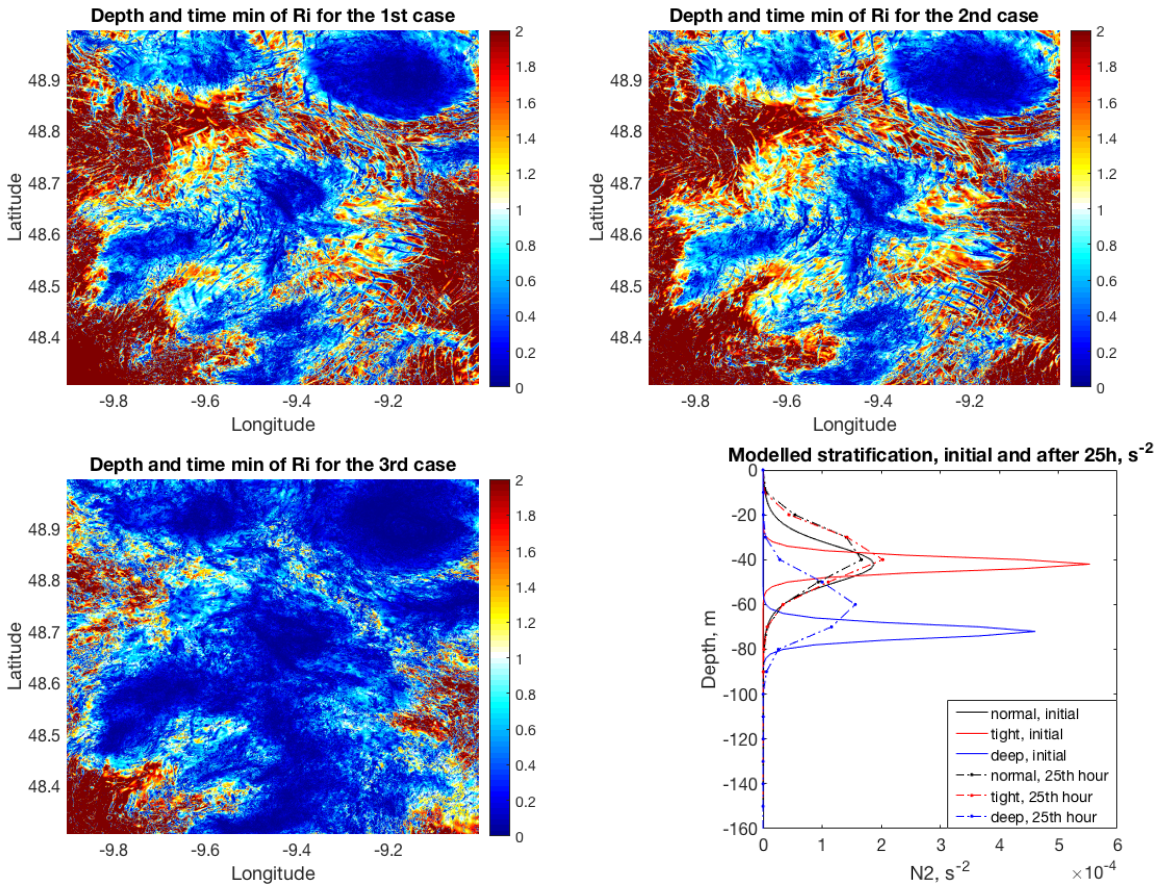

Fig. 5.4 Time and depth minimum of $Ri_{g\%}$ for the chosen MITgcm domain under three different stratification scenarios. The dramatic change in stratification leads to the increase in Ri number, especially on a shelf break and areas with critical topography. The stratification plot shows the initial stratification scenarios and results after 25h for the three different scenarios for MITgcm runs.

domain $Ri_{g\%}$ occurred only 15% of the time. There are more areas where the $Ri_{g\%}$ is closer to critical values, compared to the Normal case. In the Deep case, in over bank areas, $Ri_{g\%}$ occurs from 30 to more than 50% of the model period. This suggests that in the case of a tight and deep pycnocline over banks areas, there is a 50% chance of mixing and turbulence. Much of the rest of the model domain is covered with values of order of 20%. The shelf break areas become turbulent as well. From these results we can conclude that by increasing the maximum values of N_b^2 we are not greatly increasing the chances of mixing, but the depth of the pycnocline is playing a much bigger role, similar to HKE, see chapter 4.

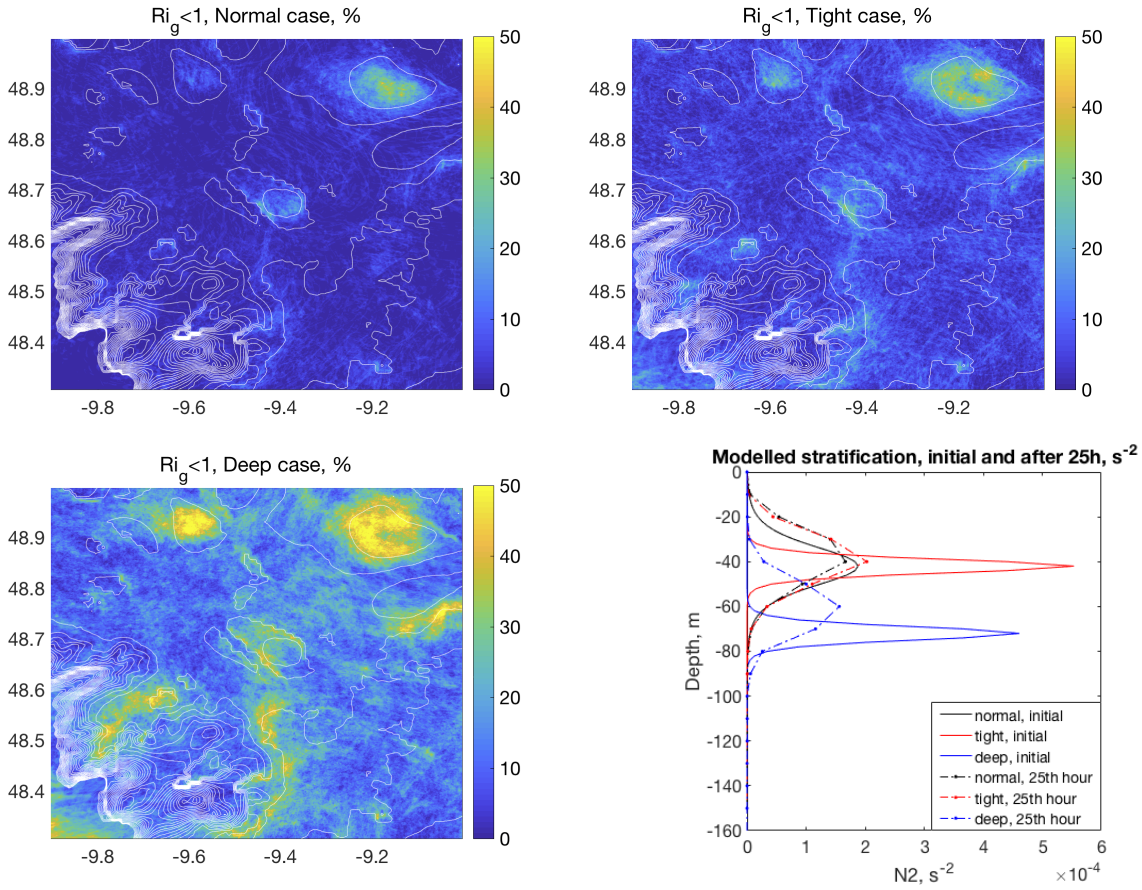

Fig. 5.5 $Ri_{g\%}$ for the chosen MITgcm domain under three different stratification scenarios, analogous to the number of times when the Ri number has reached critical values. The stratification plot shows the initial stratification scenarios and results after 25h for the three different scenarios for MITgcm runs.

The figure 5.6 shows the comparison of the depth integrated HKE for the 1st mode for the point CCS between different seasons - spring, summer, autumn, and the total depth integrated HKE for the 1st mode calculated for the period 2014-2015 in Ri number space. There is a clear dependancy between HKE and S_b^2, N_b^2 in total 2014-2015 and autumn periods - depth integrated baroclinic HKE is increasing with S_b^2, N_b^2. Whereas, summer depth integrated baroclinic HKE and spring depth integrated baroclinic HKE is highly dependant on S_b^2, probably due to intensified wind mixing. But the results for spring and summer might as well depend on limited amount of data which were provided for this research, it might be useful to check these results on several years in similar areas.

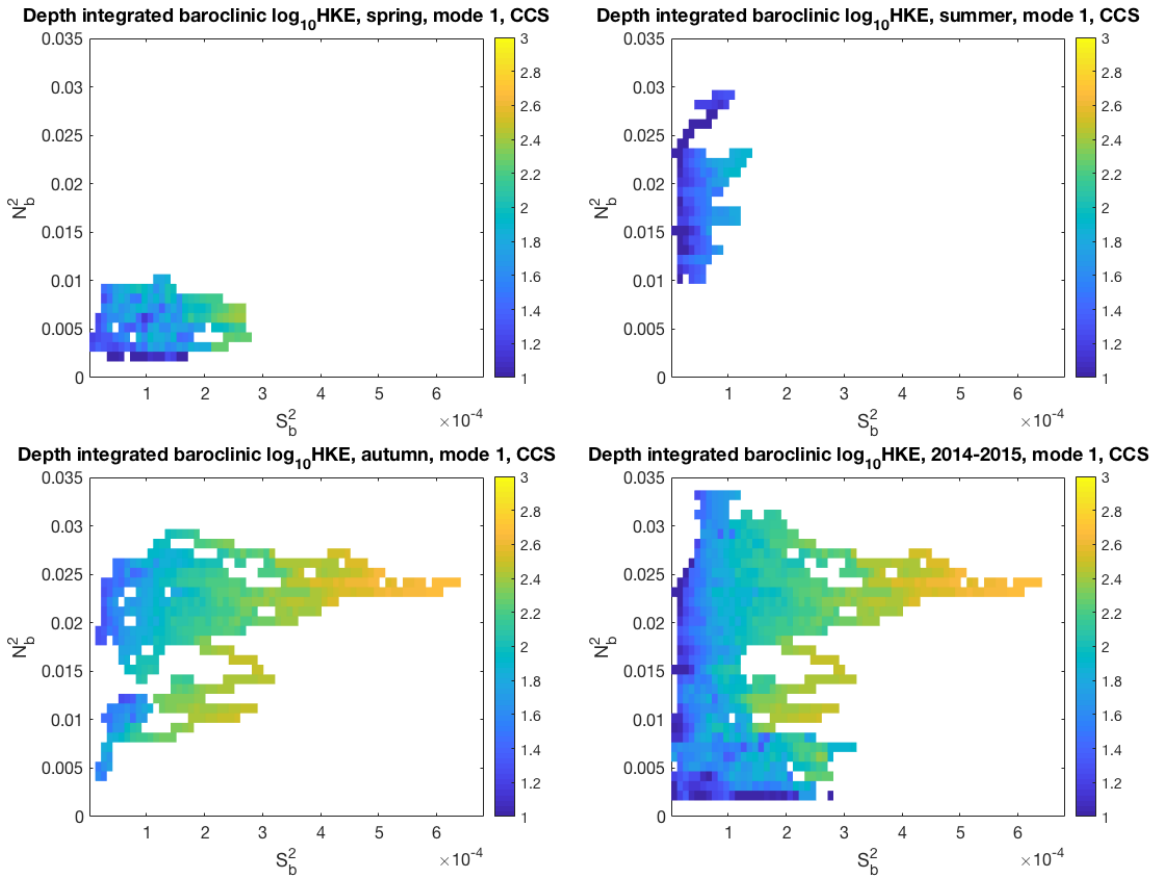

Fig. 5.6 Baroclinic HKE for the 1st mode for the CCS data in the Ri number space.

Similarly to the figure 4.7, the figure 5.7 shows the dependency between total depth integrated energy flux versus S_b^2, N_b^2 and the dependency between total depth integrated energy flux for the M_2 frequency versus S_b^2, N_b^2. The results for the total depth integrated energy flux suggests a coherent increase in total energy flux with S_b^2 and N_b^2. The higher total energy flux values, between 200 and 300 $\mathrm{m^2\,s^{-2}}$, most of the time lie on N_b^2 values, higher than $4 \cdot 10^{-4} s^{-2}$. The total energy flux is highly dependant on the N_b^2, rather on S_b^2, though there is a slight increase of energy flux values with increase in S_b^2.

5.4 Summary

In this chapter we have found the connections between internal wave (IW) dynamics and turbulent mixing over different topographies and under different dynamical forcing in a

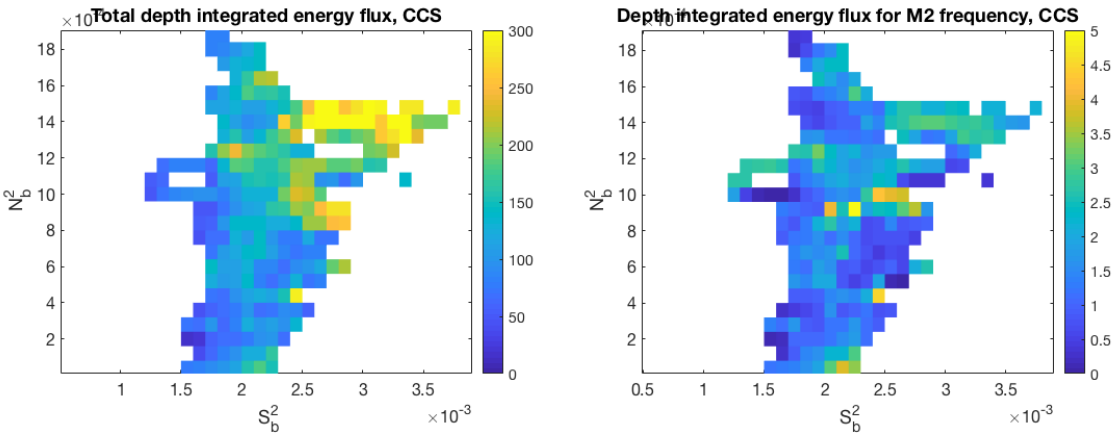

Fig. 5.7 Total depth integrated energy flux vs S_b^2 and N_b^2, depth integrated energy flux for the M2 frequency vs S_b^2 and N_b^2 for CCS data.

continental shelf seas, by using modelled and observational data. During our research it has been identified that the $Ri_{g\%}$ shows a clear dependency on three modelled cases, with the highest numbers of order of 70% in the Deep case, which suggests that there is a higher chance of turbulent mixing in case of deep and tight pycnocline. More research should be done in this area to confirm this connection, especially on a datasets with ε and velocity data, which were collected in the exactly same location and time.

Chapter 6

Discussion

The aim of this thesis was to increase our understanding of internal wave (IW) dynamics over different topographies and varying stratification in continental shelf seas through a combination of observational and modelling based methods. A key component of this work has been results from a newly configured version of the MITgcm non-hydrostatic model, which includes a very high horizontal resolution of 50m to enable the accurate simulation of a realistic internal wave field including high-frequency internal waves and solitons. Results from this model suggest that during periods of increasing stratification, analogous to when summer storms act to tighten the pycnocline and pushing it deeper in the water column, the IW field becomes more energetic. While this is intuitive, an important new result from this work is that this increase in energy is not evenly distributed, either spatially or spectrally.

The spatial variability in this response in IW energy is clearly divisible between on-shelf and off-shelf areas. In off-shelf regions, when IWs are propagating into the open ocean, the spectral cascade of internal wave energy is shown to be similar to the GM spectrum [Garrett and Munk, 1972b, 1975], reducing relative to frequency (ω) as ω^{-2}. On the shelf, the spectral cascade of energy is suggested by the model to vary under different stratification scenarios, represented in the model as changes in the initial stratification. These results show a disproportionate increase in baroclinic energy with the high frequency end of the IW spectrum identifiable as a flatter spectral shape. Spectral analysis from each of the 3 scenarios tested here, reveals an inverse relation between the strength of stratification and

spectral slope, where a strong and deep pycnocline (Deep case in this study) leads to the shallowest slope. Even subtle changes in stratification and topography are shown to result in the redistribution of IW energy.

Ocean observations of the density and current velocity structure were used to test the true IW response to similar changes in stratification scenarios to those used in the three chosen model case studies. The true variability in the system, due largely to spring-neap and seasonal cycles, covered a far broader range of scenarios. Direct comparison of model and observational results was therefore difficult. There is however, evidence of similar behaviour to the spectral cascade of IW energy in observational data to that from the MITgcm model. Results from the unique 17-month time series of current velocity and vertical density structure from the Central Celtic Sea (CCS) mooring was used to assess the predictability of internal wave energy under seasonally varying stratification scenarios. It was difficult to directly distinguish the three different model cases in the observational data, owing to an inconsistency in the occurrence of cases; with only a small amount of the Deep case scenarios being observed, all of which were during the autumn. Similar conditions to Normal and Tight cases were observed throughout summer and spring stratified periods. While the amount of the Deep case occurrences is not high, it is observed that this case did produce a significant increase in HKE during autumn months. HKE increases two-fold during these autumnal periods. This is an important result as it suggests that while the increase in wind energy acts to break down summer stratification, the relocation of the pycnocline deeper in the water column acts to increase baroclinic energy within the system.

There are many processes present within the observed IW field that are not well represented in the three model cases. The high-resolution model used in this study however, has successfully produced a realistic IW field, including high-frequency waves and solitary waves. This study has therefore enabled the effects of different stratification scenarios on the entire IW wave field, not just on low frequency components such as the dominant, M_2, frequency. The regularity with which the gradient Richardson number reached near critical values (shown as a percentage of time conditions reached $Ri_g < 1$, figures 5.6, 5.7) shows a dependency on three modelled cases. While similar results were observed for the Normal

and Tight case scenarios, the Deep case demonstrated dramatic increases in regularity of near critical conditions, with occurrences order 70% of the time being reached. This suggests that there is a higher chance that conditions will be conducive for turbulent mixing when conditions produce a deep and tight pycnocline. Relating this result to the observed behaviour in HKE during these typically autumn conditions, suggests that the storm driven conditions could potentially provide a second-order mechanism that contributes to the breakdown of seasonal stratification. The regularity of $Ri_g < 1$ conditions in model data increases with stratification, ranging from 4 to 70%.

The thesis brings together two unique datasets that permit comparable analysis from both models and observations of internal waves generated under a wide range of conditions on a continental shelf sea. This work identifies an identifiable and quantifiable response in the spectral distribution of internal wave energy that suggests that the IW behaviour on shelf seas is predictable. As this investigation has edged closer towards analysis of turbulence and mixing, the links to initial stratification scenarios have become less well idefintified. This is to be expected as more non-linear terms become stronger and the chaotic, random nature of turbulence becomes more evident. This work has however, identified an apparently strong relationship with how conditions for turbulence change relative to stratification scenarios and that a potential criticality exists that leads to a change in turbulence or mixing behaviour.

As more coincident density, current velocity and dissipation rate data becomes available from improved observational capability in this field, this work may be taken forward to identify stronger relationships between these parameters that may produce an improved parameterisation of turbulence and mixing in shelf seas. This thesis provides a stepping stone for this future work.

This work has important implication in the case of climate change when an increase in temperature and the incidence of storms may occur. IW energy may, in this instance, increase and the spectral slope could become shallower which will result in higher energy content in higher frequencies. This may have implications for the propagation distance of IWs over the shelf, which will likely have an impact on biological productivity in these regions.

References

M. H. Alford. Redistribution of energy available for ocean mixing by long-range propagation of internal waves. *Nature*, 2003.

M. H. Alford, T. Peacock, J. A. MacKinnon, and J. D. Nash. The formation and fate of internal waves in the south china sea. *Nature*, 521, 2015. doi: https://doi.org/10.1038/nature14399.

J. R. Apel. Oceanic internal waves and solitons. *An atlas of oceanic internal solitary waves*, pages 1–40, 2002.

J. R. Apel. An atlas of internal solitary-like waves and their properties, 2004. URL https://www.internalwaveatlas.com/.

J. R. Apel, H. M. Byrne, J. R. Proni, and R. L. Charnell. Observations of oceanic internal and surface waves from the earth resources technology satellite. *Journal of Geophysical Research*, 80(6):865–881, 1975. doi: 10.1029/JC080i006p00865. URL https://agupubs.onlinelibrary.wiley.com/doi/abs/10.1029/JC080i006p00865.

J. R. Apel, L. A. Ostrovsky, Y. A. Stepanyants, and J. F. Lynch. Internal solitons in the ocean. *WHOI Technical Reports*, 2006. doi: 10.1575/1912/1070. URL https://hdl.handle.net/1912/1070.

J. Boussinesq. Essai sur la theorie des eaux courantes. *Memoires presentes par divers savants a l?Academie des Sciences de l?Institut National de France, Tome XXIII, No 1*, 1877.

K. Brink and A. Robinson. *The Global Coastal Ocean - Processes and Methods*. Sea: Ideas and Observations on. Harvard University Press, 2005. ISBN 9780674017405. URL https://books.google.co.uk/books?id=Ie91TPjB6EgC.

G. S. Carter, M. A. Merrifield, J. M. Becker, K. Katsumata, M. C. Gregg, D. S. Luther, M. D. Levine, T. J. Boyd, and Y. L. Firing. Energetics of m2 barotropic-to-baroclinic tidal conversion at the hawaiian islands. *Journal of Physical Oceanography*, 38(10):2205–2223, 2008. doi: 10.1175/2008JPO3860.1. URL https://doi.org/10.1175/2008JPO3860.1.

E. A. D'Asaro. The energy flux from the wind to near-inertial motions in the surface mixed layer. *Journal of Physical Oceanography*, 15(8):1043–1059, 1985. doi: 10.1175/1520-0485(1985)015<1043:TEFFTW>2.0.CO;2. URL https://doi.org/10.1175/1520-0485(1985)015<1043:TEFFTW>2.0.CO;2.

E. A. D'Asaro, R.-C. Lien, and F. Henyey. High-frequency internal waves on the oregon continental shelf. *Journal of physical oceanography*, 37(7):1956–1967, 2007.

B. D. Dushaw, B. M. Howe, B. D. Cornuelle, P. F. Worcester, and D. S. Luther. Barotropic and baroclinic tides in the central north pacific ocean determined from long-range reciprocal acoustic transmissions. *Journal of Physical Oceanography*, 25(4):631–647, 1995. doi: 10.1175/1520-0485(1995)025<0631:BABTIT>2.0.CO;2. URL https://doi.org/10.1175/1520-0485(1995)025<0631:BABTIT>2.0.CO;2.

G. D. Egbert and R. D. Ray. Significant dissipation of tidal energy in the deep ocean inferred from satellite altimeter data. *Nature*, 405(6788):775–778, 2000. doi: 10.1038/35015531. URL https://doi.org/10.1038/35015531.

G. D. Egbert and R. D. Ray. Estimates of m2 tidal energy dissipation from topex/poseidon altimeter data. *Journal of Geophysical Research: Oceans*, 106(C10):22475–22502, 2001.

F. El-Baz and D. M. Warner. Apollo-soyuz summary science report. *NASA Lyndon B. Johnson Space Center*, 2, 1979.

ESA. Oceanic internal waves, 2016-08-30. URL https://earth.esa.int/.

A. Filonov and V. Novotryasov. Features of the nonlinear internal wave spectrum in the coastal zone. *Geophysical Research Letters*, 32(15), 2005. doi: 10.1029/2005GL023046. URL https://agupubs.onlinelibrary.wiley.com/doi/abs/10.1029/2005GL023046.

C. Garrett. Book review. *Limnology and Oceanography Bulletin*, 15(1):1–2, 2006. doi: 10.1002/lob.20061511. URL https://aslopubs.onlinelibrary.wiley.com/doi/abs/10.1002/lob.20061511.

C. Garrett and E. Kunze. Internal tide generation in the deep ocean. *Annual Review of Fluid Mechanics*, 39(1):57–87, 2007. doi: 10.1146/annurev.fluid.39.050905.110227. URL https://doi.org/10.1146/annurev.fluid.39.050905.110227.

C. Garrett and W. Munk. Oceanic mixing by breaking internal waves. *Deep Sea Research and Oceanographic Abstracts*, 19(12):823 – 832, 1972a. ISSN 0011-7471. doi: https://doi.org/10.1016/0011-7471(72)90001-0. URL http://www.sciencedirect.com/science/article/pii/0011747172900010.

C. Garrett and W. Munk. Space-time scales of internal waves. *Geophysical Fluid Dynamics*, 3(1):225–264, 1972b. doi: 10.1080/03091927208236082. URL https://doi.org/10.1080/03091927208236082.

C. Garrett and W. Munk. Space-time scales of internal waves: A progress report. *Journal of Geophysical Research*, 80(3):291–297, 1975. doi: 10.1029/JC080i003p00291. URL https://agupubs.onlinelibrary.wiley.com/doi/abs/10.1029/JC080i003p00291.

GEBCO. Gebco, 2016-08-30. URL http://gebco.net/.

T. Gerkema and J. Zimmerman. An introduction to internal waves. *Lecture Notes, Royal NIOZ, Texel*, 207, 2008.

M. Gregg. Small-scale mixing: a first-order process. In *Parameterization of Small-Scale Processes, Proceedings of the'Aha Huliko'a Hawaiian Winter Workshop*, pages 117–126. Hawaiian Institute of Geophysics, Honolulu, 1989a.

M. C. Gregg. Scaling turbulent dissipation in the thermocline. *Journal of Geophysical Research: Oceans*, 94(C7):9686–9698, 1989b. doi: 10.1029/JC094iC07p09686. URL https://agupubs.onlinelibrary.wiley.com/doi/abs/10.1029/JC094iC07p09686.

J. Grue, A. Jensen, P.-O. Rusås, and J. K. Sveen. Properties of large-amplitude internal waves. *Journal of Fluid Mechanics*, 380:257–278, 1999.

R. A. Hall and G. S. Carter. Internal tides in monterey submarine canyon. *Journal of Physical Oceanography*, 41(1):186–204, 2011. doi: 10.1175/2010JPO4471.1. URL https://doi.org/10.1175/2010JPO4471.1.

R. A. Hall, M. H. Alford, G. S. Carter, M. C. Gregg, R.-C. Lien, D. J. Wain, and Z. Zhao. Transition from partly standing to progressive internal tides in monterey submarine canyon. *Deep Sea Research Part II: Topical Studies in Oceanography*, 104:164 – 173, 2014. ISSN 0967-0645. doi: https://doi.org/10.1016/j.dsr2.2013.05.039. URL http://www.sciencedirect.com/science/article/pii/S0967064513002300. Submarine Canyons: Complex Deep-Sea Environments Unravelled by Multidisciplinary Research.

C. D. Helfrich, Y.-F. Li, N. D. Sharp, and A. E. Sales. Organizational readiness to change assessment (orca): Development of an instrument based on the promoting action on research in health services (parihs) framework. *Implementation Science*, 4(1):38, Jul 2009. ISSN 1748-5908. doi: 10.1186/1748-5908-4-38. URL https://doi.org/10.1186/1748-5908-4-38.

K. R. Helfrich and W. K. Melville. On long nonlinear internal waves over slope-shelf topography. *Journal of Fluid Mechanics*, 167:285–308, 1986. doi: 10.1017/S0022112086002823.

B. Helland-Hansen and F. Nansen. The norwegian sea, its physical oceanography.based on the norwegian researches 1900-1904. *Technical Report 390, Report on Norwegian fishery and marine-investigations, vol. 2, Bergen, Norway.*, 1909.

F. S. Henyey, J. Wright, and S. M. Flatte. Energy and action flow through the internal wave field: An eikonal approach. *Journal of Geophysical Research: Oceans*, 91(C7):8487–8495, 1986. doi: 10.1029/JC091iC07p08487. URL https://agupubs.onlinelibrary.wiley.com/doi/abs/10.1029/JC091iC07p08487.

T. Hibiya, Y. Niwa, and K. Fujiwara. Numerical experiments of nonlinear energy transfer within the oceanic internal wave spectrum. *Journal of Geophysical Research: Oceans*, 103 (C9):18715–18722, 1998. doi: 10.1029/98JC01362. URL https://agupubs.onlinelibrary.wiley.com/doi/abs/10.1029/98JC01362.

J. Holt and S. Thorpe. The propagation of high frequency internal waves in the celtic sea. *Deep Sea Research Part I: Oceanographic Research Papers*, 44(12):2087 – 2116, 1997. ISSN 0967-0637. doi: https://doi.org/10.1016/S0967-0637(97)00091-5. URL http://www.sciencedirect.com/science/article/pii/S0967063797000915.

J. E. Hopkins, G. R. Stephenson Jr., J. A. M. Green, M. E. Inall, and M. R. Palmer. Storms modify baroclinic energy fluxes in a seasonally stratified shelf sea: Inertial-tidal interaction. *Journal of Geophysical Research: Oceans*, 119(10):6863–6883, 2014. doi: 10.1002/2014JC010011. URL https://agupubs.onlinelibrary.wiley.com/doi/abs/10.1002/2014JC010011.

L. N. Howard. Note on a paper of john w. miles. *Journal of Fluid Mechanics*, 10(4):509?512, 1961. doi: 10.1017/S0022112061000317.

B. A. Hughes. The effect of internal waves on surface wind waves 2. theoretical analysis. *Journal of Geophysical Research: Oceans*, 83(C1):455–465, 1978. doi: 10.1029/JC083iC01p00455. URL https://agupubs.onlinelibrary.wiley.com/doi/abs/10.1029/JC083iC01p00455.

J. M. Huthnance. Circulation, exchange and water masses at the ocean margin: the role of physical processes at the shelf edge. *Progress in Oceanography*, 35(4):353 – 431, 1995. ISSN 0079-6611. doi: https://doi.org/10.1016/0079-6611(95)80003-C. URL http://www.sciencedirect.com/science/article/pii/007966119580003C.

P. Hyder, D. Jeans, E. Cauquil, and R. Nerzic. Observations and predictability of internal solitons in the northern andaman sea. *Applied Ocean Research*, 27(1):1 – 11, 2005. ISSN 0141-1187. doi: https://doi.org/10.1016/j.apor.2005.07.001. URL http://www.sciencedirect.com/science/article/pii/S0141118705000222.

M. Inall, D. Aleynik, T. Boyd, M. Palmer, and J. Sharples. Internal tide coherence and decay over a wide shelf sea. *Geophysical Research Letters*, 38(23), 2011. doi: 10.1029/2011GL049943. URL https://agupubs.onlinelibrary.wiley.com/doi/abs/10.1029/2011GL049943.

D. Kang and O. Fringer. On the calculation of available potential energy in internal wave fields. *Journal of Physical Oceanography*, 40(11):2539–2545, 2010. doi: 10.1175/2010JPO4497.1. URL https://doi.org/10.1175/2010JPO4497.1.

V. Klemas. Remote sensing of ocean internal waves: An overview. *Journal of Coastal Research*, 28(3):540–546, 2012.

J. M. Klymak and J. N. Moum. Internal solitary waves of elevation advancing on a shoaling shelf. *Geophysical Research Letters*, 30(20), 2003.

J. M. Klymak, J. N. Moum, J. D. Nash, E. Kunze, J. B. Girton, G. S. Carter, C. M. Lee, T. B. Sanford, and M. C. Gregg. An estimate of tidal energy lost to turbulence at the hawaiian ridge. *Journal of Physical Oceanography*, 36(6):1148–1164, 2006. doi: 10.1175/JPO2885.1. URL https://doi.org/10.1175/JPO2885.1.

J. M. Klymak, R. Pinkel, and L. Rainville. Direct breaking of the internal tide near topography: Kaena ridge, hawaii. *Journal of Physical Oceanography*, 38(2):380–399, 2008. doi: 10.1175/2007JPO3728.1. URL https://doi.org/10.1175/2007JPO3728.1.

D. D. J. Korteweg and D. G. de Vries. Xli. on the change of form of long waves advancing in a rectangular canal, and on a new type of long stationary waves. *The London, Edinburgh, and Dublin Philosophical Magazine and Journal of Science*, 39(240):422–443, 1895. doi: 10.1080/14786449508620739. URL https://doi.org/10.1080/14786449508620739.

E. Kunze and T. B. Sanford. Abyssal mixing: Where it is not. *Journal of Physical Oceanography*, 26(10):2286–2296, 1996. doi: 10.1175/1520-0485(1996)026<2286:AMWIIN>2.0.CO;2. URL https://doi.org/10.1175/1520-0485(1996)026<2286:AMWIIN>2.0.CO;2.

E. Kunze, E. Firing, J. M. Hummon, T. K. Chereskin, and A. M. Thurnherr. Global abyssal mixing inferred from lowered adcp shear and ctd strain profiles. *Journal of Physical Oceanography*, 36(8):1553–1576, 2006. doi: 10.1175/JPO2926.1. URL https://doi.org/10.1175/JPO2926.1.

K. Lambeck. The earth's variable rotation: Some geophysical causes. In *Reference Frames*, pages 241–284. Springer, 1989.

P. LeBlond and L. Mysak. *Waves in the Ocean*. Elsevier Oceanography Series. Elsevier Science, 1981. ISBN 9780080879772. URL https://books.google.co.uk/books?id=TYGIwzz_k8kC.

P. H. LeBlond. On tidal propagation in shallow rivers. *Journal of Geophysical Research: Oceans*, 83(C9):4717–4721, 1978. doi: 10.1029/JC083iC09p04717. URL https://agupubs.onlinelibrary.wiley.com/doi/abs/10.1029/JC083iC09p04717.

M. D. Levine. A modification of the garrett–munk internal wave spectrum. *Journal of Physical Oceanography*, 32(11):3166–3181, 2002. doi: 10.1175/1520-0485(2002)032<3166:AMOTGM>2.0.CO;2. URL https://doi.org/10.1175/1520-0485(2002)032<3166:AMOTGM>2.0.CO;2.

Y. Liang, A. Zareei, and M.-R. Alam. Inherently unstable internal gravity waves due to resonant harmonic generation. *Journal of Fluid Mechanics*, 811:400–420, 2017. doi: 10.1017/jfm.2016.754.

Y. Lu and R. G. Lueck. Using a broadband adcp in a tidal channel. part i: Mean flow and shear. *Journal of Atmospheric and Oceanic Technology*, 16(11):1556–1567, 1999.

S. A. Mack and H. C. Schoeberlein. Richardson number and ocean mixing: Towed chain observations. *Journal of Physical Oceanography*, 34(4):736–754, 2004. doi: 10.1175/1520-0485(2004)034<0736:RNAOMT>2.0.CO;2. URL https://doi.org/10.1175/1520-0485(2004)034<0736:RNAOMT>2.0.CO;2.

J. MacKinnon, M. Alford, J. Ansong, B. Arbic, A. Barna, B. Briegleb, F. Bryan, M. Buijsman, E. Chassignet, G. Danabasoglu, S. Diggs, S. Griffies, R. Hallberg, S. Jayne, M. Jochum, J. Klymak, E. Kunze, W. Large, S. Legg, and Z. Zhao. Climate process team on internal-wave driven ocean mixing. *Bulletin of the American Meteorological Society*, 98, 03 2017. doi: 10.1175/BAMS-D-16-0030.1.

J. A. MacKinnon and M. C. Gregg. Mixing on the late-summer new england shelf—solibores, shear, and stratification. *Journal of Physical Oceanography*, 33(7):1476–1492, 2003. doi: 10.1175/1520-0485(2003)033<1476:MOTLNE>2.0.CO;2. URL https://doi.org/10.1175/1520-0485(2003)033<1476:MOTLNE>2.0.CO;2.

J. Marshall, C. Hill, L. Perelman, and A. Adcroft. Hydrostatic, quasi-hydrostatic, and nonhydrostatic ocean modeling. *Journal of Geophysical Research: Oceans*, 102(C3):5733–5752, 1997. doi: 10.1029/96JC02776. URL https://agupubs.onlinelibrary.wiley.com/doi/abs/10.1029/96JC02776.

J. W. Miles. On the stability of heterogeneous shear flows. *Journal of Fluid Mechanics*, 10 (4):496?508, 1961. doi: 10.1017/S0022112061000305.

J. W. Miles. The korteweg-de vries equation: a historical essay. *Journal of Fluid Mechanics*, 106:131–147, 1981. doi: 10.1017/S0022112081001559.

G. R. Miller. The flux of tidal energy out of the deep oceans. *Journal of Geophysical Research*, 71(10):2485–2489, 1966. doi: 10.1029/JZ071i010p02485. URL https://agupubs.onlinelibrary.wiley.com/doi/abs/10.1029/JZ071i010p02485.

MITgcm. Mitgcm, 2016-08-30. URL http://mitgcm.org/.

S. N. Moshonkin, A. V. Gusev, V. B. Zalesny, and V. I. Byshev. Mixing parameterizations in ocean climate modeling. *Izvestiya, Atmospheric and Oceanic Physics*, 52(2):196–206, Mar 2016. ISSN 1555-628X. doi: 10.1134/S0001433816010084. URL https://doi.org/10.1134/S0001433816010084.

J. N. Moum, J. M. Klymak, J. D. Nash, A. Perlin, and W. D. Smyth. Energy transport by nonlinear internal waves. *Journal of Physical Oceanography*, 37(7):1968–1988, 2007. doi: 10.1175/JPO3094.1. URL https://doi.org/10.1175/JPO3094.1.

W. Munk. Internal waves and small-scale processes. *Evolution of Physical Oceanography*, 1981.

W. Munk and C. Wunsch. Abyssal recipes ii: energetics of tidal and wind mixing. *Deep Sea Research Part I: Oceanographic Research Papers*, 45(12):1977 – 2010, 1998. ISSN 0967-0637. doi: https://doi.org/10.1016/S0967-0637(98)00070-3. URL http://www.sciencedirect.com/science/article/pii/S0967063798000703.

M. Nagasawa, T. Hibiya, Y. Niwa, M. Watanabe, Y. Isoda, S. Takagi, and Y. Kamei. Distribution of fine-scale shear in the deep waters of the north pacific obtained using expendable current profilers. *Journal of Geophysical Research: Oceans*, 107(C12), 2002.

F. Nansen. *Farthest North*. Archibald Constable, 1897.

NASA. Nasa, 2016-08-30. URL https://www.giss.nasa.gov/.

J. D. Nash and J. N. Moum. Internal hydraulic flows on the continental shelf: High drag states over a small bank. *Journal of Geophysical Research: Oceans*, 106(C3):4593–4611, 2001. doi: 10.1029/1999JC000183. URL https://agupubs.onlinelibrary.wiley.com/doi/abs/10.1029/1999JC000183.

J. D. Nash, M. H. Alford, and E. Kunze. Estimating internal wave energy fluxes in the ocean. *Journal of Atmospheric and Oceanic Technology*, 22(10):1551–1570, 2005. doi: 10.1175/JTECH1784.1. URL https://doi.org/10.1175/JTECH1784.1.

J. D. Nash, M. H. Alford, E. Kunze, K. Martini, and S. Kelly. Hotspots of deep ocean mixing on the oregon continental slope. *Geophysical Research Letters*, 34(1), 2007. doi: 10.1029/2006GL028170. URL https://agupubs.onlinelibrary.wiley.com/doi/abs/10.1029/2006GL028170.

J. D. Nash, S. M. Kelly, E. L. Shroyer, J. N. Moum, and T. F. Duda. The unpredictable nature of internal tides on continental shelves. *Journal of Physical Oceanography*, 42(11):1981–2000, 2012. doi: 10.1175/JPO-D-12-028.1. URL https://doi.org/10.1175/JPO-D-12-028.1.

K. A. Nikolaevich. The local structure of turbulence in incompressible viscous fluid for very large reynolds' numbers. *Soviet Physics Uspekhi*, 1941.

A. R. Osborne and T. L. Burch. Internal solitons in the andaman sea. *Science*, 208(4443): 451–460, 1980. ISSN 0036-8075. doi: 10.1126/science.208.4443.451. URL http://science.sciencemag.org/content/208/4443/451.

R. Ozmidov. Energy distribution between oceanic motions of different scales. *Bull. Acad. Sci. USSR Atmos. Oceanic Phys.*, 1:257–261, 1965.

R. C. Pacanowski and S. G. H. Philander. Parameterization of vertical mixing in numerical models of tropical oceans. *Journal of Physical Oceanography*, 11(11):1443–1451, 1981. doi: 10.1175/1520-0485(1981)011<1443:POVMIN>2.0.CO;2. URL https://doi.org/10.1175/1520-0485(1981)011<1443:POVMIN>2.0.CO;2.

M. Palmer, G. Stephenson, M. Inall, C. Balfour, A. Düsterhus, and J. Green. Turbulence and mixing by internal waves in the celtic sea determined from ocean glider microstructure measurements. *Journal of Marine Systems*, 144:57 – 69, 2015. ISSN 0924-7963. doi: https://doi.org/10.1016/j.jmarsys.2014.11.005. URL http://www.sciencedirect.com/science/article/pii/S0924796314003108.

M. R. Palmer, M. E. Inall, and J. Sharples. The physical oceanography of jones bank: A mixing hotspot in the celtic sea. *Progress in Oceanography*, 117:9 – 24, 2013. ISSN 0079-6611. doi: https://doi.org/10.1016/j.pocean.2013.06.009. URL http://www.sciencedirect.com/science/article/pii/S0079661113000979. From Physics to Fishing over a Shelf Sea Bank.

A. Panton, C. Mahaffey, N. Greenwood, J. Hopkins, D. Montagnes, and J. Sharples. Short-term and seasonal variation in metabolic balance in liverpool bay. *Ocean Dynamics*, 62(2): 295–306, 2012.

R. Pingree and G. Mardell. Solitary internal waves in the celtic sea. *Progress in Oceanography*, 14:431 – 441, 1985. ISSN 0079-6611. doi: https://doi.org/10.1016/0079-6611(85)90021-7. URL http://www.sciencedirect.com/science/article/pii/0079661185900217.

R. D. Pingree, G. T. Mardell, D. E. Cartwright, D. H. Peregrine, J. C. Swallow, R. I. Currie, A. E. Gill, and J. H. Simpson. Slope turbulence, internal waves and phytoplankton growth at the celtic sea shelf-break. *Philosophical Transactions of the Royal Society of London. Series A, Mathematical and Physical Sciences*, 302(1472):663–682, 1981. doi: 10.1098/rsta.1981.0191. URL https://royalsocietypublishing.org/doi/abs/10.1098/rsta.1981.0191.

K. L. Polzin, J. M. Toole, and R. W. Schmitt. Finescale parameterizations of turbulent dissipation. *Journal of Physical Oceanography*, 25(3):306–328, 1995. doi: 10.1175/1520-0485(1995)025<0306:FPOTD>2.0.CO;2. URL https://doi.org/10.1175/1520-0485(1995)025<0306:FPOTD>2.0.CO;2.

G. R. Stephenson Jr., J. E. Hopkins, J. A. Mattias Green, M. E. Inall, and M. R. Palmer. Baroclinic energy flux at the continental shelf edge modified by wind-mixing. *Geophysical Research Letters*, 42(6):1826–1833, 2015. doi: 10.1002/2014GL062627. URL https://agupubs.onlinelibrary.wiley.com/doi/abs/10.1002/2014GL062627.

O. Reynolds. Iii. an experimental investigation of the circumstances which determine whether the motion of water shall be direct or sinuous, and of the law of resistance in parallel channels. *Proceedings of the royal society of London*, 35(224-226):84–99, 1883.

T. P. Rippeth and M. E. Inall. Observations of the internal tide and associated mixing across the malin shelf. *Journal of Geophysical Research: Oceans*, 107(C4):3–1–3–14, 2002. doi: 10.1029/2000JC000761. URL https://agupubs.onlinelibrary.wiley.com/doi/abs/10.1029/2000JC000761.

Royal Collection Trust. Leonardo da vinci, studies of turbulent water, royal collection trust, 2019. URL https://www.rct.uk/collection/themes/exhibitions/leonardo-da-vinci-a-life-in-drawing/the-queens-gallery-palace-of-hol-7.

D. L. Rudnick, T. M. S. Johnston, and J. T. Sherman. High-frequency internal waves near the luzon strait observed by underwater gliders. *Journal of Geophysical Research: Oceans*, 118(2):774–784, 2013. doi: 10.1002/jgrc.20083. URL https://agupubs.onlinelibrary.wiley.com/doi/abs/10.1002/jgrc.20083.

J. S. Russel. Report on waves". *Report of the fourteenth meeting of the British Association for the Advancement of Science, York*, 1844-1845.

J. Russell. *Report on Waves: Made to the Meetings of the British Association in 1842-43*. British Association, 1845. URL https://books.google.co.uk/books?id=994EAAAAYAAJ.

H. Sandstrom and J. A. Elliott. Internal tide and solitons on the scotian shelf: A nutrient pump at work. *Journal of Geophysical Research: Oceans*, 89(C4):6415–6426, 1984. doi: 10.1029/JC089iC04p06415. URL https://agupubs.onlinelibrary.wiley.com/doi/abs/10.1029/JC089iC04p06415.

A. Scotti and J. Pineda. Observation of very large and steep internal waves of elevation near the massachusetts coast. *Geophysical Research Letters*, 31(22), 2004. doi: 10.1029/2004GL021052. URL https://agupubs.onlinelibrary.wiley.com/doi/abs/10.1029/2004GL021052.

J. Sharples, M. C. Moore, T. P. Rippeth, P. M. Holligan, D. J. Hydes, N. R. Fisher, and J. H. Simpson. Phytoplankton distribution and survival in the thermocline. *Limnology and Oceanography*, 46(3):486–496, 2001. doi: 10.4319/lo.2001.46.3.0486. URL https://aslopubs.onlinelibrary.wiley.com/doi/abs/10.4319/lo.2001.46.3.0486.

J. Sharples, J. F. Tweddle, J. A. Mattias Green, M. R. Palmer, Y.-N. Kim, A. E. Hickman, P. M. Holligan, C. M. Moore, T. P. Rippeth, J. H. Simpson, and V. Krivtsov. Spring-neap modulation of internal tide mixing and vertical nitrate fluxes at a shelf edge in summer. *Limnology and Oceanography*, 52(5):1735–1747, 2007. doi: 10.4319/lo.2007.52.5.1735. URL https://aslopubs.onlinelibrary.wiley.com/doi/abs/10.4319/lo.2007.52.5.1735.

J. Simpson. Physical processes in the rofi regime. *Journal of Marine Systems*, 12(1):3 – 15, 1997. ISSN 0924-7963. doi: https://doi.org/10.1016/S0924-7963(96)00085-1. URL http://www.sciencedirect.com/science/article/pii/S0924796396000851.

J. Simpson and J. Sharples. *Introduction to the Physical and Biological Oceanography of Shelf Seas*. Cambridge University Press, 2012. ISBN 9781107377394. URL https://books.google.co.uk/books?id=kzggAwAAQBAJ.

J. H. Simpson, W. R. Crawford, T. P. Rippeth, A. R. Campbell, and J. V. Cheok. The vertical structure of turbulent dissipation in shelf seas. *Journal of Physical Oceanography*, 26(8): 1579–1590, 1996.

SSB. UK Shelf Sea Biogeochemistry programme, 2016-08-30. URL https://www.uk-ssb.org/.

L. St. Laurent and C. Garrett. The role of internal tides in mixing the deep ocean. *Journal of Physical Oceanography*, 32(10):2882–2899, 2002.

L. St. Laurent and R. W. Schmitt. The contribution of salt fingers to vertical mixing in the north atlantic tracer release experiment. *Journal of Physical Oceanography*, 29(7): 1404–1424, 1999. doi: 10.1175/1520-0485(1999)029<1404:TCOSFT>2.0.CO;2. URL https://doi.org/10.1175/1520-0485(1999)029<1404:TCOSFT>2.0.CO;2.

N. Stashchuk and V. Vlasenko. Bottom trapped internal waves over the malin sea continental slope. *Deep Sea Research Part I: Oceanographic Research Papers*, 119:68 – 80, 2017. ISSN 0967-0637. doi: https://doi.org/10.1016/j.dsr.2016.11.007. URL http://www.sciencedirect.com/science/article/pii/S0967063716302175.

N. Stashchuk, V. Vlasenko, M. E. Inall, and D. Aleynik. Horizontal dispersion in shelf seas: High resolution modelling as an aid to sparse sampling. *Progress in Oceanography*, 128: 74 – 87, 2014. ISSN 0079-6611. doi: https://doi.org/10.1016/j.pocean.2014.08.007. URL http://www.sciencedirect.com/science/article/pii/S007966111400130X.

S. Thorpe. *The Turbulent Ocean*. Cambridge University Press, 2005. ISBN 9781139445795. URL https://books.google.co.uk/books?id=Ax2d94PODgIC.

V. Vlasenko and K. Hutter. Numerical experiments on the breaking of solitary internal wavesover a slope–shelf topography. *Journal of Physical Oceanography*, 32(6):1779–1793, 2002. doi: 10.1175/1520-0485(2002)032<1779:NEOTBO>2.0.CO;2. URL https://doi.org/10.1175/1520-0485(2002)032<1779:NEOTBO>2.0.CO;2.

V. Vlasenko and N. Stashchuk. Internal tides near the celtic sea shelf break: A new look at a well known problem. *Deep Sea Research Part I: Oceanographic Research Papers*, 103: 24 – 36, 2015. ISSN 0967-0637. doi: https://doi.org/10.1016/j.dsr.2015.05.003. URL http://www.sciencedirect.com/science/article/pii/S0967063715000990.

V. Vlasenko, N. Stashchuk, and K. Hutter. *Baroclinic Tides: Theoretical Modeling and Observational Evidence*. Cambridge University Press, 2005. ISBN 9781139446075. URL https://books.google.co.uk/books?id=laMcOuAX7-EC.

V. Vlasenko, N. Stashchuk, M. R. Palmer, and M. E. Inall. Generation of baroclinic tides over an isolated underwater bank. *Journal of Geophysical Research: Oceans*, 118(9): 4395–4408, 2013. doi: 10.1002/jgrc.20304. URL https://agupubs.onlinelibrary.wiley.com/doi/abs/10.1002/jgrc.20304.

V. Vlasenko, N. Stashchuk, M. E. Inall, and J. E. Hopkins. Tidal energy conversion in a global hot spot: On the 3-d dynamics of baroclinic tides at the celtic sea shelf break. *Journal of Geophysical Research: Oceans*, 119(6):3249–3265, 2014. doi: 10.1002/2013JC009708. URL https://agupubs.onlinelibrary.wiley.com/doi/abs/10.1002/2013JC009708.

V. Vlasenko, N. Stashchuk, M. E. Inall, M. Porter, and D. Aleynik. Focusing of baroclinic tidal energy in a canyon. *Journal of Geophysical Research: Oceans*, 121(4):2824–2840, 2016. doi: 10.1002/2015JC011314. URL https://agupubs.onlinelibrary.wiley.com/doi/abs/10.1002/2015JC011314.

J. U. Wihsgott, J. Sharples, J. E. Hopkins, E. M. S. Woodward, T. Hull, N. Greenwood, and D. B. Sivyer. Observations of vertical mixing in autumn and its effect on the autumn phytoplankton bloom. *Progress in Oceanography*, 2019. ISSN 0079-6611. doi: https://doi.org/10.1016/j.pocean.2019.01.001. URL http://www.sciencedirect.com/science/article/pii/S0079661118302544.

N. J. Zabusky and M. D. Kruskal. Interaction of "solitons" in a collisionless plasma and the recurrence of initial states. *Phys. Rev. Lett.*, 15:240–243, Aug 1965. doi: 10.1103/PhysRevLett.15.240. URL https://link.aps.org/doi/10.1103/PhysRevLett.15.240.

M. Zarroug, J. Nycander, and K. Doos. Energetics of tidally generated internal waves for nonuniform stratification. *Tellus A: Dynamic Meteorology and Oceanography*, 62(1):71–79, 2010. doi: 10.1111/j.1600-0870.2009.00415.x. URL https://doi.org/10.1111/j.1600-0870.2009.00415.x.

S. Zhang and M. H. Alford. Instabilities in nonlinear internal waves on the washington continental shelf. *Journal of Geophysical Research: Oceans*, 120(7):5272–5283, 2015. doi: 10.1002/2014JC010638. URL https://agupubs.onlinelibrary.wiley.com/doi/abs/10.1002/2014JC010638.

Z. Zhao. Internal tide radiation from the luzon strait. *Journal of Geophysical Research: Oceans*, 119(8):5434–5448, 2014. doi: 10.1002/2014JC010014. URL https://agupubs.onlinelibrary.wiley.com/doi/abs/10.1002/2014JC010014.

J. Zhou, X. Zhang, and P. H. Rogers. Resonant interaction of sound wave with internal solitons in the coastal zone. *The Journal of the Acoustical Society of America*, 90(4):2042–2054, 1991. doi: 10.1121/1.401632. URL https://doi.org/10.1121/1.401632.